Final Technical Report

Role of Fluid and Temperature in Fracture Mechanics and Coupled THMC Processes for Enhanced Geothermal Systems

Award Recipient Organization: University of Utah (DOE Project DE-EE0007080)

Subrecipient Organization:
Purdue University
DUNS Identifier: 07-205-1394
525 Northwestern Avenue, West Lafayette, IN 47907
Award Number: 5-2557

Project Period:
10/01/2021 – 09/30/2025

Principal Investigator:
Laura Pyrak-Nolte
Professor, Physics & Astronomy, Purdue University
ljpn@purdue.edu
765-494-3005

Report Submitted By:
Laura Pyrak-Nolte
Date of Report Submission: 11/30/2025
Reporting Period: 10/01/2021 – 09/30/2025
Total Pages (excluding cover page): 109

Project Partners: Sandia National Laboratories, University of Illinois at Urbana-Champaign, Northwestern University, and University of Hawaii at Manoa

This material is based upon work supported by the U.S. Department of Energy under Award Number DE-EE0007080.

Abstract

Final Report for Role of Fluid and Temperature in Fracture Mechanics and Coupled THMC Processes for Enhanced Geothermal Systems

DOE Award Number:
Award Recipient Organization: University of Utah (DOE Project DE-EE0007080)
Subrecipient Organization: Purdue University (Award Number: 5-2557)
Principal Investigator: Laura Pyrak-Nolte, Professor

The ability to sustain high energy extraction efficiency from Enhanced Geothermal Systems (EGS) is affected by the ability to measure, characterize, and predict the effect of different perturbations that arise from fluid injection rates, fluid temperature, and shut-in conditions on existing and stimulated fracture systems throughout a subsurface reservoir's lifecycle. The difficulty arises from limited knowledge of the interaction of fluid and temperature driven fractures with frictional interfaces that govern local deformation and frictional behavior in the surrounding rock. Thermo-poro-mechanical coupled processes tend to dominate this interaction and strongly affect the permeability and local stress distributions that impact efficiency and prevent optimal stimulation conditions over multi-decadal time frames.

Our research developed and validated a macroscopic numerical model that can account for local deformation/frictional behavior, seismic/aseismic behavior, chemical reactions. We extended, theoretically, rate-and-state friction relationships for geothermal conditions and performed experiments to provide additional datasets for validation of the model. Laboratory experiments found geophysical signatures of precursors to slip along fractures in response to shearing and determined the parameters that affect interpretation of fracture aperture from electrical methods. A joint inversion method was developed that leverages machine learning methods to combine hydro-thermal datasets to provide a tool for optimal reservoir design for geothermal sites to enable identification of key parameters for heat recovery and quantification of coupled THMC processes that govern fracture evolution.

The outcome of the research is 3 open source tools that are available to the geothermal community: (1) MOOSE-FARM – to simulate dynamic frictional fracture (2D & 3D) elastodynamics with a rate-and-state friction model and a 3D visco-poro-plastic, finite deformation, nonlocal continuum damage-breakage; (2) Theory - that includes temperature, bulk permeability, injection fluid rate, and gouge properties such as friction parameters to improve insight into stable versus unstable sliding; and (3) AI Data Assimilation – for fast model prediction of the reservoir state. These tools provide a breakthrough to quantify both single fracture and reservoir scale states in coupled THMC processes and their evolutions in response to hydro-thermally induced perturbations.

Keywords: [Geothermal, Coupled Processes, Fracture Propagation, Joint Inversion]

Table of Contents

Executive Summary

1.1 Background

The ability to sustain high energy extraction efficiency from Enhanced Geothermal Systems (EGS) is affected by the ability to measure, characterize, and predict the effect of different perturbations that arise from injection rates, fluid temperature, and shut-in conditions on existing and stimulated fracture systems throughout a reservoir's lifecycle. The difficulty arises from limited knowledge of the interaction of fluid and temperature driven fractures with frictional interfaces that govern local deformation and frictional behavior in the surrounding rock. Thermo-poro-mechanical processes tend to dominate this interaction and strongly affect the permeability and local stress distributions that impact.

1.2 Objectives

Our primary objective is to predict the interaction of fluid and temperature driven fractures with frictional interfaces that ultimately impacts the long-term efficiency of the stimulation process in enhanced geothermal systems (EGS). Thermo-hydro-mechanical (THM) processes govern changes in permeability and local stress distribution associated with evolving mechanical and chemical properties along with the local deformation and dynamic frictional behavior in the surrounding rock. To achieve this objective, work was performed to improve (1) the current baseline FORGE THMC (THM-chemical) simulator, FALCON/MOOSE (the Idaho National Laboratories (INL)), through incorporation of the physics of slip, dynamic fracture processes, and wave propagation during geothermal stimulation, and (2) joint inversion methods of multi-modal data sets to predict and monitor the evolution of the problem under THM conditions. Multi-modal bench top experiments and development of mechanistic constitutive relations are critical factors for the validation and successful update of FALCON/MOOSE. The key is to identify key parameters for EGS development and accurately evaluate fracture evolution in response to changes in stress, temperature, fluid pressure, and other thermo-poro-elastic processes, and the impact on optimal long-term heat recovery in EGS. Then geophysical signatures of such evolution can be used to jointly invert multi-modal field data to identify changes in subsurface geothermal reservoirs.

1.3 Key Findings

The outcomes from this project include: (1) a theoretical update of extended rate-and-state friction model as a function of temperature, bulk permeability, injection fluid rate, and gouge properties such as friction parameters for applications in geothermal/hydrothermal systems; (2) development and validation of an open source numerical code (MOOSE-FARMS - Fault and Rupture Mechanics Simulations) for 2D and 3D simulations of dynamic frictional fracture with rate-and-state friction model, and a 3D visco-poro-plastic, finite deformation, nonlocal continuum damage-breakage (CDB) model that has been incorporated into the Idaho National Laboratories (INL) MOOSE platform; (3) experimental data sets on the role of fault gouge properties on coefficients of friction, on the use of compressional and shear waves to detect precursors to slip along fractures, on the interpretation of fracture aperture from electrical resistivity, and well-bore breakout data sets under a range of fluid and temperature conditions for validation of numerical models; and (4) a validated machine-learning (ML) based framework for data assimilation through joint inversion of thermal-hydro-geophysical field data.

The integration of the outcomes listed above has led to the development and validation of 3 open-source tools available to the geothermal community. These tools are

1. **MOOSE-FARM** – to simulate dynamic frictional fracture (2D & 3D) elastodynamics with a rate-and-state friction model and a 3D visco-poro-plastic, finite deformation, nonlocal continuum damage-breakage
2. **Theory** - that includes temperature, bulk permeability, injection fluid rate, and gouge properties such as friction parameters to improve insight into stable versus unstable sliding
3. **AI Data Assimilation** – for fast model prediction of the reservoir state

Introduction

2.1 Purpose of the Report

This report provides a summary of the work performed under the Utah FORGE project 5-2557 by the following participants: Antonio Bobet & Laura Pyrak-Nolte (Purdue Univ., Indiana), Hongkyu Yoon & R. Charles Choen (Sandia National Laboratories, New Mexico), Ahmed Elbana (Univ. of Illinois at Urbana-Champaign, Illinois), John Rudnicki (Northwestern Univ., Illinois), and Jonghyun Harry Lee (Univ. of Hawaii at Manoa, Hawaii).

2.2 Scope of Work

Central to this work was the integration of experimental, theoretical, and computational approaches to enhance heat recovery in geothermal systems through the characterization and monitoring of the impact of fluid and temperature on fracture slip mechanisms and associated changes in permeability and mechanical properties. Laboratory experiments were performed to determine the fundamental relationships among deformation/frictional behavior, permeability, temperature, and injection rates at in-situ EGS conditions. Slip and deformation tests on existing fractures identified seismic phases that are sensitive to evolving fracture properties, fluids, and stresses. Utilizing this extensive dataset, theoretical studies on the physics of slip on existing fractures were evaluated and led to the extension of a rate-and-state friction relationship to include microphysical rate and state parameters related to injection rates, gouge, chemical alterations, imposed slip rate, and bulk permeability. Constitutive equations for modeling dynamic frictional fracture using 2D and 3D elastodynamics with a continuum damage-breakage model (MOOSE-FARMS: FAult and Rupture Mechanics Simulations) were implemented as a stand-alone module to MOOSE. The code includes two of the most widely used friction laws: (1) the slip-weakening friction law and (2) the rate-and-state friction law and can perform simulations with and without pore pressure that account for dynamic poro-elastic effects on damage evolution representing fracture initiation, propagation, and coalescence. The code was validated with laboratory experiments to induce wellbore breakout under a range of temperature and saturation conditions. A joint thermal-hydro-geophysical inversion method was developed and validated and provides uncertainty quantification.

2.3 Organization of the Report

The report is divided into three main sections: Methodology, Results & Discussion, and Conclusions and Recommendations. Under each section, the relevant information for the experimental, theoretical, numerical, and joint inversion work is presented.

Methodology

In this section, the methods and approaches are provided for the experimental (Section 3.1), theoretical (Section 3.2), numerical (Section 3.3) and joint inversion (Section 3.4) studies. In the experimental section, subsection 3.1.1 describes the rock type used for the experimental work, followed by separate subsections for the different experimental methods that were used.

3.1 Experiments

3.1.1 Samples

An alternative granite to the rock found at the Utah FORGE site was selected to enable acquisition of a sufficient quantity of the rock material for multiple tests and to customize its dimensions to fit the different experimental test setups (subsections 3.1.2 – 3.1.4). A literature review was conducted to compare the mechanical properties of different granites with those of rocks at the Utah FORGE site. The primary focus was to identify a similar mineral composition (Table 1) and mechanical properties (
Table 2), especially UCS and grain size, that could significantly affect the strength of rock joints. Information on Utah Forge Rock composition and properties were obtained from Moore et al., (2018). The following granite types were considered a potential test material for the research: (1) Sierra White granite, California; (2) Charcoal granite, Minnesota; (3) Rockville granite, Minnesota; (4) Barre granite. Vermont; (5) Westerly granite. Rhode Island. Five potential alternatives were chosen because they have been widely studied for rock mechanics and engineering. Table 2 shows the physical and mechanical properties of different granites. For the experimental task, Sierra White granite (SWG) has been chosen based on physical and mechanical properties and previous experience on SWG.

Table 1 Mineral composition of the Utah FORGE rock

Composition	Percentage (%)
Plagioclase	37-40
K-feldspar	25-37
Quartz	21-27
Biotite	3-5
Illite or Muscovite	2-4

Table 2 Physical and mechanical properties of different granites.

Properties	FORGE (UT)	Sierra White[1)] (CA)	Charcoal[2)] (MN)	Rockville[3)] (MN)	Barre[4)] (VT)	Westerly[5)] (RI)
Density (g/cm^3)	2.63 - 2.64	2.64 - 2.67	2.72 - 2.75	2.70	2.59 - 2.65	2.63 - 2.64
UCS (MPa)	110 - 130	150 – 165	233	100 - 180	150	200 - 287
Young's modulus (GPa)	23 - 34	35 - 65	60 - 76	25 - 44	20 – 40	51 - 65
Porosity (%)	0.46 (0 - 1)	0.8	0.08	0.03 - 0.5	0.2 - 0.6	< 1
Grain size (mm)	0.1 - 10	0.7 - 3	0.2 - 8	1 - 40	0.25 – 3	0.1 - 1

[1)] Hu et al. (2020), Ingraham et al. (2017), Scott et al. (1985), Ye et al. (2017)

[2)] Kahraman (2002), Labuz et al. (1985, 1987), Pourahmadian & Guzina (2018), Zietlow & Labuz (1998)

[3)] Kahraman (2002), Labuz et al. (1985, 1987), Peng (1976), Tarokh et al. (2017), Zietlow & Labuz (1998)

[4)] Butt et al. (2020), Garg et al. (2020), Li & Einstein (2019), Morgan et al. (2013), Nasseri & Mohanty (2008), Xia et al. (2008), Zafar et al. (2020).

[5)] Griffiths et al. (2017), Heap & Faulkner (2008), Lokajíček et al. (2021), Nasseri et al. (2007, 2009), Petružálek et al. (2020), Rutter & Neumann (1995), Sprunt & Brace (1974)

3.1.2 Geophysical Monitoring of Fractures

3.1.2.1 Ultrasonic Wave Monitoring during Direct Shear Testing

B-value tests were used to ensure that rock samples were fully saturated prior to testing. B-value tests are commonly used in soil mechanics to ensure that a sample is fully water saturated. Full saturation is assumed once the B-value is equal to or very close to 1.0 (e.g., $B > 0.95$). However, this may not be achievable in very stiff soils and rocks because the compressibility of the solid skeleton is comparable to that of the pore water (Biot, 1941, 1956). For rock materials, full saturation is achieved when the B-value remains constant with further increases in back pressure (Wissa, 1969). The application of a back pressure compresses air bubbles inside the rock pores and dissolves them into the pore water (Lowe & Johnson, 1960). The B-value is an undrained response of pore fluid against hydrostatic confining pressure. Thus, when the rock specimen has air bubbles

in the pores, the B-value increases with increasing back pressure as the air bubbles are compressed, which indicates that the degree of saturation is increasing.

B-value Test Sample Preparation: B-value tests were performed on cylindrical Sierra White granite specimens in the custom-built chamber. Table 3 lists the dimensions and physical properties of Sierra White granite (Ingraham et al., 2017; Ye et al., 2017; Hu et al., 2020). Before the tests, the rock specimens were vacuum-saturated with de-aired, deionized water for 24 hours, following the recommendations of ASTM D4767, Standard Test Method for Consolidated Undrained Triaxial Compression Test for Cohesive Soils. The 24 hours were chosen based on the time-dependent weights of the specimens and visual inspection (Han et al., 2021).

Table 3 Dimensions and properties of cylindrical granite specimens

Properties	Sierra White granite
Diameter (mm)	50.8
Height (mm)	76.2
Density (g/cm^3)	2.63
Porosity (%)	< 1
UCS (MPa)	150-165
Young's modulus, E (GPa)	35-65

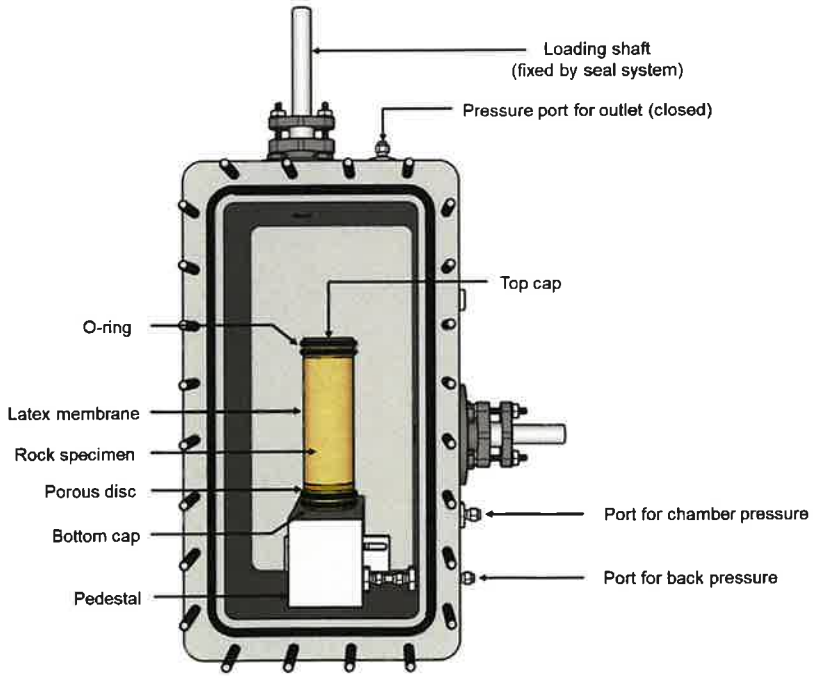

Figure 1. Experimental set-up for B-value tests

Figure 1 shows the experimental set-up for the B-value tests. A vacuum-saturated rock specimen was placed on a pedestal at the bottom of the chamber. A porous disc was mounted at the base of the specimen to uniformly impose the pore water pressure to the specimen, and a stainless-steel cap was placed on the top. A latex membrane with O-ring seals isolated the specimen from the chamber. The O-rings, placed at the top and bottom caps, were further tightened with hose clamps (Hossain, 1995). The chamber pressure (confining stress) and back pressure (pore water pressure) were applied independently using two separate syringe pumps (Teledyne ISCO 500D and 1000D).

Direct Shearing Sample Geometry: Direct shear tests were performed on samples with a single tensile-induced fracture in Sierra White granite from Raymond, California. To create rough fractures, prismatic rock blocks were fractured using a Brazilian technique (Jaeger et al., 2009) or split cylinder method (ASTM D3967), resulting in a single tensile-induced fracture in granite. The dimensions of the rock blocks were 152.4 mm × 127.0 mm × 50.8 mm. The blocks were notched along their sides to facilitate fracture propagation aligned with the loading direction.

Design & Fabrication of Loading Apparatus for Saturated Conditions: Direct shear tests were conducted on dry and saturated rock fractures using a custom-built pressure chamber and a biaxial compression frame. Figure 2 shows the overall test setup for the direct shear tests. A brief description of the apparatus is provided below. A more detailed explanation of each component of the setup can be found in Han (2024).

The complete experimental setup is shown in Figure 3a, including the layout of the ultrasonic sensors for seismic wave measurement. For a test, a fractured rock specimen is placed inside the chamber and is loaded in biaxial compression through the loading shafts. The horizontal loading frame pushes the horizontal shaft and applies a normal stress to the fracture using a computer-controlled system to maintain a constant normal stress. For room temperature conditions, an effective normal stress of 2 MPa was imposed on all specimens. A conventional loading machine was used to displace the vertical shaft to apply shear to the specimen at a constant displacement rate of 8 μm/s. An unjacketed test (e.g., no jackets/membranes) was adopted to impose the chamber pressure (or pore pressure) on the specimen.

The shear testing apparatus was designed to include two loading platens and stainless-steel balls (rollers) to reduce friction on the lateral support. The stainless-steel balls are placed inside a series of 60 holes machined into a stainless-steel plate to hold the balls. The two loading platens, one on each side of the specimen, transfer the horizontal/normal load to the specimen and house piezoelectric sensors for ultrasonic probing of the fracture during shearing. Spherical seats are machined on the top and right platens to ensure that the vertical and horizontal loads align with the specimen to minimize undesired bending moments.

Sensors: Several parameters were monitored during the shear tests, including chamber pressure, normal load, shear load, and shear displacement. The normal and shear loads were measured from strain gauges attached to the tips of the loading shafts placed inside the chamber. The displacements were measured using external LVDTs. Full waveforms of P- (compressional) and S (shear)-waves transmitted across the rock fracture were recorded. Ultrasonic transducers with a central frequency of 1 MHz (Olympus Panametrics V103-RM for P-waves and V153-RM for S-waves) were used for the tests, as they have been successfully used in the past for elastic wave propagation in rock materials (Hedayat et al., 2014a, 2014b, 2018; Modiriasari et al., 2017, 2020;

El Fil 2021). Additional sealing of the transducers was necessary for the saturated tests to prevent water leaks inside the transducers due to the large fluid pressure used, e.g., 4 ~ 8 MPa. Heat shrink tubing was wrapped around the connection between the transducer and the cable, and it was followed by the application of marine epoxy over the heat shrink tubing and the transducer body (not to the wear plate).

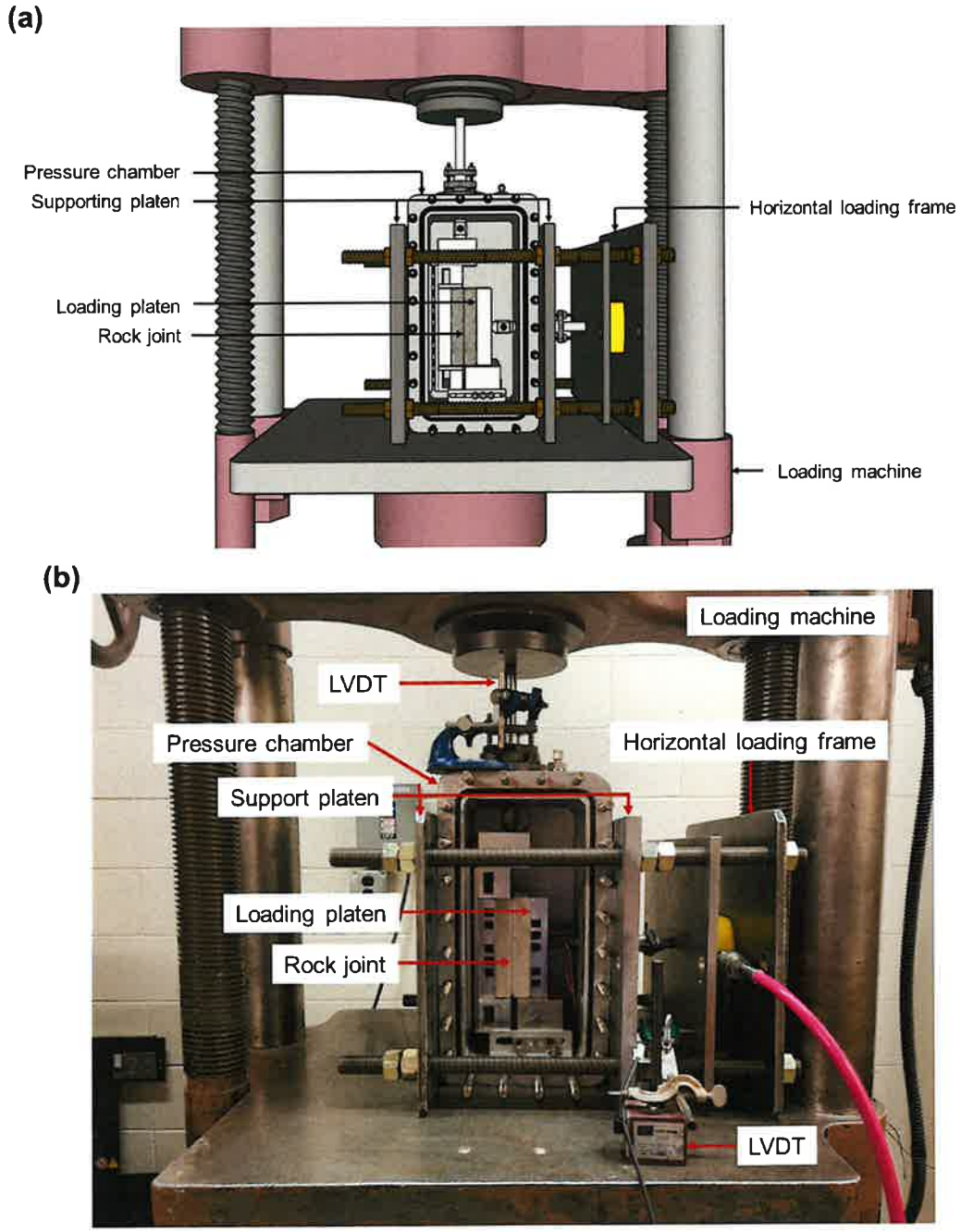

Figure 2 Test set-up for direct shear tests: (a) Schematic drawing; (b) Actual photograph

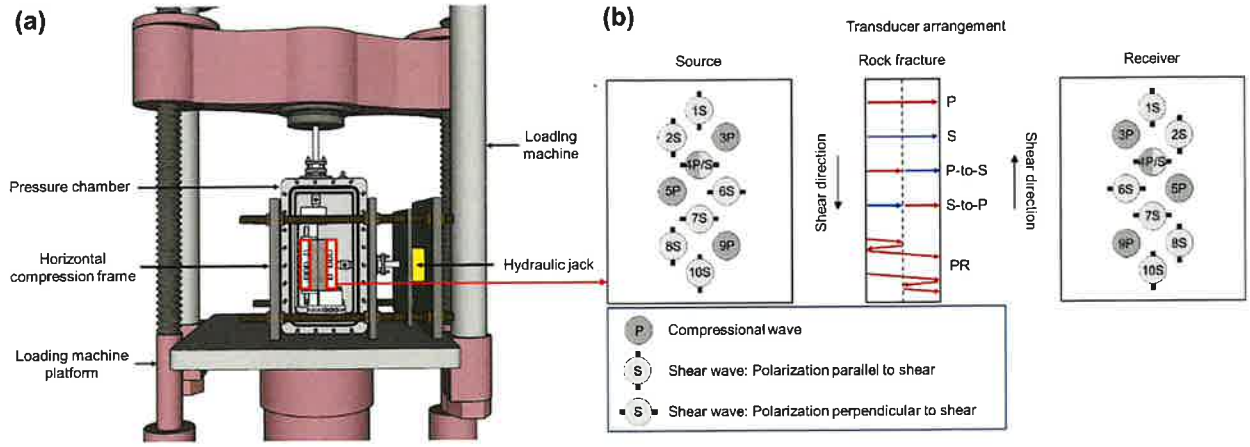

Figure 3 Experimental set-up for direct shear tests with the transducer configuration: (a) Overall setup; (b) Schematic drawing with transducer arrangement inside loading platens. The drawing in the middle of Figure 7(b) shows the wave propagation paths.

During the tests, square wave pulses with a 400 V amplitude were generated with a repetition rate of 1 kHz using a pulser-receiver (Olympus Panametrics model 5077PR). The seismic wave signals were measured at a sampling rate of 100 MHz, and transmitted waves across the specimen were recorded every two seconds. A data acquisition system enabled a synced ultrasonic wave measurement with load and displacement measurements. The system consisted of a chassis (PXI-1042), with two multiplexer terminal blocks (TB-2630), a 68-pin terminal block (TB-2706), a 16-channel DAQ (PXI-6143), and a two-channel 14-bit 100 MHz digitizer (PXI-5122) to monitor multiple full waveforms of signals.

Eight pairs of transducers were used in the tests. Figure 3b provides an example of the transducer configuration, with the numbers indicating the transducer location and the letters P and S denoting the transducer type. The lines on the circles indicate the S-wave polarization. Figure 3b illustrates possible propagation paths of elastic waves that can be shown in the captured waveform, with the wave arrival time ranging from 10 μs to 30 μs, which is the region of interest in this study. P and S refer to the direct P-wave and S-wave transmission across a rock fracture, respectively. P-to-S corresponds to an incident P-wave but is converted to an S-wave at a fracture, while S-to-P is vice versa. PR is the P-wave that either (1) is reflected at a fracture first, then reflected at the source side, and transmitted across a fracture, or (2) is transmitted across a fracture first and reflected at the receiver side, then reflected at a fracture.

Elevated Temperature Components: For elevated temperature conditions, the chamber was modified to accommodate a heater and thermocouples. The chamber pressure was imposed through a syringe pump, and the temperature through an immersion heater placed inside the chamber. The pore pressure was monitored using a pressure transducer before and during the test to check whether it remained constant. The heater was installed at the top of the chamber to avoid contact with the specimen and shear testing components and with the cables from the strain gages

and ultrasonic wave transducers inside the chamber. Two thermocouple probes were installed at the top and bottom of the chamber to measure the temperature across the chamber during the tests.

Direct Shearing Experimental Protocol: A uniform and repeatable protocol was developed to perform the direct shear tests. It consisted of the following steps:

(1) The fractured rock specimen was placed inside the pressure chamber. The chamber and biaxial compression frame were placed on the loading machine platform.
(2) The total normal stress and chamber pressure were gradually increased until the chamber pressure achieved the target magnitude, while keeping the effective normal stress constant. At room temperature, an effective normal stress of 2 MPa and a pore pressure of 8 MPa were applied to the specimens. For elevated temperatures, an effective normal stress of 6 MPa and a pore pressure of 1 MPa were applied.
(3) For elevated temperature conditions, once the chamber pressure reached the target value and stabilized, the temperature of the fluid inside the chamber was increased to the desired value (50°C or 100°C), at the bottom of the chamber, with a heating rate of 6-10°C/hr. Tests under room temperature conditions skipped this step.
(4) The shear load was applied to the rock specimen at a constant displacement rate of 8 μm/s.
(5) Wave signals transmitted across the fracture were recorded along with the normal and shear loads, the normal and shear displacements, chamber pressure, and temperature.

3.1.2.1 Analysis Techniques for Direct Shear Testing Results

B-Value Test Analysis: The procedure for the B-value tests followed a modified ASTM D4767 procedure because of the rock material (Mesri et al., 1976; Chiu et al., 1983; Makhnenko & Labuz 2013; Favero et al., 2018; Han et al., 2021). After flushing all back pressure lines and placing the vacuum-saturated rock specimen in the chamber, the chamber and back pressures were simultaneously increased following a stepwise process, while keeping the effective stress in the specimen constant at 0.2 MPa. B-value measurements were performed by applying an increment of 0.2 MPa to the chamber pressure/confining stress and repeated at higher chamber/backpressures until successive values of the B-value did not change (Wissa, 1969; ASTM D4767). The B-value was calculated as follows:

$$B = \frac{\Delta u}{\Delta \sigma_c}$$

where $\Delta\sigma_c$ is the applied chamber pressure/confining stress (0.2 MPa) and Δu is the change in back pressure/pore water pressure measured at the base of the specimen.

Direct Shearing Data Analysis: Figure 4 and Figure 5 display representative seismic wave signals propagated across dry and saturated fractures in Sierra White granite undergoing shear. Windowing was applied to the signal (i.e., a rectangular window), and then a wavelet transformation was used (Nolte et al., 2000) to extract the peak group amplitude from a given signal. Then, the amplitudes were obtained at the dominant frequency of each mode (i.e., transmitted or converted mode) in the

signals and were subsequently normalized with respect to their initial value prior to shear to facilitate comparisons.

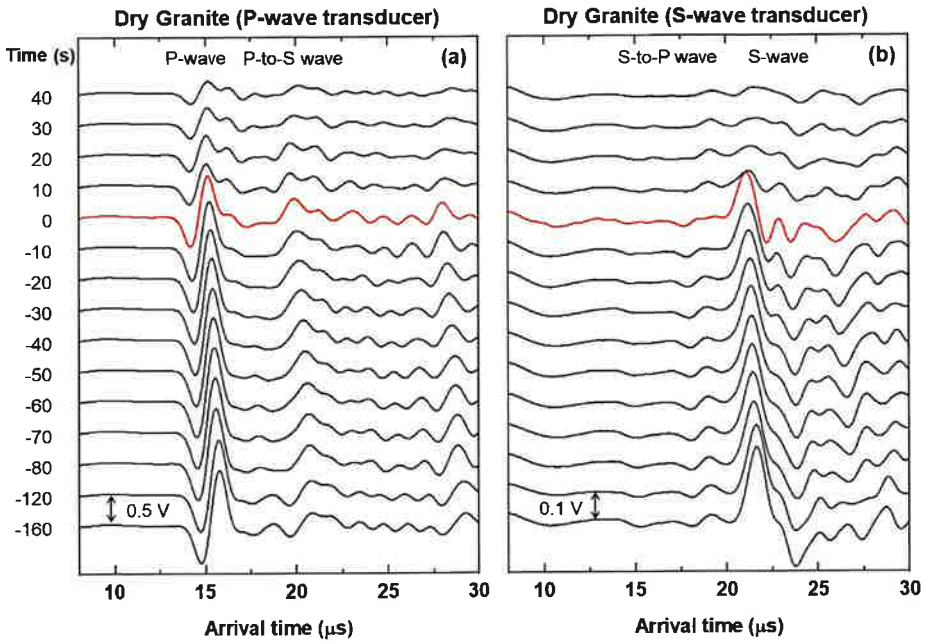

Figure 4 Seismic wave signals during shear: (a) P-wave transducer (3P) in dry granite; (b) S-wave transducer (4S) in dry granite. The vertical axis of the plot is the test time. The red color signal is at the peak shear strength. See Figure 3b for transducer locations.

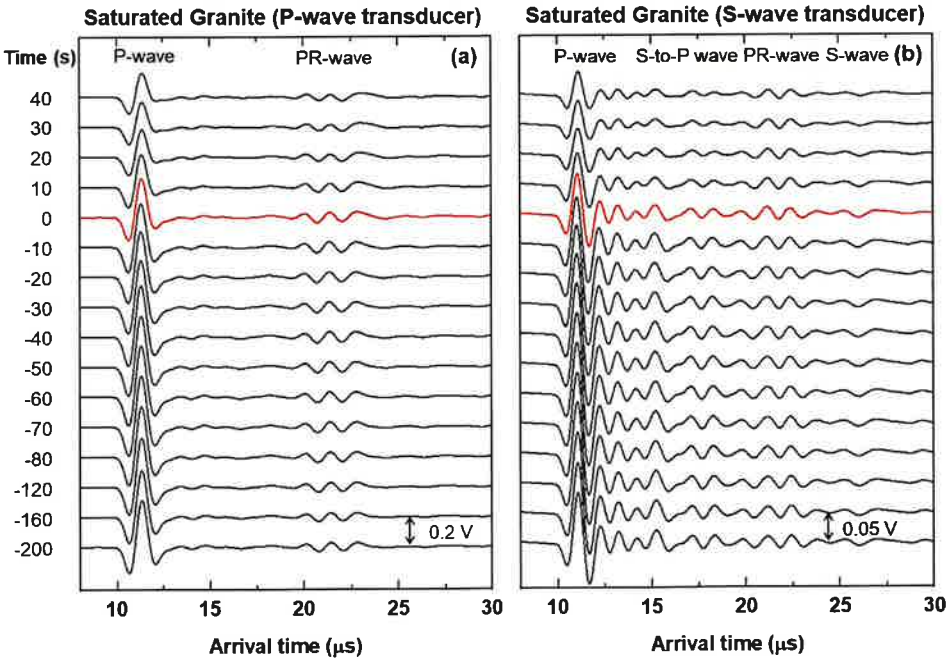

Figure 5 Seismic wave signals during shear: (a) P-wave transducer (3P) in saturated granite; (b) S-wave transducer (4S) in saturated granite. The vertical axis of the plot is the test time. The red color signal is at the peak shear strength. See Figure 3b for transducer locations.

Figure 4 shows the P- and S-wave signals of dry granite fractures with time. Figure 5 is a similar plot, but for saturated granite. The time when the peak shear strength is reached is set to zero to facilitate comparisons among different tests. Negative values refer to times prior to shear failure, while positive values refer to times after the failure. In all the figures, the signal at the peak shear strength is shown in red. For dry granite, the P-wave, P-to-S converted, and S-wave amplitudes decrease with shear before failure. For saturated conditions, important differences are observed. For example, the change in P-wave amplitude, Figure 5a, is not as significant as that for the dry conditions in Figure 4a. In Figure 5, the amplitudes of the signals of the P-wave, converted S-to-P wave, and the S-wave increase with shear, in contrast with what is shown in Figure 4.

In addition, Figure 5 displays two P-wave signals, denoted as P and PR, for saturated granite. As shown in Figure 3, P is the directly transmitted P-wave and is the one considered in this investigation, which consistently appears in all the tests. The PR-wave arrives earlier than the S-wave. The PR-wave signal is not investigated in this study because it may contain information about both transmission and reflection (reflection from the slip surface). While such information is interesting, its analysis is beyond the scope of the research.

Theory for Wave Propagation across a Fracture: The Displacement Discontinuity (DD) theory has been utilized to model the effect of a fracture on seismic wave propagation (Schoenberg, 1980; Cook, 1992; Pyrak-Nolte et al., 1990; Pyrak-Nolte, 1996). When a seismic wave impinges on a fracture, energy partitioning occurs, resulting in an incident wave that is partitioned into reflected, transmitted, and converted waves. Figure 12 illustrates the mechanism of energy partitioning of a seismic wave (P-wave) that is normally incident on a rock fracture. Nakagawa et al. (2000) modeled a rock fracture (Figure 6a) as an interface consisting of a periodic array of inclined microcracks (Figure 6b). Figure 6c illustrates the idealization of the contact through a set of distributed normal and shear springs. κ_{zz} and κ_{xx} are the normal and shear fracture specific stiffnesses of the fracture (the other shear stiffness, κ_{yy}, is not shown). The fracture specific stiffness can be expressed in terms of the stress on the fracture and displacement discontinuity as follows:

$$\sigma_{zi} = \kappa_{ij}[u_j] \quad (i, j = x, z)$$

where σ_{zi} is the stress applied on the fracture (σ_{zz} is the normal stress and σ_{zx} is the tangential stress), $[u_j]$ is the displacement discontinuity across the fracture between two half spaces (notated as subscripts "1" and "2" for the upper and lower spaces), defined by $[u_j] = u_{2j} - u_{1j}$. In the DD theory, the transmission coefficient for a wave propagated across a fracture is associated with the magnitude of the normal and shear fracture stiffness. Figure 6 also displays the cross-coupling stiffness of the fracture (κ_{zx} and κ_{xz}) introduced by Nakagawa et al. (2000). Seismic wave conversion is associated with the cross-coupling stiffness of a fracture. For example, a compressional wave induces both shear and normal displacements across the fracture. The resultant normal displacement is associated with normal fracture stiffness (κ_{zz}) in Figure 6c.

However, the magnitude of shear displacement induced by the normal stress depends on the cross-coupling stiffness (κ_{zx}), which is related to the amplitude of the P-to-S converted wave.

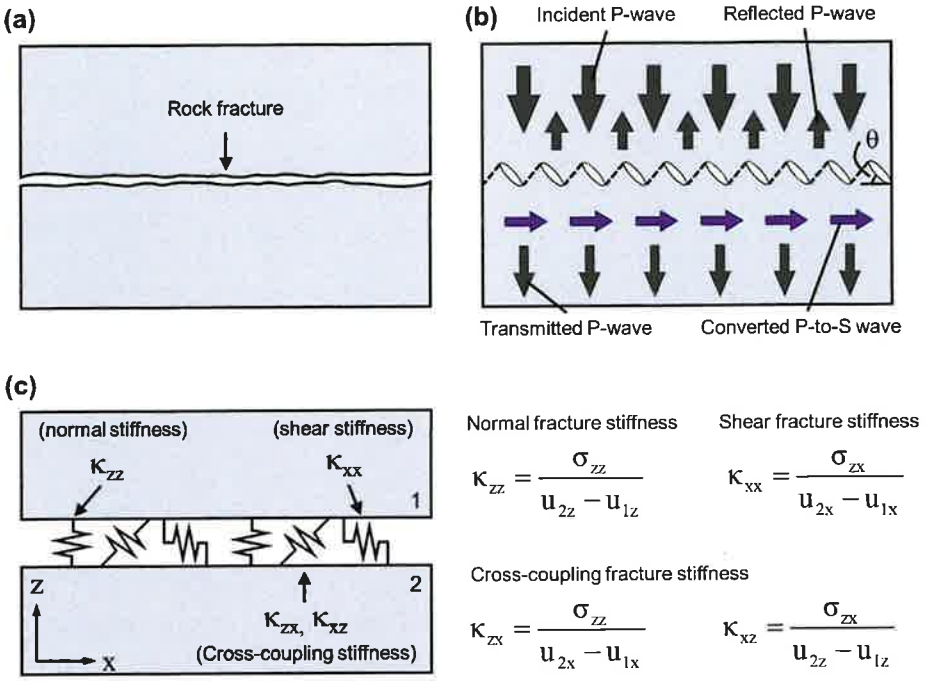

Figure 6. Mechanism of wave energy partitioning and fracture stiffness for a normally incident compressional (P) wave: (a) Rock fracture; (b) Generation of wave conversion (P-to-S wave conversion); (c) Fracture model based on normal, shear, and cross-coupling fra fracture specific stiffnesses. In Figure 7(b), θ is the inclination of the array of microcracks. In Fig. 1(c), σ_{zi} is the stress applied on the fracture and u_{nj} is the displacement induced (i, j = x, z; n describes the upper, n=1, or the lower space, n = 2)

Figure 7 shows transmitted, reflected, and converted coefficients for waves normally incident to a fracture, as a function of the normalized frequency ($\omega Z/\kappa$), which is expressed as the ratio of the product of the wave angular frequency (ω) and the seismic impedance (Z), to the fracture stiffness (κ). The seismic impedance (Z) is the product of the density (ρ) and phase velocity (V) of the fracture half-spaces. Nakagawa et al. (2000) introduced the relative magnitude of the cross-coupling fracture stiffness, R, as:

$$R = \sqrt{\frac{K_{xz} \cdot K_{zx}}{K_{xx} \cdot K_{zz}}}$$

The magnitude of R ranges from 0 (corresponding to 0° inclination of the array of microcracks) to 1 (corresponding to microcrack inclinations of ~ 63°), implying that an increase in R enhances the cross-coupling stiffness.

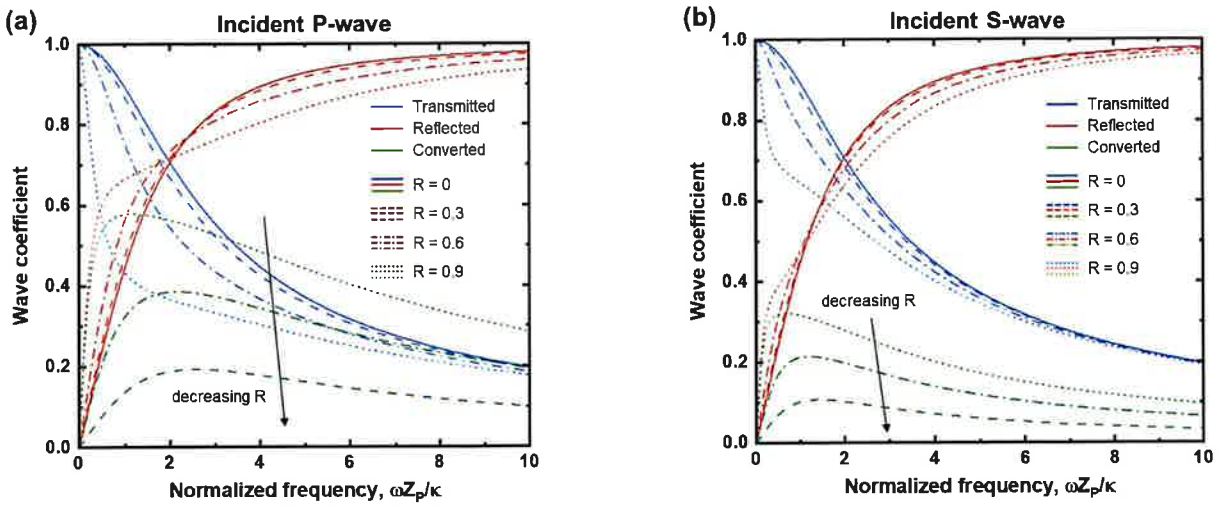

Figure 7. Transmitted, reflected, and converted coefficients for a normally incident seismic wave, as a function of normalized frequency: (a) Incident P-wave; (b) Incident S-wave. It is assumed that V_P = 4,500 m/s, V_S = 2,500 m/s, and ρ = 2.5 g/cm^3 for the calculations. When R = 0, the seismic wave conversion does not occur, and the converted wave coefficient is always zero.

In Figure 7, for all R values, when the fracture stiffness approaches infinity ($\kappa \rightarrow \infty$), the fracture acts as a welded contact, where all the energy is transmitted across the discontinuity and the reflection coefficient goes to zero. In contrast, when the fracture stiffness approaches zero ($\kappa \rightarrow 0$), an increase in normalized frequency is associated with a decrease in the transmission coefficient and an increase in the reflection coefficient, i.e., the fracture behaves like a free surface. The converted wave coefficient shows a non-monotonic behavior and peaks at a normalized frequency ranging between 0.6 and 2.5 for all cases except the R = 0 case.

Natural rock fractures can possess oriented microcracks (or voids) between the two contact surfaces, especially when sheared. In such cases, seismic wave conversion (S-to-P or P-to-S) occurs even for a normal incidence wave, as shown in Figure 7. As discussed, when a rock fracture has oriented apertures/voids, a seismic wave propagated across the fracture contains both the transmitted and converted wave signals. A non-homogeneous rough fracture surface may result in mechanical changes in fracture geometry (void shape, size, and contact area) undergoing shear that will affect the local stiffness of the fracture. In this report, we monitored and investigated the amplitudes of both the transmitted and converted waves recorded along the fracture surface undergoing shear.

3.1.2.2 Electrical Methods for Assessing Fracture Aperture

Laboratory experiments were performed to investigate the factors affecting the interpretation of fracture aperture and flow path tortuosity from electrical resistivity measurements on fluid-filled fractures. 3D X-ray microscopy was used to provide a direct 3D reconstruction of the geometry of the fracture. Comparisons of the interpreted aperture and tortuosity, using the equivalent channel model by Walsh and Brace (1984) with the imaged aperture and tortuosity for idealized fracture geometries, are presented. In addition, numerical models were developed to investigate the

influence of flow path tortuosity and constrictions on the spatial distribution of electric field within the fracture.

Sample Geometry: Complex impedance measurements were conducted on 3D printed nearly cylindrical fractured specimens with dimensions of 25 mm x 27 mm x 80 mm and an aperture of 2 mm. These specimens were prepared with a range of different idealized fracture geometries, including a parallel-smooth fracture, parallel-sawtooth fractures (tortuosity ranging from 1 to 3.8), and a fracture with a centrally constricted channel (designed size: 2 mm x 2 mm x 2 mm) (Figure 8). The fractured specimens were fabricated with an SLA (Stereolithography) 3D printer (FormLabs 3), where a liquid resin (FormLabs Clear resin: RS-F2-GPCL-04) is solidified through the process of photopolymerization. The finished parts were post-cured in an oven utilizing both heat and UV light for 2 hours at 60 °C.

Figure 9 shows detailed drawings of the two fracture geometries: (i) smooth fracture with a constant vertical aperture of 2 mm and width of 25 mm (Figure 9a), and (ii) sawtooth in the Y-Z plane (or Tortuous in Y) with a constant vertical aperture of 2 mm, width of 24.6 mm and ratio of actual to nominal length (or tortuosity) of 1.25 (Figure 9b). As shown in Figure 8, each end face of the specimen is printed together with an end cap that includes a threaded flow port and a fluid reservoir.

Electrical Resistivity Set-up: For electrical resistivity measurements, the electrical impedance method that uses four electrodes was employed. Four Silver/Silver Chloride (Ag/AgCl) electrodes were prepared and attached to the circumference of the specimen, following the procedure presented by Sawayama (2021). The location of the electrodes on the specimen is illustrated in Figure 9a. The first and last electrodes were placed at 15 mm from the edges of the sample. The distance between two consecutive electrodes was set to 10 mm. Four silver mesh strips, cut to a width and length of 5 mm and 82 mm, respectively, were coated on both sides with Ag/AgCl ink and dried in the oven at 100°C for approximately 60 minutes. Each of the electrodes was tightly wrapped around the specimen using Kapton tape and soldered at its edges to a gage terminal. Each gage terminal was then soldered to an electric wire. Since the fractured specimens were designed so that the electrolytic fluid inside the fracture was in direct contact with the Ag/AgCl electrodes, the fracture had to be jacketed to avoid fluid losses during the experiment. The jacketing consisted of one layer of rubberized waterproof tape (Flex tape) tightly wrapped and secured around the specimen-wire assembly.

3D X-ray Imaging: Given that the actual dimensions of the 3D printed specimen might differ from the designed dimensions, 3D X-ray microscopy was used to provide a direct 3D reconstruction of the fracture geometry. The volume of the specimen between the two internal (voltage) electrodes was scanned before conducting electrical measurements using a 3D X-ray Microscope (Zeiss Xradia 510 Versa). A custom-made 3D printed sample holder was designed to facilitate the placement of the specimen in the center of the rotating stage in the microscope. The 3D printed fractured specimen within the sample holder was placed between the X-ray source and detector (source and detector distances of 59 mm and 86 mm, respectively). The scans were conducted with a resolution of ~28 μm/voxel edge length. The energy and power of the scans were 80 kV and 7 W, respectively. The scans were acquired using an exposure time of 1.2 s for each of the 2401 projections, a 0.4× magnification lens, a bin size of 2, and a filter LE2.

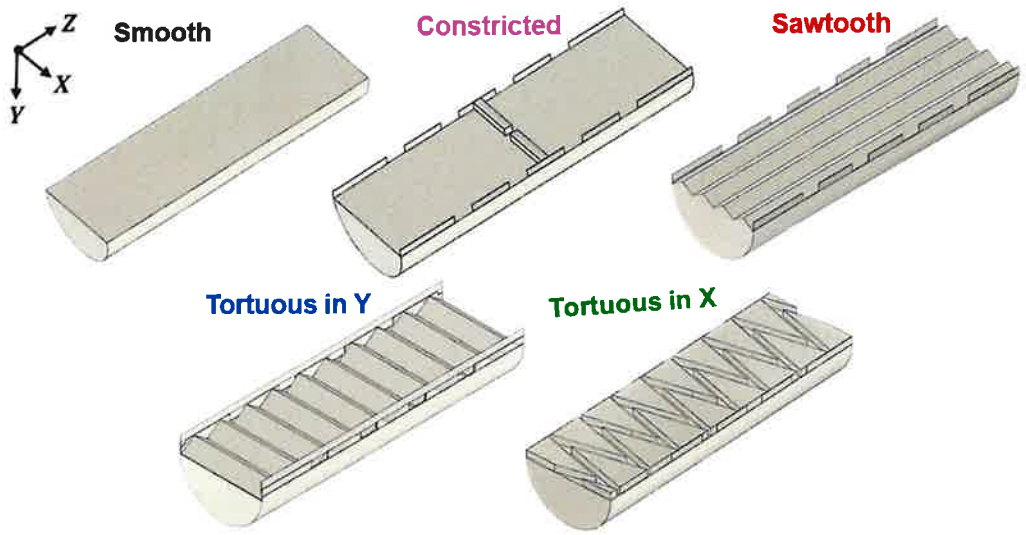

Figure 8. Schematic drawings of idealized fractures: (a) Smooth; (b) Constricted; (c) Sawtooth; (d) Tortuous in Y; (e) Tortuous in X.

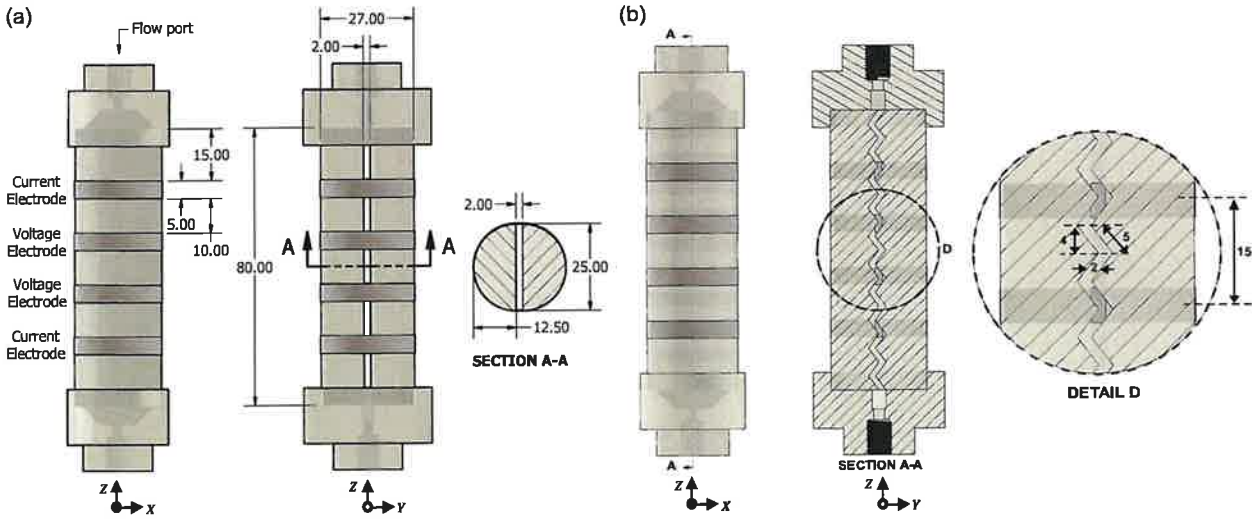

Figure 9. Schematic drawings of 3D printed fractures: (a) Parallel-smooth; (b) Sawtooth in the Y-Z plane (Tortuous in Y). All dimensions are in mm.

Fluid Properties: After sealing the specimen, the fracture was saturated with a sodium chloride (NaCl) solution of specific ionic concentration. Impedance measurements were performed using three solutions with different electrical conductivities: (i) 0.76% by weight NaCl solution ($\sigma_{24°C}$ = 1.33 S/m); (ii) 2% by weight NaCl solution ($\sigma_{24°C}$ = 3.26 S/m), and (iii) 4% by weight NaCl solution ($\sigma_{24°C}$ = 6.07 S/m). An Orion Versa Star Pro Meter and a four-electrode cell conductivity

probe with a built-in temperature sensor acquired fluid conductivity measurements at the measured temperature.

The experimental set-up for fracture saturation and impedance measurements is shown in Figure 10. The jacketed specimen was connected to the inlet and outlet reservoirs with PVC plastic tubing (outer diameter 3.18 mm, inner diameter 1.59 mm). The prepared electrolytic solution was injected through the fracture from bottom to top at a constant flow rate. The flow rate was prescribed using a microfluidic pressure-based flow controller (Fluigent Flow EZ Module, LU-FEZ-1000) and a flow sensor (Fluigent Flow Unit L+, FLU-L-Plus) installed between the fluid reservoir and the specimen. Once fluid started accumulating in the outlet reservoir, saturation of the fracture was achieved, and both the inlet and outlet ports of the specimen were disconnected from the set-up and sealed with plugs.

Electrical Impedance Measurements: Electrical impedance measurements were performed on saturated fractures with a Solartron 1260A impedance analyzer. The electrodes were connected to the impedance analyzer via four coaxial cables (RG-58/U), with each wire soldered to the cable's internal conductor. Impedance measurements were achieved by applying a known sinusoidal voltage signal $V(t) = V_m \sin(\omega_0 t)$ at a given angular frequency ω_0 to the two outer electrodes, which results in a current $I(t) = I_m \sin(\omega_0 t - \theta)$ with a phase shift θ relative to *V(t)*. Simultaneously, the voltage between the two inner electrodes was measured. Impedance (Z) for each angular frequency ω_0 can be simply derived from Ohm's law using:

$$Z(\omega_0) = \frac{V(\omega_0)}{I(\omega_0)} = Z_m cos\theta + iZ_m sin\theta = Z' + iZ''$$

where Z' and Z'' are the real and imaginary components of impedance, respectively, and Z_m and θ are the impedance magnitude and phase angle at a given angular frequency, given by:

$$Z_m = \sqrt{Z'^2 + Z''^2}$$

$$\theta = arctan\left(\frac{Z''}{Z'}\right)$$

The complex resistivity at each ω_0 for a specimen with uniform cross-section A is then calculated as:

$$\rho(\omega_0) = Z(\omega_0)\frac{A}{L}$$

where L is the distance between the two voltage (inner) electrodes. The units of ρ are ohm-meters ($\Omega \cdot m$), while the units of Z are ohms (Ω). In this study, an applied voltage magnitude of 100 mV was adopted and the frequency f ($= \omega/2\pi$) was ranging from 10^{-2} to 10^{6} Hz.

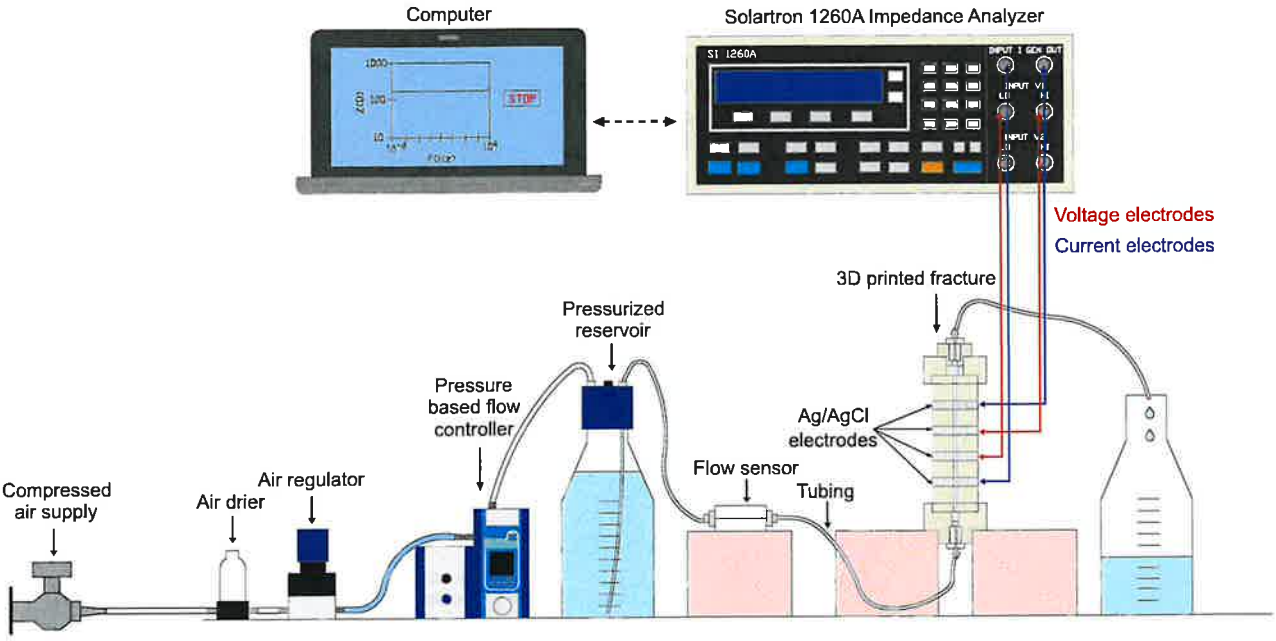

Figure 10. Schematic diagram of the experimental set-up for fracture saturation and electrical impedance measurements with the four-electrode technique.

3.1.2.3 Monitoring Geochemical Alterations to Fractures

This section describes a custom-made transparent flow cell that was designed and fabricated to conduct room- and high-temperature fluid flow tests on individual rock fracture surfaces of Sierra-White granite. The experimental set-up and procedures enabled the continuous monitoring of the electrical conductivity and pH of the effluent under constant flow rate and at room temperature. In addition, the setup was modified to perform fluid flow tests while the specimen was heated to 120 °C, with continuous measurements of effluent conductivity. Fracture surface roughness was measured using laser profilometry and 3D X-ray microscopy before and after the flow tests to evaluate any potential changes in the fracture geometry caused by chemical dissolution phenomena.

Sample Geometry: Laboratory fluid flow experiments were conducted on individual granite fracture surfaces, created through axial splitting of cylindrical specimens of Sierra White granite. Sierra White granite blocks with dimensions of 304.8 mm x 304.8 mm x 101.6 mm were acquired from a quarry in Raymond, California. Cylindrical cores with a diameter of 19 mm were cored from the granite blocks using a coring machine with a diamond-tipped coring bit (25.4 mm outer diameter, 19 mm inner diameter). Each core was cut into cylindrical specimens that were 19 mm in length. Fracture surfaces with dimensions of 19 mm x 19 mm were then created by axially splitting the cylindrical specimens.

Flow Cell: A custom-made transparent flow cell was designed to allow fluid to flow freely over the fracture surfaces, so that the effects of surface roughness and mineral heterogeneity on geochemical alteration could be captured. The components of the flow cell were fabricated with

an SLA (Stereolithography) 3D printer (FormLabs 4), where liquid resin (FormLabs Clear resin: RS-C2-GPCL-05) was solidified through photopolymerization. The finished parts were post-cured in an oven utilizing both heat and UV light for 20 minutes at 60 °C. For the high-temperature experiments, a high-temperature resin (FormLabs High Temperature resin, RS-F2-HTAM-02) was used for the fabrication of its components, allowing them to withstand temperatures of up to 200 °C. The finished parts were post-cured in an oven for 2 hours at 80 °C and 3 hours at 160 °C to ensure maximum heat resistance.

Each fracture surface was placed in an individual flow cell, which consisted of a sample holder and a mated end cap to seal the flow cell (Figure 11). The disk-shaped sample holder with a diameter of 80 mm and thickness of 15 mm included a semi-cylindrical space at the center with a diameter of 20 mm to accommodate the rock specimen. Half of the fractured core was secured to the sample holder with a layer of silicon adhesive (Loctite Superflex Silicone Sealant, Model 595) applied around the core circumference. The sample holder also contained two fluid-distribution reservoirs adjacent to the inlet and outlet flow ports, designed to be sufficiently large to ensure uniformly distributed fluid flow in and out of the fracture surface. Both reservoirs had a length of 20 mm, matching the diameter of the semi-cylindrical space for the rock specimen, and a width and depth of 10 mm, aligning with the radius of the semi-cylindrical space. Once the fracture surface was attached to the holder, the flow cell was sealed by bolting the end cap and sample holder together using a rectangular rubber O-ring seal, as shown in Figure 11b. In addition, the end cap accommodated a rectangular opening with a width of 20 mm, length of 46 mm, and depth of 5 mm (Figure 11c). This ensured a 5 mm aperture between the fracture surface and the lid (Figure 11c).

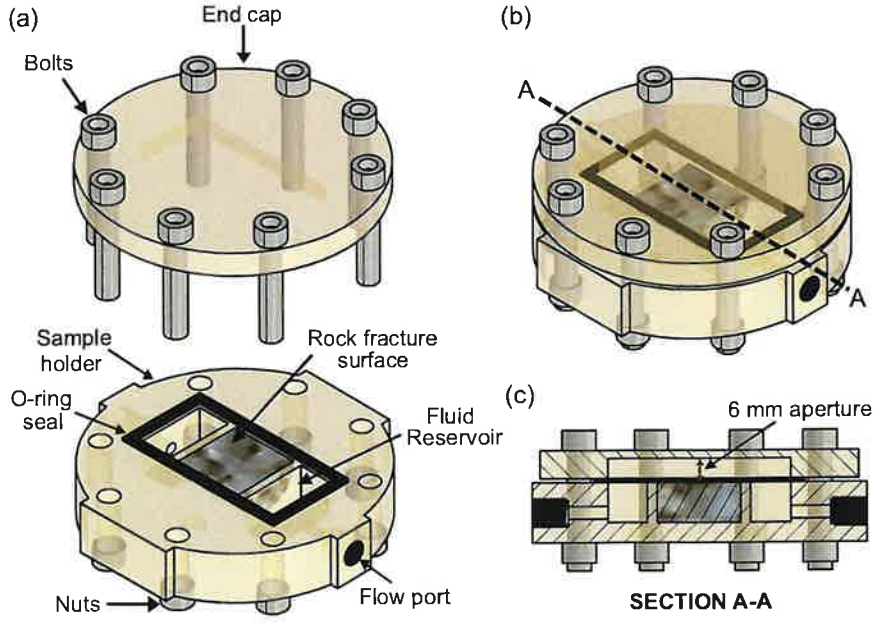

Figure 11. Schematic drawings of the flow cell: (a) Components; (b) Assembly; (c) Vertical cross section A-A

Fracture Surface Roughness Measurements: Laser profilometry and 3D X-ray microscopy before and after the fluid flow tests to measure changes in asperity height along the fracture surfaces. The accuracy of the laser profilometer in capturing the fracture surfaces of granite was limited by its

inability to detect transparent minerals such as quartz. To overcome the limitation of the laser profilometer and improve the accuracy of the surface roughness measurements, 3D X-ray microscopy was chosen as an alternative non-destructive imaging technique. Given the disk-shaped structure of the sample holder and its flat, parallel edges, the surface topography of the fracture was measured while the specimen was placed within the sample holder on the laser profilometer stage and within the X-ray microscope. The fracture surface was first scanned using a Keyence LK-G152 laser (120 μm spot size) with a step size of 100 μm, which was mounted on two computer-controlled translation stages (Newport MTM250PP1) (Figure 12). The vertical resolution of the profilometer was 0.5 μm. The specimen was also scanned using a 3D X-ray Microscope (XRM), (Zeiss Xradia 510 Versa). To be able to mount the specimen in the center of the rotating stage inside the X-ray microscope, a 3D printed sample holder was created, as shown in (Figure 12b. The sample holder was positioned between the X-ray source and detector with source and detector distances of 75 mm and 100 mm, respectively. The voxel size of the scans was ~ 29 μm per edge, while the energy and power were set to 160 kV and 10 W, respectively. The scans were obtained using an exposure time of 2.4 s for each of the 2401 projections, a 0.4× magnification lens, a bin size of 2, and an HE2 filter.

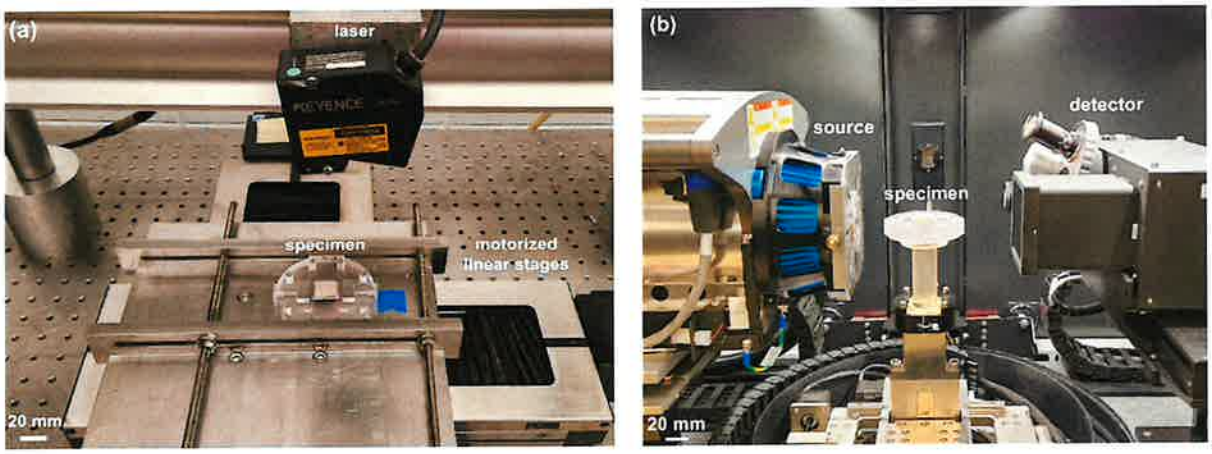

Figure 12. Indiana limestone fracture surface within flow cell: (a) on laser profilometer stage, and (b) in a customized sample holder base within X-ray Microscope.

Fluids: Fluid flow tests were conducted using two types of fluid: (a) an acidic brine solution consisting of sodium chloride (NaCl) and hydrochloric acid (HCl), and (b) a sodium chloride solution. The acidic brine solution was prepared by dissolving 0.75 g of NaCl in 2 kg of deionized water (σ ~ 2 μS/cm), which resulted in an electrical conductivity at 25°C of 750-800 μS/cm. The purpose of using a low-salinity brine was to enhance the sensitivity of the electrical conductivity measurements. At low ionic concentrations, even small changes due to geochemical reactions become more detectable in the effluent. Because the NaCl solution alone would be insufficient to induce geochemical alterations in fracture surfaces within a short period of time (about two days), the acidity of the injected fluid was increased. This was done by adding a 0.15 g of HCl solution with a concentration of 37% by weight (w/w) to the brine. The measured pH and electrical conductivity at 25°C of the acidic brine solution were 3.2 and 1,000-1,100 μS/cm, respectively. A sodium chloride solution, formulated to resemble the composition of water found in geothermal

reservoirs hosted within granitic rock formations, was used for several tests at room temperature and exclusively for the high-temperature tests. Roosevelt Hot Springs is a high-temperature geothermal resource in Beaver Country, Utah. In-situ surface and deep thermal fluids are mainly sodium-chloride (NaCl) brines with a neutral pH and total dissolved solids of 7,000 – 10,000 mg/kg (Ward et al., 1978; Simmons et al., 2018). For the fluid flow experiments, a 0.76 % by weight NaCl solution was prepared by dissolving 7.6 g of NaCl in 1 kg of distilled water ($\sigma \sim 2$ μS/cm). The electrical conductivity of the prepared NaCl solution at 25 °C varied between 13.5 and 13.8 mS/cm.

Fluid Flow Measurement Components: A schematic of the experimental setup for fluid flow tests on rock fracture surfaces at room temperature is shown in Fig. 8. The sealed flow cell enclosing the specimen was connected to the inlet and outlet reservoirs using plastic (Tygon PVC) tubing with outer and inner diameters of 3.18 mm and 1.59 mm, respectively. Acidic brine stored in a 1 L glass bottle (pressurized reservoir in Figure 13) was injected through the fracture surface at a constant flow rate of 0.5 ml/min using a microfluidic pressure-based flow controller (Fluigent Flow EZ Module, LU-FEZ-1000). A flow regulator was used to manage the fluid pressure in the reservoir, while allowing controlled flow of the fluid through the tubing and into the experimental setup. In addition, a flow sensor (Fluigent Flow Unit L+, FLU-L-Plus) was installed between the pressurized reservoir and the flow cell. In series with the flow cell, a constant head reservoir was connected to continuously monitor the effluent electrical conductivity, pH, and temperature. This monitoring reservoir, fabricated with the same 3D printing material as the flow cell, had a rectangular prismatic shape with external dimensions of 31 mm x 51 mm x 68 mm. The dimensions of the reservoir were selected to accommodate the placement of both a conductivity and a pH probe, which required to be submerged to a specific depth for accurate readings. During a typical fluid flow test, the monitoring reservoir was filled with the solution before initiating the flow. After the onset of flow, fluid entered the reservoir through an inlet port at the bottom and exited through an outlet port located 40 mm above the inlet port. Cumulative effluent weight was measured continuously using a digital laboratory scale. The flow test was terminated after 48 hours.

Measurements of Effluent Properties: The conductivity and pH of the effluent was monitored every minute throughout the duration of the test. An Orion Versa Star Pro Meter, equipped with a four-electrode conductivity probe and a pH probe, both incorporating built-in temperature sensors, acquired fluid conductivity and pH measurements that were then recorded in a computer. The bodies of both the conductivity and pH probes were made of epoxy to prevent corrosion over time. Although the fluid flow tests were performed at a relatively constant room temperature (between 21.5 °C to 22 °C), a linear temperature compensation was applied to the recorded conductivity values for meaningful comparisons between different tests (all expressed at a reference temperature of 25 °C). The following linear relationship is usually a good approximation for the temperature compensation (Walton 1989):

$$\sigma_T = \sigma_{25}[1 + a(T - 25)]$$

where σ_T is the electrical conductivity at T (°C), σ_{25} is the electrical conductivity at 25 °C, and a (°C^{-1}) is a temperature compensation factor. In this study, an automatic 2.1 % per 1 °C correction (a = 0.021 °C^{-1}) was applied to the measured conductivity, which is considered a good approximation for sodium chloride solutions (Walton, 1989; Thermo Fisher Scientific, 2018).

Elevated Temperature Experiments: A similar experimental setup was used for fluid flow tests at 120°C (Figure 14). After scanning, the flow cell with the fractured specimen was inserted into a

laboratory forced-air oven and was connected to the inlet and outlet reservoirs with PEEK (polyether ether ketone) tubing (outer diameter 3.18 mm, inner diameter 1.59 mm). PEEK fittings were also used for the high-temperature fluid flow tests due to their heat and chemical resistance properties. Brine (0.76 % by weight NaCl solution) at room temperature was injected through the fracture surface at a constant flow rate of 2.5 ml/min. The total flow time during these tests reached 21 hours.

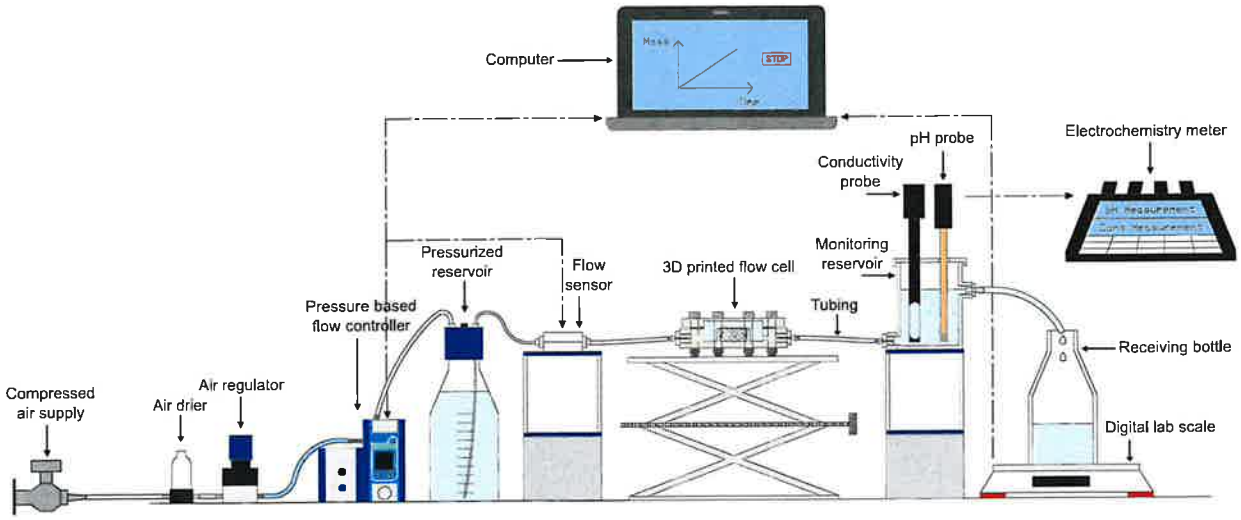

Figure 13. Schematic drawing of the experimental set-up for laboratory fluid flow tests.

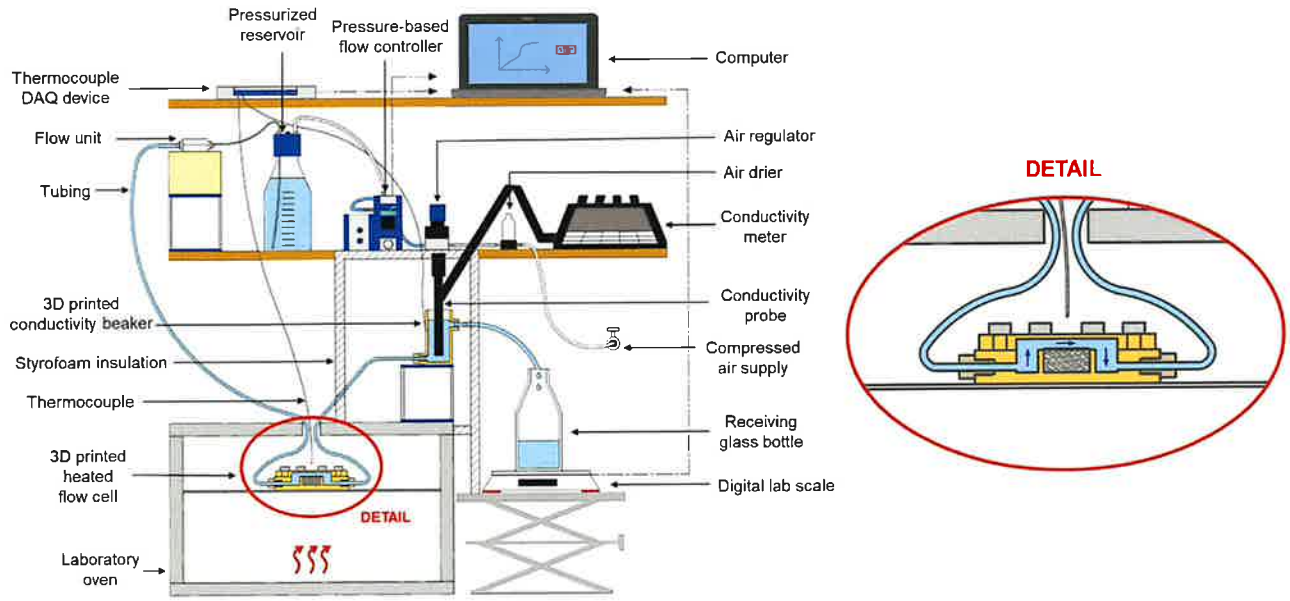

Figure 14. Schematic diagram of the experimental set-up for the high temperature fluid flow tests.

3.1.2.5 Monitoring of Hydraulic & Mechanical Behavior of Fractures in Rock

This section describes an X-ray transparent hassler type core holder that was designed and fabricated to conduct laboratory flow-through experiments with simultaneous measurements of electrical impedance, stiffness and permeability on saturated rock fractures subjected to hydrostatic loading.

Design & Fabrication of X-ray Transparent Pressure Cell: The core holder was designed to meet the following key requirements: (1) the main body had to be X-ray transparent, (2) a cylindrical geometry was preferred for uniform material distribution, (3) structural strength was required to withstand internal pressures up to 15 MPa, and (4) the overall dimensions had to be compatible with the X-ray microscope setup to ensure adequate image resolution.

A modified version of the flow-through reaction cell by Kahl et al. (2016) was developed for this study. The main body was fabricated from polyether ether ketone (PEEK) due to its excellent mechanical strength and chemical resistance. The assembly consists of a hollow PEEK cylinder, top and bottom end caps, and steel reinforcement rings for structural integrity (Figure 15). Cylindrical rock specimens (25.5 mm diameter, 80 mm length) were mounted between the end caps and enclosed within the holder, which provides space for specimen jacketing and geophysical instrumentation. The core holder was dimensioned to maintain mechanical stability under 15 MPa confining pressure, with optimum wall thickness determined through finite element analysis using ABAQUS. The top and bottom end caps incorporate ports for fluid flow, pressure application, and geophysical wiring feedthroughs (Figure 15). A modified top end cap was made to include additional feedthrough to accommodate extra instrumentation.

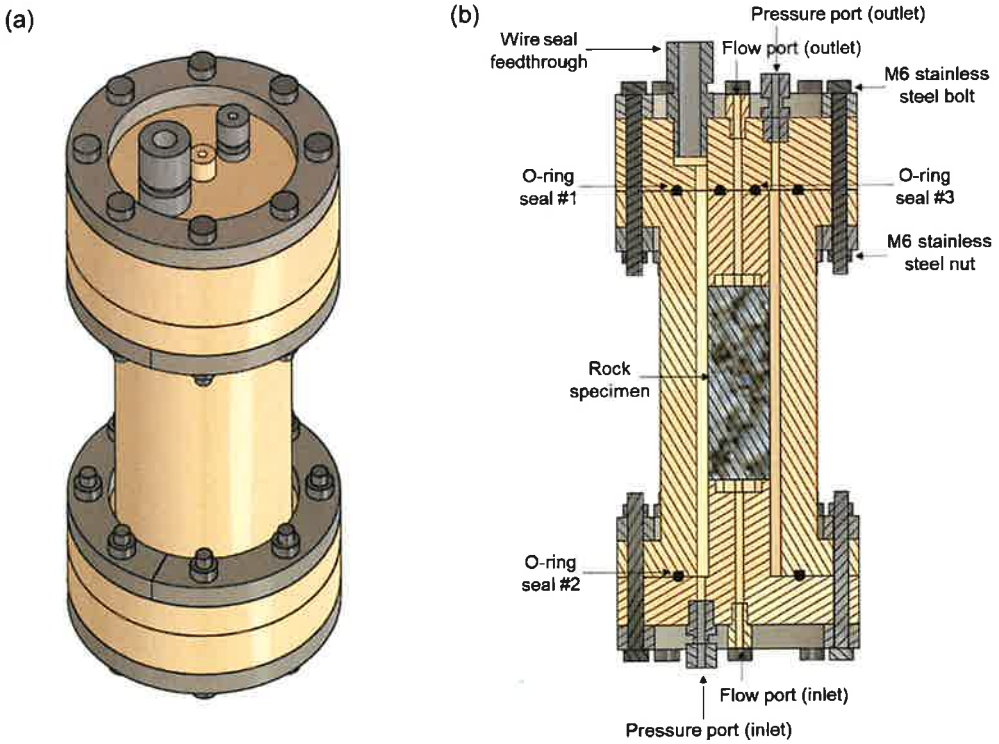

Figure 15. Core holder assembly: (a) Three-dimensional view; (b) Cross-sectional view.

Specimen Geometry and Preparation: Laboratory flow-through experiments were performed on tension-fractured Sierra White granite specimens. Cylindrical cores with a diameter of 25.4 mm were extracted from a prismatic granite block (203.2 × 101.6 × 38.1 mm) using a coring machine equipped with a diamond-tipped bit (31.75 mm outer diameter, 25.4 mm inner diameter). Each core was subsequently cut into 80 mm-long cylindrical specimens. A small notch along the sides of the specimen, with a depth of approximately 3 mm, was made with a saw to facilitate splitting of the core. The specimens were then axially split to create fracture surfaces measuring 19 × 80 mm. The two halves were reassembled using silicone adhesive applied along the notched surface.

Electrical Resistivity Electrodes: To enable electrical and seismic measurements, the specimen was equipped with four silver–silver chloride electrodes (prepared as described previously) and three custom-made piezoelectric transducers. After the adhesive was cured, three grooves were carefully created along the specimen length using a hand-held rotary tool (Figure 16a). Each groove, positioned between two consecutive electrodes, measured 8 mm in length and 3 mm in depth to accommodate piezoelectric crystals (6 mm diameter, 2 mm thickness). For transducer installation, a layer of conductive tape was first placed in each groove, followed by conductive epoxy and the crystal (Figure 16b). The conductive tapes of all transducers were interconnected by grounding wires. The top surface of each crystal served as the signal side, to which individual signal wires were soldered, while a single ground wire was attached to the conductive tape of the middle transducer. Similarly, four signal wires were soldered to the electrodes attached to the specimen.

Ultrasonic Sensor: The grooves containing the custom-made transducers were filled with marine epoxy until the crystals were fully encapsulated. Marine epoxy was also applied to seal the electrode terminals. The fractured specimen was then positioned between the two end caps of the core holder (Figure 16c). Rubber washer discs (25.4 mm outer diameter, 19 mm inner diameter, 3.175 mm thickness) were placed between each specimen face and the end cap to act as deformable spacers, preventing surface damage and improving sealing. The top specimen end cap was 3D-printed with circumferential grooves to allow effective sealing of transducer and electrode wires. A rubberized coating was applied inside the grooves to encapsulate and seal the wires. Finally, the specimen along with the end caps was jacketed to avoid contact between the rock and the confining fluid during the pressure test. The jacketing consists of one layer of rubberized waterproof tape tightly wrapped around the specimen-end caps assembly and two pieces of rubber tubing compressing the edges of the specimen, as shown in Figure 16d. The entire core holder assembly including port fittings is shown in Figure 15.

Experimental Set-up & Protocols: A schematic diagram of the experimental set-up for the flow-through tests is illustrated in Figure 17. The core holder includes two water pressure ports, one at the bottom end cap and one at the top end cap, which are used to apply confining pressure to the specimen. Confining pressure is applied through the bottom port using a syringe pump (Teledyne Isco Model 1000D) connected to a controller that maintains a constant pressure. The syringe pump is also equipped with a high-precision pressure transducer (accuracy 0.1% of full-scale output). The controller is connected to a computer where continuous measurements (every second) of water pressure, total volume inside the pump, and flow rate are conducted. The syringe pump is connected to the core holder through stainless steel tubing. A pressure transducer (GeoTAC PS2K) is installed between the inlet pressure port and the pump to monitor the confining pressure inside

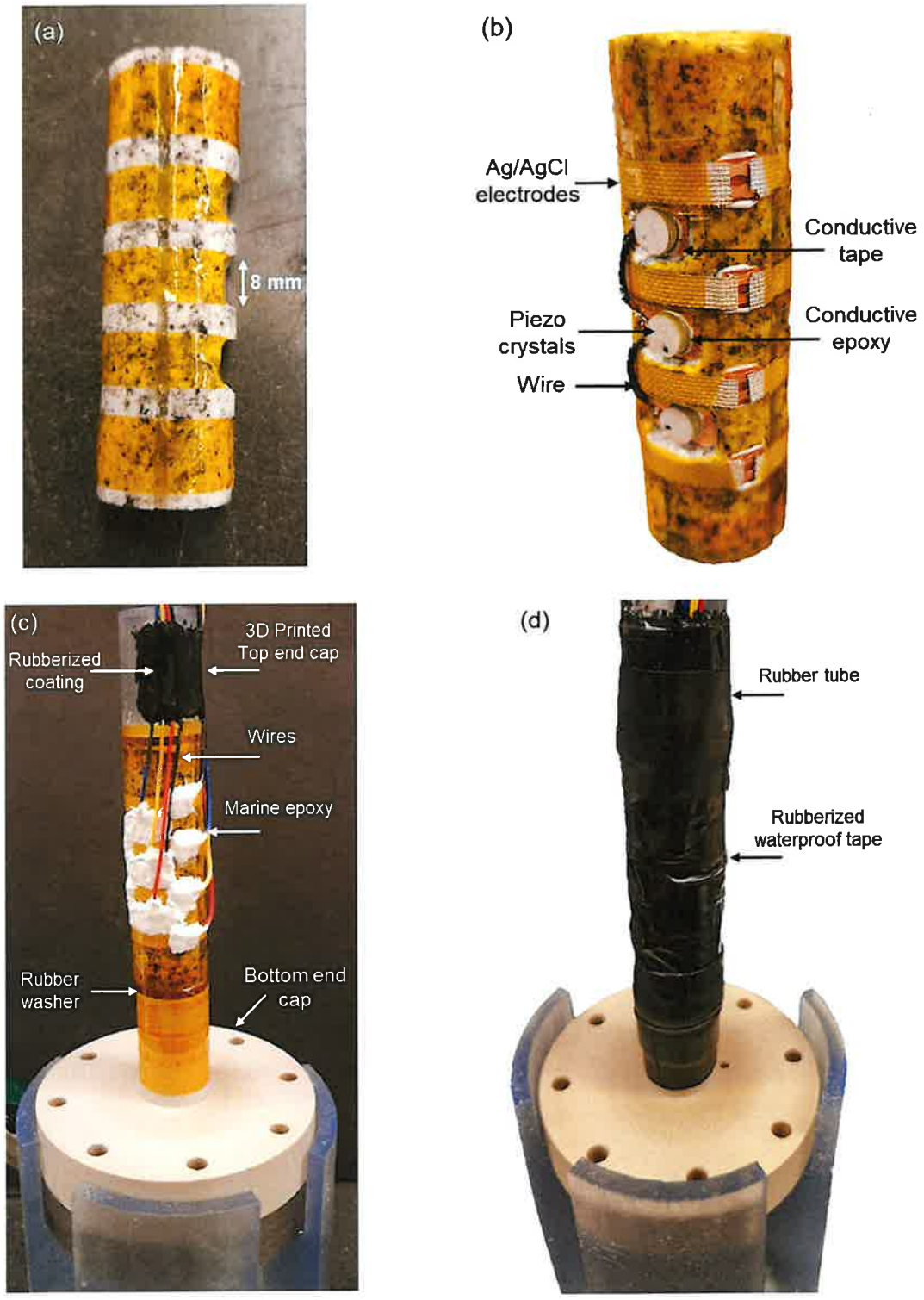

Figure 16. Preparation and assembly of the instrumented fractured specimen: (a) specimen with electrodes and piezoelectric transducers; (b) specimen-end cap assembly before jacketing; (c) specimen-end cap assembly after jacketing.

the core holder. Confining pressure is also recorded every second using a data acquisition (DAQ) system, consisting of an advanced digital I/O (ADIO) module, a network module, and a DAQ software (GeoTAC TestNet). To apply confining pressure, water was injected into the core holder through the bottom pressure port, while the outlet valve remained open to allow air to escape. Once the core holder was completely filled with the confining fluid, injection was paused, and the outlet valve was closed. The confining pressure was then increased to the target value. The initial pressure for all tests was 50 kPa, and the maximum applied pressure was 5 MPa.

At a confining pressure of 50 kPa, the fracture was first filled with an electrolytic solution (2% NaCl by weight, $\sigma_{24°C}$ = 3.3 S/m), which was slowly injected from bottom to top through PEEK tubing at a constant flow rate of 20 μL/min. The flow rate was prescribed using a microfluidic pressure-based flow controller (Fluigent Flow EZ Module, LU-FEZ-1000) and a flow sensor (Fluigent Flow Unit L+, FLU-L-Plus) installed between the fluid reservoir and the specimen. After complete saturation and at each confining pressure level, measurements of permeability, electrical impedance, and reflected waveforms were performed. To measure fracture permeability, different pressures were applied to the pressurized reservoir using a flow controller, while the flow rate was continuously monitored. Cumulative effluent weight was also measured continuously using a digital laboratory scale. A differential pressure transducer (Omega PX2300-1BDI) was installed between the inlet and outlet flow ports of the core holder to measure the pressure drop across the specimen. The transducer was excited by dual-output DC power supply (HP 6234A), and its output was continuously recorded using a National Instruments digital multimeter (USB-4065).

At each stress level, reflected wave signals were also recorded using a seismic measurement system that includes a pulse-receiver (Olympus Panametrics model 5077PR) sending a 400V square wave excitation to the source transducer, with a repetition rate of 1 kHz. The pulser-receiver

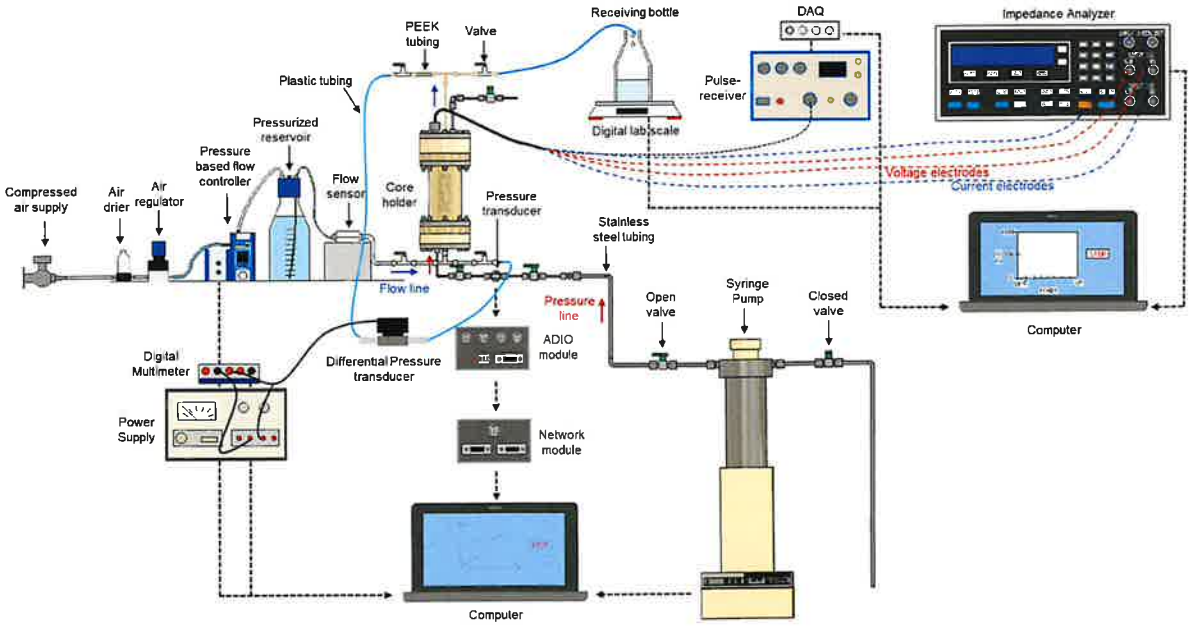

Figure 17. Schematic diagram of the experimental set-up for flow-through tests on granite fractures.

amplifies and filters the received signals reflected across the specimen, which are then recorded using a National Instrument data acquisition system. Electrical impedance measurements were performed with a Solartron 1260A impedance analyzer. The electrodes were connected to the impedance analyzer via four coaxial cables (RG-58/U), with each wire soldered to the cable's internal conductor. A single sine voltage drive was applied to the two outer electrodes and the voltage between the two inner electrodes was measured simultaneously. An applied voltage magnitude of 100 mV was adopted and the frequency f $(= \omega/2\pi)$ was ranging from 10^{-2} to 10^{6} Hz.

3.1.2.5 Analysis Techniques for Electrical Methods

Numerical Modeling of Electric Field: To quantify the influence of fracture geometry on electrical conduction, a two-dimensional (2D) finite element model was developed in MATLAB. The model represents a vertical cross-section of the fracture plane, where the out-of-plane direction corresponds to the fracture aperture, b, for the smooth and constricted fracture and the fracture width, w, for the tortuous in X- and Y- axis fractures. The fracture is assumed to have a uniform aperture and to be filled with a conductive fluid of resistivity ρ (conductivity $\sigma = 1/\rho$). For each geometry, the region between the two internal voltage electrodes was modeled. In this 2D computational domain representing the fracture cross-section, the governing equation for steady-state electrical conduction is the Laplace equation for the electric potential $V(x, y)$:

$$\vec{\nabla} \cdot (\sigma \vec{\nabla} V) = 0$$

This equation corresponds to the conservation of electric charge under steady-state conditions, assuming isotropic and homogeneous conductivity. The applied boundary conditions simulate an imposed potential difference across the fracture while constraining current flow within its walls: (a) inlet (left boundary): Dirichlet potential $V = V_{in} = 0.1$ V; (b) outlet (right boundary): Dirichlet potential $V = 0$ V, and (c) top and bottom walls: electrically insulating $(\vec{n} \cdot \sigma \vec{\nabla} V = 0)$. The fracture geometry was discretized using linear triangular elements, as shown in Figure 18 for a tortuous fracture.

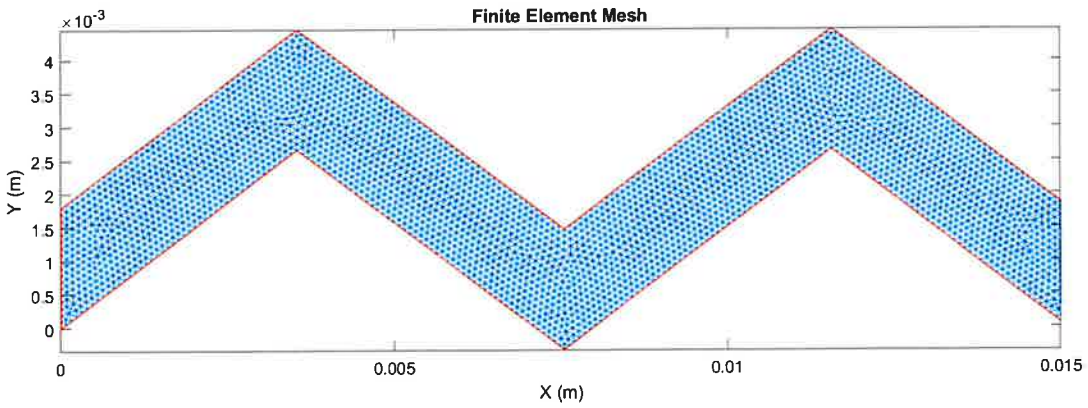

Figure 18. Finite element mesh for an idealized tortuous fracture (tortuous in Y).

Hydraulic & Electrical Aperture Analysis: Permeability measurements were also performed at each stress level. The measured flow rate were graphed against the differential pressure across the specimen for each confining pressure. Linear regression of the data points at each stress level was used to estimate the slope. This slope was then used to estimate the fracture aperture based on the cubic law for laminar flow between parallel plates. Assuming the fracture has a uniform aperture b, the volumetric flow rate Q (m^3/s) is related to the pressure drop ΔP (Pa) by:

$$Q = \frac{wb^3}{12\mu L}\Delta P$$

where w is the fracture width perpendicular to flow, L is the flow path length, and μ is the fluid viscosity. From the slope of the measured Q–ΔP curves at each confining pressure, the mean hydraulic aperture b_h was calculated as:

$$b_h = \left(\frac{12\mu L(slope \cdot 10^{-6})}{w}\right)^{1/3}$$

A mean electric aperture was also estimated using the parallel plate model to enable comparison with the hydraulic aperture. This model is a simplified version of the equivalent channel model by Walsh and Brace (1984), in which the fracture tortuosity is assumed to be unity. Electric aperture was then approximated by:

$$b_e = \frac{\rho_f}{Z}\frac{L}{w}$$

3.1.3 Datasets for Parameters & Validation of Theory & Models

3.1.3.1 Role of Gouge on Shear Behavior

Laboratory shear tests were conducted on pulverized Sierra White granite (SWG) to investigate slip mechanisms in naturally occurring faults. Synthetic fault geometries were constructed by sandwiching fine grained SWG powder in between steel forcing blocks as shown in Figure 19.

Sample & Gouge Preparation: For dry experiments, ~3.5 g of SWG powders was poured onto the face of the lower steel forcing block and leveled. For saturated experiments, enough fluid was added to the ~3.5 g of SWG powders to form a slurry. This slurry was applied to the lower forcing block and leveled. Inclined forcing blocks with 25.4 mm diameter and 35° faces, which were machined from ground steel rods with fine teeth on the faces, help to hold the gouge in place and prevent delamination at the interface. The top forcing block had a 2.03 mm centered hole to allow pore fluid access to the gouge. A fine steel mesh prevented back flow of the gouge into pore fluid lines. Samples were isolated from the confining medium using three layers of heat shrink polyolefin. The outer layer was shrunk over the O-rings on the end caps to form an impermeable seal, which was reinforced with steel tie wires on both sides of the O-rings. Hardened steel spacers and copper shim stock was placed between the steel forcing blocks and the end caps to preserve the parallelism of the Hastelloy wetted parts. For dry samples, the end caps were plugged, while the end caps for the saturated samples were connected to pore lines.

Loading Conditions: An isopar-pressurized chamber with an axial loading ram in a conventional loading machine is shown in Figure 19. The jacketed rock specimen is placed inside the chamber, where it is loaded triaxially. The hydraulic intensifier applied a confining pressure via pressurized fluid to generate a normal stress on sample. The shear load was imposed on the specimen by advancing the axial ram at a constant displacement rate. During the experiments, 15 MPa confining pressure, P_C, was applied to the sample before 5 MPa pore pressure, P_P, to generate 10 MPa effective pressure, P_E, where $P_E = P_C - P_P$. The confining pressure was increased to 80 MPa at a rate of 2.5 MPa/min while pore pressure was held constant to apply an effective pressure of 75 MPa. A differential stress of 1 kN was applied to the sample, and the axial ram was displaced at sequential constant rates of 36, 3.6, 0.36, 36, 360, and 36 mm/hr. The loads were obtained from an internal load cell, confining pressure from a pressure transducer mounted on the intensifier, and pore pressure from a syringe pump.

Experimental Protocol: The procedure for the direct shear tests involved the following steps:

(a) A Sierra White granite gouge sample was prepared.
(b) The jacketed fault specimen was placed inside the vessel, and the vessel was sealed.
(c) A target effective pressure (e.g., 75 MPa) was applied first to the sample and was held throughout the experiment.
(d) The axial load was applied to the rock specimen by imposing a constant displacement rate of 0.36 to 360 mm/hr.

3.1.3.1.1 Analysis Techniques for Gouge Experiments

Three shear experiments were performed on two dry gouge samples and one water saturated sample with effective pressures (P_E) from 15 to 75 MPa. Due to the experimental geometry, application of effective pressure, P_E, increased the normal stress, σ_n, while the application of an axial stress, σ_A, increased both the normal stress and the shear stress, τ, as follows:

$$\tau = (\sigma_A - P_C) \sin\theta \cos\theta$$

and

$$\sigma_n = P_C + (\sigma_A - P_C) \sin^2\theta$$

where θ is the angle of the face of the forcing blocks (= 35°). The friction coefficient is the ratio between shear stress and normal stress as below,

$$\mu = \tau/\sigma_n.$$

As the sample deforms, the inclination of the frictional interface causes the forcing blocks to move laterally as well as vertically, changing the true area of contact for the fault gouge. The reduction in contact area can be corrected by

$$A/A_0 = \Theta - \sin\Theta/\pi$$

and

$$\Theta = \pi - 2\sin^{-1}[(dl/2r)\tan\theta]$$

where r is the radius of the cylinder, dl is the axial displacement, and θ is the angle of the inclined face. True normal and shear stress are the uncorrected values divided by A/A_0.

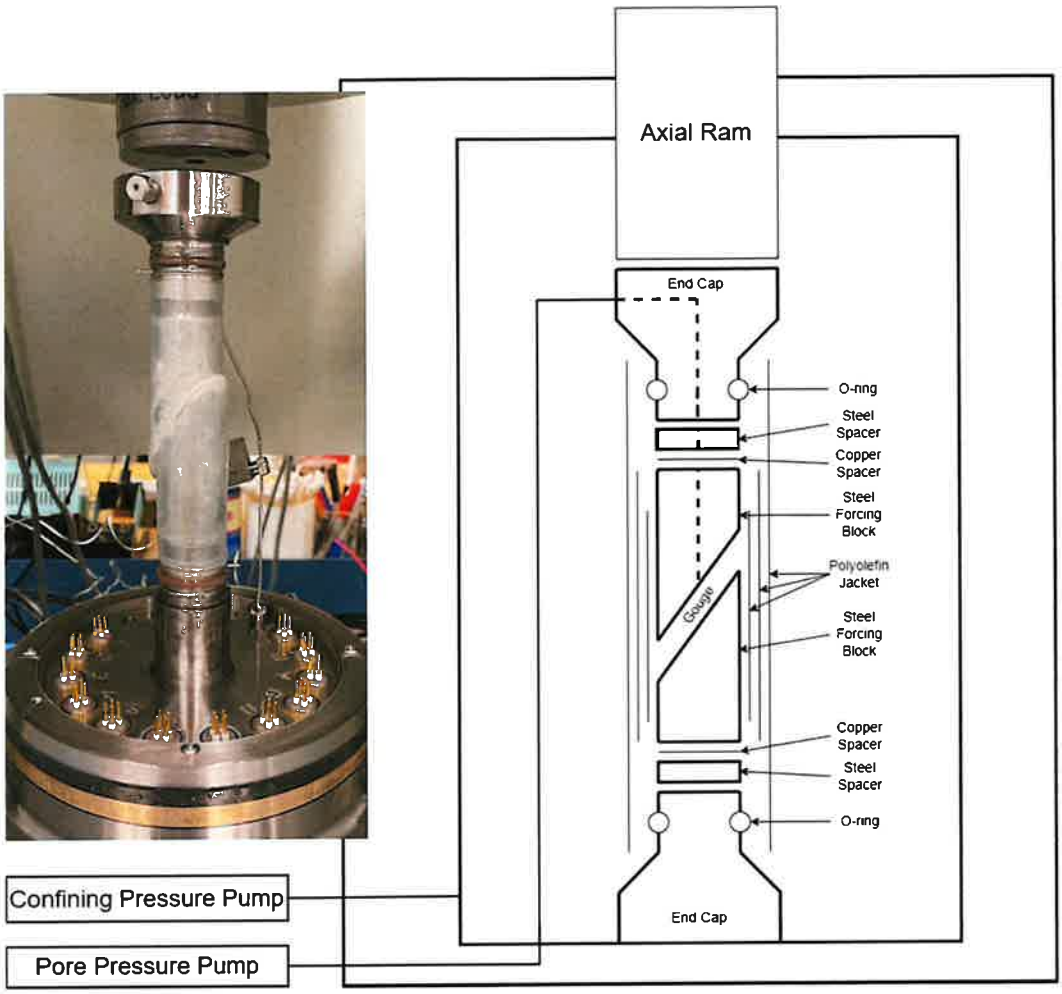

Figure 19. Schematic of experimental setup for triaxial shear tests. A photo shows an actual testing with a gouge sample isolated from the confining medium using three layers of heat shrink polyolefin.

3.1.3.2. Crack Initiation & Formation during Wellbore Breakout

Borehole breakout experiments at a laboratory scale were conducted on SWG samples to evaluate the fracture initiation and propagation from a borehole.

Sample Preparation: A borehole was created by drilling a small hole through the center of a cylindrical sample of Sierra White granite (Figure 20). This geometry utilizes the axial loading ram and confining pressure to create a differential stress around the borehole, as opposed to classic borehole simulations that required multiple rams to achieve similar stress states. The simulated borehole is isolated from the confining medium using ported steel covers, allowing for the independent pressurization of the borehole interior with different fluid chemistries. Samples are

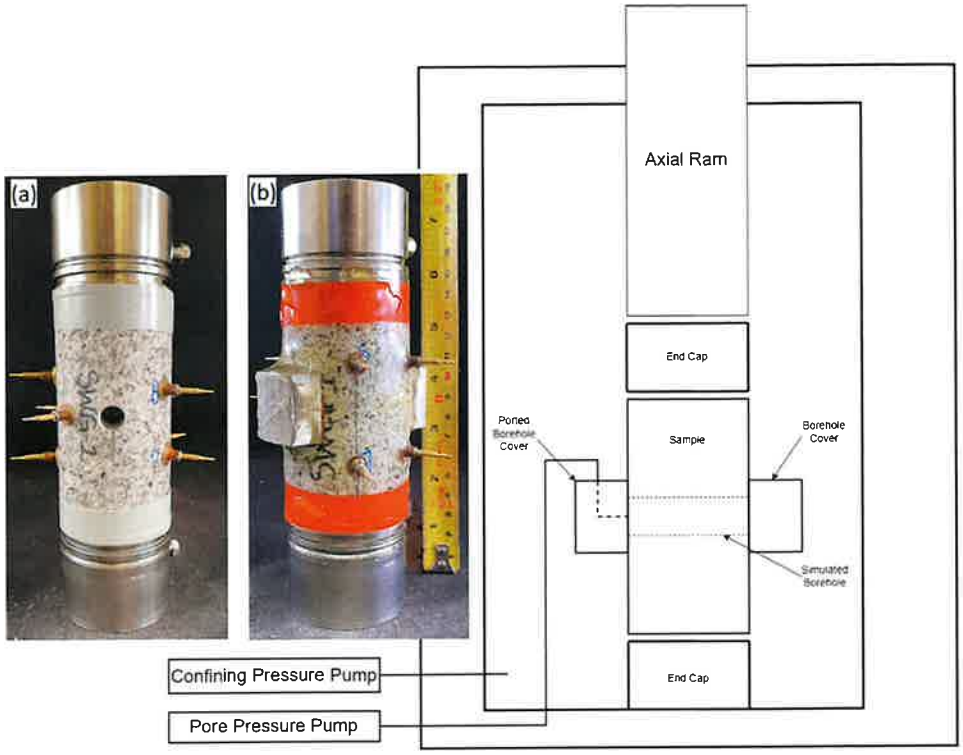

Figure 20. Schematic of experimental setup for wellbore breakout tests. Photos show (a) a simulated borehole in SWG and (b) a polyurethane-jacketed sample with borehole covers. A total of eight transducer pins are used to collect acoustic emission signals during experiments.

jacked with a UV cure polyurethane to isolate the sample from the confining medium. Granite cylinders are 54 mm in diameter and ~95 mm long, and drilled borehole has a 11 mm diameter. Experimental procedures for wellbore breakout testing have been different for dry and wet samples and at room and high temperature conditions as listed in Figure 21.

Sensors: Samples were instrumented with 8 piezoelectric transducers to record acoustic emissions (AE) to monitor damage development and localization along the borehole during deformation. Dynasen© piezoelectric shock pins were employed due to their small size, pressure capability, and thermal rating. Pin mounting technique depended on temperature. For ambient tests, pins were potted into brass waveguides using Wood's metal and affixed to the sample using a 5-minute cure epoxy. For the test at 100 °C, pins were potted into brass waveguides using a steel reinforced epoxy and affixed to the sample using a quick set steel reinforced epoxy. For the 150 °C test, brass waveguides were attached using a steel reinforced epoxy. AE was recorded using a Mistras© Micro-II Express system with an Express-8 eight channel AE board. Signals were pre-amplified with a 60 dB gain and bandpass filtered from 100 to 600 kHz. A hit was recorded with signal levels on a channel that exceeded 31 dB, at which point 250 µsec pre-threshold crossing and 750 µsec post threshold crossing was recorded. Additional front-end filters prevented waveforms that were shorter than 15 threshold crossings or 2 µsec duration above threshold levels from being recorded. These filters helped to screen the significant amount of electrical noise associated with the system. Post testing, AE events were located using ASC© In-Site Lab software. The detailed description is reported in Choens et al. (2025).

TEST PROCEDURES

Tests at Room Temperature

1. Step 1: Apply initial load onto the sample
   - Initial seating load of 1 MPa differential stress between axial load and lateral confining pressure
   - System will adjust axial force to maintain 1 MPa differential stress while confining pressure is increased
2. Step 2: Apply confining pressure @ 1 MPa/min
   - Target of 17.2 MPa for dry test, 20.6 MPa for fluid saturated test
   - For saturated test, add 3.4 MPa pore fluid starting at 6.8 MPa confining pressure. Step up fluid pressure in 100 psi increments while confining pressure is increasing.
   - After reaching the target confining pressure, the system holds pressure. Confining stage lasts a total of 30 min
3. Step 3: Deform axially (vertical) at a displacement rate equivalent to strain rate of $3.3 \times 10^{-6}\ s^{-1}$
4. Once stress plateaus and starts to drop, unload at the same rate ($3.3 \times 10^{-6}\ s^{-1}$) to 5 MPa differential stress
5. Decrease confining pressure at 1 MPa/min to 1 MPa
6. Decrease pore pressure to 0 at 6.8 MPa confining pressure

Tests at High Temperature

1. Apply initial seating load – 1 MPa differential stress
   - Maintained for confining pressure and temperature stages
2. Apply confining pressure @ 1 MPa/min
   - Target of 20.6 MPa for saturated tests
3. Add 3.4 MPa pore fluid starting at 6.8 MPa confining pressure
4. Confining pressure stage lasts for 30 min
5. At the end of confining pressure stage, increase differential stress to 5 MPa
6. Increase temperature to 100°C or 150°C at 1°C/min, maintained overnight
7. Deform axially at displacement rate equivalent to strain rate of $3.3 \times 10^{-6}\ s^{-1}$, measured by axial ram displacement
8. Once stress plateaus and starts to drop, unload at same rate to 5 MPa differential stress (Later tests used a faster rate)
9. Decrease confining pressure at 1 MPa/min to 1 MPa
10. Decrease pore pressure to 0 at 6.8 MPa confining pressure

Figure 21. Procedures for wellbore breakout tests at room and high temperature conditions.

Loading Conditions: Once the load began to drop, the sample was unloaded to prevent the development of throughgoing shear fracture that could damage the jacket. Axial displacement was controlled by displacement of the axial ram as opposed to the displacement of LVDTs mounted on the sample due to connectivity issues at elevated temperature. Loading in this control created a plateau in stress when interfaces were closing; these have been removed from the data in the result. For tests conducted at elevated temperature, the $\Delta\sigma$ was increased to 5 MPa and the vessel was heated at a rate of 1 °C per minute after P_C pressurization until the target temperature of 100 and 150 °C was reached. Samples were allowed to equilibrate overnight before axial deformation as described in Figure 21.

Crack & Fracture Imaging: Samples after testing were imaged using X-ray micro computed tomography (microCT, Zeiss Xradia Versa 620 & 510) and then sliced to construct thin sections in the area of samples with primary fracture features based on micro-CT three-dimensional (3D) images. Thin sections were cut perpendicular to the borehole direction to match CT slices of interest. Micro-fractures and borehole breakout geometries were analyzed in each thin section with a Zeiss LSM 900 microscope using reflected, plane-polarized and cross-polarized transmitted light modes.

3.1.3.2.1 Analysis Techniques for Borehole Breakout Study

Wellbore breakout tests were performed on Sierra White granite (SWG) specimens under different wetting (dry, water/brine/mineral oil wet) and temperature (room, 100 °C, 150 °C) conditions. Experimental procedure is also reported in Choens et al. (2025).

The stresses along the borehole are calculated using Kirsch's solution for a hole in a semi-infinite plate. The analytical solution shows that in the plane perpendicular to the loading direction, the stress concentration is three times greater than the applied load at the borehole wall. Stresses applied parallel to the plane create a stress opposite in magnitude. Hence, the stresses acting along the borehole in the horizontal plane are, σ_{BH}, are:

$$\sigma_{BH} = 3 * \sigma_A - P_C - P_P,$$

where σ_A is the axial stress, P_C is the confining pressure, and P_P is the pore pressure inside the borehole. The stresses acting along the borehole in the plane parallel to the axial loading direction, σ_{BV}, are:

$$\sigma_{BV} = 3 * P_C - \sigma_A - P_P,$$

The borehole is isolated from the confining pressure using a machined steel cover. The cover has an inner diameter that mates to the diameter of the core. A high-pressure port has been machined into the covers on both sides of the borehole. Only one cover is used to access the borehole and the other is plugged to prevent leaks. The open cover is connected to a Hastelloy pore line that runs through the vessel base to a syringe pump.

3.2 Theory: Rate-and-State Friction

An extensive review of hydrothermal friction experiments was performed. Laboratory data was compiled for various fault gouges. The key parameters, such as shear layer thickness, grain size, and permeability, were determined from experimental measurements. The approach to extend rate and state friction relationships to geothermal conditions included:

1) Extension of the microphysical Chen–Niemeijer–Spiers (CNS) model (Mei and Rudnicki, 2023a&b, 2024) to hydrothermal conditions by using the observed temperature variation of indentation hardness to infer the temperature dependence of a microphysical parameter.
2) Formulation of the problem for a fluid-saturated gouge-filled fault (Figure 22). The CNS model was applied that uses the porosity as a state variable. By incorporating the pore pressure evolution in the fluid-infiltrated fault, a theoretical analysis was conducted of the friction model as a function of injection pressure and bulk permeability. Using a single-degree-of-freedom system, fault stability was analyzed for a range of different drainage conditions.
3) The numerical results from the extension of the CNS microphysical model were compared with those for the standard rate-and-state friction law.

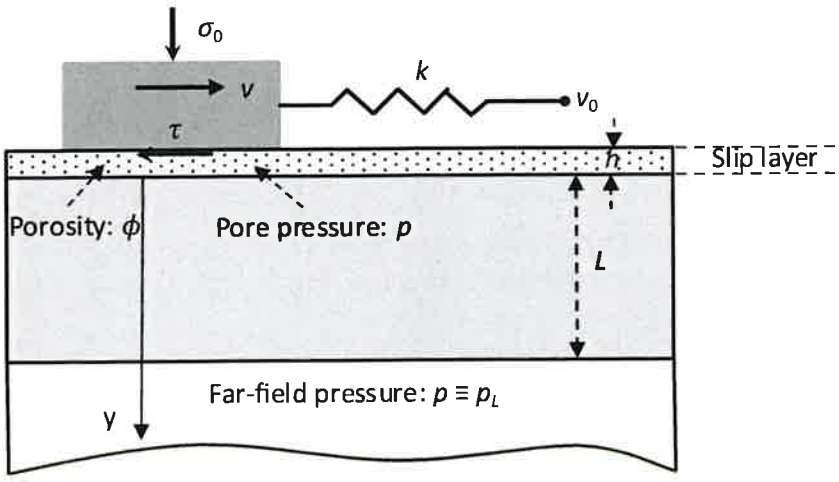

Figure 22. Frictional slip of fluid-saturated faults in a spring-slider model.

3.3 Numerical Simulation of Fracture/Fault Propagation

3.3.1 Computational Methods for Model Update and Validation

Under this project, we developed a 3D visco-poro-plastic, finite deformation, nonlocal Continuum Damage-Breakage (CDB) model in the MOOSE-FARMS (Fault and Rupture Mechanics Simulations), an INL MOOSE-based application for fracture/fault initiation, propagation, coalescence with wave propagation. The details of model algorithm are reported in Zhao et al. (2024). Here we report the latest update that has been used for model validation against wellbore breakout experimental data.

Free Energy Formulation: The CDB model uses damage (cracking) and breakage (granulation) state variables to account for elastic moduli changes during brittle deformation. The total free energy partitions into elastic Ψ_s and granular Ψ_B components:

$$\Psi(T, \mathbf{E}^e, \zeta^e, \alpha, B) = (1 - B)\Psi_s(T, \mathbf{E}^e, \zeta^e, \alpha) + B\Psi_B(T, \mathbf{E}^e, \zeta^e)$$

For the elastic and granular parts, we assume separable contributions to the elastic strain-energy density, fluid energy density. The constitutive equations follow Biot's classical theory of linear, isotropic poroelasticity:

$$\Psi_s = \frac{\lambda}{2} I_1^2 + \mu I_2 - \gamma I_1 \sqrt{I_2} - \beta M \zeta^e I_1 + \frac{1}{2} M \zeta^{e2}$$

$$\Psi_B = a_0 I_1 + a_1 I_1 \sqrt{I_2} + a_2 I_1^2 + a_3 \frac{I_1^3}{\sqrt{I_2}} - \beta_g M_g \zeta^e I_1 + \frac{1}{2} M_g \zeta^{e2}$$

Here, γ is the third modulus that couples volumetric and shear strains in a damaged solid. M and β are the Biot modulus and Biot coefficient for the solid phase, respectively, while M_g and β_g are the corresponding Biot modulus and Biot coefficient for the granular phase. The strain invariants I_1, I_2, and the invariant ratio ξ, as functions of Green-Lagrange strain tensor $\boldsymbol{E}$, are defined as:

$$I_1 = \mathrm{tr}(\mathbf{E}^e), \quad I_2 = \mathrm{tr}(\mathbf{E}^{e2}), \quad \xi = \frac{I_1}{\sqrt{I_2}}$$

Governing Equations: The governing equations are derived from the first and second laws of thermodynamics, ensuring thermodynamic consistency and proper partitioning of material properties between the damaged solid phase and the granular phase. Without presenting lengthy derivations here, the two-field formulation solves for the solid displacement field u and the pore pressure p, with the final strong form in the reference configuration expressed as follows:

Balance of Linear Momentum:

$$\nabla_X \cdot \mathbf{P} = \rho_0 \ddot{\mathbf{U}}$$

where P is the total first Piola-Kirchoff stress tensor, ρ_o is the mass density in the reference configuration, and $\ddot{U}$ is the acceleration. The total first Piola-Kirchoff stress tensor can be derived from the total Cauchy stress tensor using Nanson's formula as follows:

$$\mathbf{P} = J\mathbf{T}\mathbf{F}^{-T}$$

where T is the total Cauchy stress tensor while F, J are the deformation gradient and it's Jacobian, respectively. The total Cauchy stress tensor can be derived from the total elastic second Piola-Kirchoff stress tensor as follows:

$$\mathbf{T}^e = J^e \mathbf{F}^{e-1} \mathbf{T} \mathbf{F}^{e-T}$$

where T^e is the total elastic second Piola-Kirchoff stress tensor while F^e, J^e are the elastic deformation gradient and it's Jacobian, respectively. The total elastic second Piola-Kirchoff stress tensor can be expressed as follows:

$$\begin{aligned}
\mathbf{T}^e = \frac{\partial \Psi}{\partial E^e} &= (1-B)\left[\left(\lambda - \frac{\gamma}{\xi}\right) I_1 \delta_{ij} + (2\mu - \gamma\xi) E^e_{ij}\right] \\
&+ B\left[\left(2a_2 + \frac{a_1}{\xi} + 3a_3\xi\right) I_1 \delta_{ij} + (2a_o + a_1\xi - a_3\xi^3) E^e_{ij}\right] \\
&+ \frac{(1-B)BMM_g(\beta - \beta_g)^2}{(1-B)M + BM_g} I_1 \delta_{ij} \\
&- \frac{(1-B)\beta M + B\beta_g M_g}{(1-B)M + BM_g} p\delta_{ij}
\end{aligned}$$

The total first Piola-Kirchoff stress tensor can be derived directly from the total second Piola-Kirchoff stress tensor as follows:

$$\mathbf{P} = J\mathbf{T}\mathbf{F}^{-T} = JJ^{e-1}\mathbf{F}^e\mathbf{T}^e\mathbf{F}^{eT}\mathbf{F}^{-T} = J^p\mathbf{F}^e\mathbf{T}^e\mathbf{F}^{p-T}$$

Fluid mass conservation:

$$\frac{1}{(1-B)M+BM_g}\dot{p}+\frac{(1-B)\beta M+B\beta_g M_g}{(1-B)M+BM_g}\dot{I}_1+J^p\,\mathrm{tr}(\mathbf{D}^p)$$
$$-\nabla_X\cdot\left((1-B)\,\kappa_R\,\nabla_X(p)+B\,\kappa_{R,g}\,\nabla_X(J^P p)\right)=0,$$

where B is the breakage variable, M, $M_g$are the biot modulus in damaged solid, granular phase, respectively, β,β_g are biot coefficients in two phases, and $\kappa_R,\kappa_{R,g}$ are hydraulic conductivities in the reference configuration for two phases, respectively.

3.3.2 Constitutive Models

The constitutive relations for the poroelastic properties of damaged solid phase and granular phase are presented here. First, the constitutive relation for solid phase is defined as follows:

$$\kappa(\alpha,\phi)=\kappa(\phi)e^{b\alpha}$$

where the permeability tensor $\kappa(\phi)$ describes the porosity-dependent intrinsic permeability of the damage-free material, and b controls the exponential growth of permeability with damage as in Lyakhovsky et al. (2015). The porosity-dependent permeability function follows the power-law empirical relation:

$$\kappa(\phi)=\kappa_o\frac{\phi^3}{\phi_o^3}$$

Porosity evolution is modeled as a function of volumetric strain using the following empirical equation (Katsman et al., 2025):

$$\phi=1-(1-\phi_o)e^{-I_1}$$

The drained bulk modulus K(α) evolves with damage:

$$K(\alpha)=\lambda+\frac{2\mu(\alpha)}{3}-\frac{2\gamma(\alpha)I_1}{3\sqrt{I_2}}$$

Biot coefficient and Biot modulus can be calculated using evolved poroelastic properties as follows:

$$\beta(\alpha)=1-\frac{K(\alpha)}{K_s}$$
$$M(\alpha)=\left(\frac{\beta(\alpha)-\phi}{K_s}+\frac{\phi}{K_f}\right)^{-1}$$

The bulk moduli K_s and K_f represent the compressibility of the solid grains and the pore fluid, respectively.

For granular phase the elastic component of porosity retains its form as in solid phase while the plastic component of porosity depends on the rate of plastic deformation. The permeability of the granular phase evolves according to the adopted power-law:

$$\kappa(\phi) = \kappa_t \frac{\phi^3}{\phi_t^3}$$

where κ_t and ϕ_t are the permeability and porosity at the transition from damaged solid phase to granular phase, respectively. The Biot coefficient in the granular phase is expressed as:

$$\beta_g = 1 - \frac{K^{dr}}{K^s}$$

where K^s is the solid grain bulk modulus, and K^{dr} is the drained bulk modulus for the granular skeleton, computed as:

$$K^{dr} = 2a_2 + \frac{6a_3 I_1}{\sqrt{I_2}} + \frac{2a_o}{3} + \frac{2a_1 I_1}{3\sqrt{I_2}} - \frac{4a_3 I_1^3}{3I_2\sqrt{I_2}}$$

The Biot modulus is then:

$$M_g = \frac{K_s K^f}{K_s\phi + K^f(\beta_g - \phi)}$$

For Damage-Breakage related parameters, the fluidity of the granular phase depends strongly on the breakage parameter, which measures the grain size distribution between the initial coarse granular material and the ultimate state corresponding to a fine powder. Adopting a power-law constitutive relation, we approximate the rate of granular flow by the breakage-dependent relation:

$$D^p = C_g B^{m_1} \|\tau_{\text{eff}}\|^{m_2} \left(\frac{\tau_{\text{eff}}}{\|\tau_{\text{eff}}\|} + \frac{\beta_D}{3}\mathrm{I}\right)$$

where C_g, m_1 and m_2 are the material parameters, B is the breakage parameter, β_D is the dilatancy function, and τ_{eff} is the effective deviatoric stress component. τ_{eff} is derived from the effective plastic stress expressed as follows:

$$T^p_{\text{eff}} = T^p + J^p pI$$

where T^p is the microscopic plastic stress. The dilatancy function evolves as Anand and Su (2005):

$$\beta_D = g_o \left(1 - \frac{\eta}{\eta_{cv}}\right)^r$$

where g_o, η_{cv} and r are material constants. The plastic porosity evolution follows Anand (2017):

$$\dot{\phi}^p = (1 - \phi^p)\mathrm{tr}(\mathbf{D}^p)$$

Evolution equations for damage α and breakage B variables are:

$$\frac{\partial(\alpha, B)}{\partial t} = \begin{cases} \left((1-B)\, C_d\, I_2\,(\xi - \xi_o),\ C_B\, P(\alpha)\,(1-B)\, I_2\,(\xi - \xi_o)\right), & \xi \geq \xi_o \\ \left((1-B)\, C_1\, e^{\alpha/C_2}\, I_2\,(\xi - \xi_o),\ C_{BH}\, I_2\,(\xi - \xi_o)\right), & \xi < \xi_o. \end{cases}$$

We identify the free parameters including C_d (damage rate), C_1,C_2 (damage healing rate), C_B (breakage rate), C_{BH}(breakage healing rate), and C_g, m_1, m_2 (granular flow). Material properties include ξ_o (related to internal friction angle) and model-derived parameters include $\gamma_r, a_0, a_1, a_2, a_3$,P(α).

For nonlocal strain invariant ratio, strain localization typically resolves within narrow damage band during material softening stage, which causes mesh sensitivity issue. It is then important to introduce the nonlocal averaging of damage over a certain radius. Here we adopt integral nonlocal formulation on strain invariant ratio ξ, which is the indicator of strain state of material element.

$$\hat{\xi}(x) = \frac{1}{V_r(x)} \int_V \alpha(s-x)\, \xi(x)\, dV(s),$$

$$V_r(x) = \int_V \alpha(s-x)\, dV(s), \qquad \alpha(x) = \exp\left[-\left(\frac{k\,|x|}{l}\right)^2\right]$$

$$|x| = \sqrt{x^2 + y^2 + z^2}, \qquad k = \left(6\sqrt{\pi}\right)^{1/3}$$

We relate the length scale with grain size of the rock sample (l).

Finally, strain-rate dependent C_d is related to the strain rate by following the calibration in Lyakhovsky et al. (2016):

$$C_d(\dot{\epsilon}_d) = \widehat{C_d} \times \exp\left[1 + m \log_{10}\left(\frac{\dot{\epsilon}_d}{\hat{\epsilon}}\right)\right]$$

Here we choose the strain rate is the deviatoric total strain rate ($\dot{\epsilon}_{ij}^d$) as

$$\dot{\epsilon}_d = \sqrt{\frac{2}{3}\dot{\epsilon}_{ij}^d\, \dot{\epsilon}_{ij}^d}.$$

3.4 Joint Inversion

3.4.1 Machine Learning-driven Geothermal Field Generation & Simulation Models

Subsurface field characterization with fractures is challenging because of lack of enough field data sets to identify small-scale fractures and their complex, non-Gaussian distribution. The recent advance in deep learning offers a new way to process and characterize such complex spatial fields. Specifically, deep generative models have attracted increasing attention due to their ability to well represent data distributions and generate realistic samples including subsurface applications with non-Gaussian channels and fractures (Goodfellow et al., 2014; Kim et al, 2021). In this work, diffusion models were used as the state-of-art generative models that outperform other generative models such as Generative Adversarial Networks and Variational Autoencoders (Chen et al., 2024). Diffusion models are probabilistic generative models that include two processes. The

forward process introduces Gaussian noise into training data, and the reverse process is a denoising process that gradually removes noise to generate new samples. Diffusion models effectively overcome the challenges encountered in aligning the posterior distribution

In this work, the denoising diffusion implicit model (DDIM) (Song et al., 2020) is used to learn the generative mechanism of the potential FORGE site permeability fields from the 500 fractured field realizations as discussed in the next section. DDIM consists of two processes, (1) the forward process, which converts a fractured field sample to an independent and identically distributed Gaussian random field by sequential noising, and (2) the reverse process that denoises a Gaussian random field to a meaningful, fracture field sample as in Figure 21Figure 23. The forward process of DDIM can be defined as:

$$x_t = \sqrt{\alpha_t} x_0 + \sqrt{1 - \alpha_t}\epsilon$$

The reverse process can be expressed as:

$$\hat{x}_{t-1} = \sqrt{\alpha_{t-1}} \hat{x}_0 + \sqrt{1 - \alpha_{t-1}}\epsilon$$

where x_0 is the original image, and $\hat{x}_0$ is the generated image. α_t is a decreasing sequence and $\alpha_t \in (0,1)$. ϵ is the noise used to perturb the image and $\epsilon \sim N(\mathbf{0}, \boldsymbol{I})$. Figure 23 illustrates the forward and reverse process of the selected generative model. Once the model is trained, a user can create a subsurface field of interest from a random noise Gaussian field. We call this input random noise field as latent variables. Therefore, the inversion process becomes searching for the optimal values of the latent variables whose denoised fractured permeability field used as input to forward model to produce temperature and pressure consistent with the observed data set.

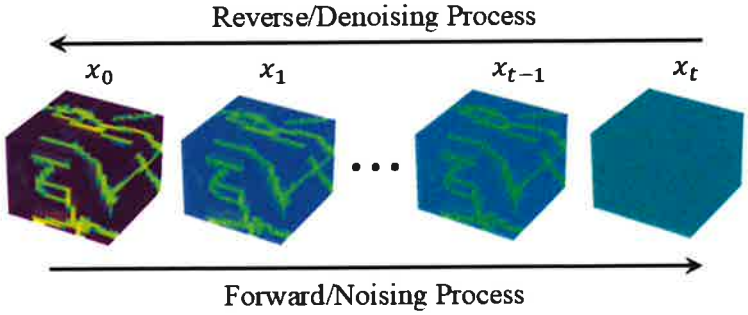

Figure 23. Illustration of the forward and reverse processes of the generative model (DDIM). x_t is a Gaussian random field and x_0 is a fracture field denoised from the random field. Once trained, the generative model will convert a Gaussian random field inputted from users or updated during data assimilation to a field with fractures.

For our application, we first generated a set of natural and hydraulic fractures, and then upscale them to an equivalent permeability field for continuum-based TH simulation as shown in Figure 24. The natural fractures were created using dfnWorks (Hyman et al., 2015) with the fracture model

parameters at the Utah FORGE site (Finnila and Jones, 2024). Figure 24 shows an example of generated fractures and upscaled permeability. The fractures were generated within a 500 m × 500 m × 500 m domain, and the upscaled permeability field has 36 × 36 × 36 blocks (each block is at least 10 m × 10 m × 10 m with 300 m x 300 m x 300 m of the center domain and larger outside the well locations). The upscaling from DFN to permeability field is performed using the upscaled discrete fracture matrix model (UDFM) (Sweeney et al., 2020). The permeability values were adjusted to fit the measured pressure and temperature data from recirculation tests performed in 2024 at the Utah FORGE site (Xing et al., 2025).

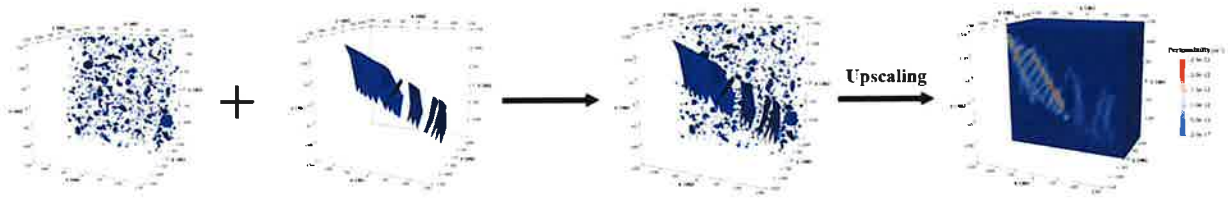

Figure 24. Generated natural (first) and hydraulic (second) fractures and combined fractures (third) were converted to a upscaled permeability field (last).

500 training permeability and porosity fields were generated on 36 x 36 x 36 grids to train the diffusion model. Figure 25 shows training data and deep learning-based generated data. The first row is the permeability data used for training, and the second row shows the data generated by the diffusion model. The trained model can generate fracture properties similar to those of the training data. To illustrate the choice of the diffusion model over other widely used generative models, three examples generated by Wasserstein Generative Adversarial Network (WGAN) (Kim et al., 2021) are presented in the bottom row of Figure 25. It is shown that the fracture connectivity of the samples generated by the generative model DDIM is much better than that of the samples generated by WGAN, which reflects the superior generation ability of DDIM.

3.4.2 Surrogate Geothermal Flow and Heat Transport Simulation Model

Simulations were conducted using an open-source software MATLAB Reservoir Simulation Toolbox (MRST) (Lie, 2019) because of its efficient discretization of the complex permeability fields. The finite element mesh in FALCON requires sophisticated and time-consuming mesh discretization processes and for the inverse problem application where many permeability field candidates need to be evaluated, fast meshing is crucial. For this reason, we tested FALCON and MRST in the synthetic 2D problems based on the FORGE site (Bao et al., 2023) and confirmed two software produced similar results in THM modeling. Still, the join data inversion would require a few thousand simulation runs in practice, which would be very time-consuming, thus a surrogate model was trained using deep learning for faster simulations. The surrogate model architecture is shown in Figure 26. We used the U-net architecture (Ronneberger et al., 2015), which is well-known for capturing spatio-temporal feature changes, and thus time-varying pressure and temperature were reproduced using the U-net architecture. The model takes the upscaled permeability as input and outputs time series pressure maps. As shown in Figure 26, the

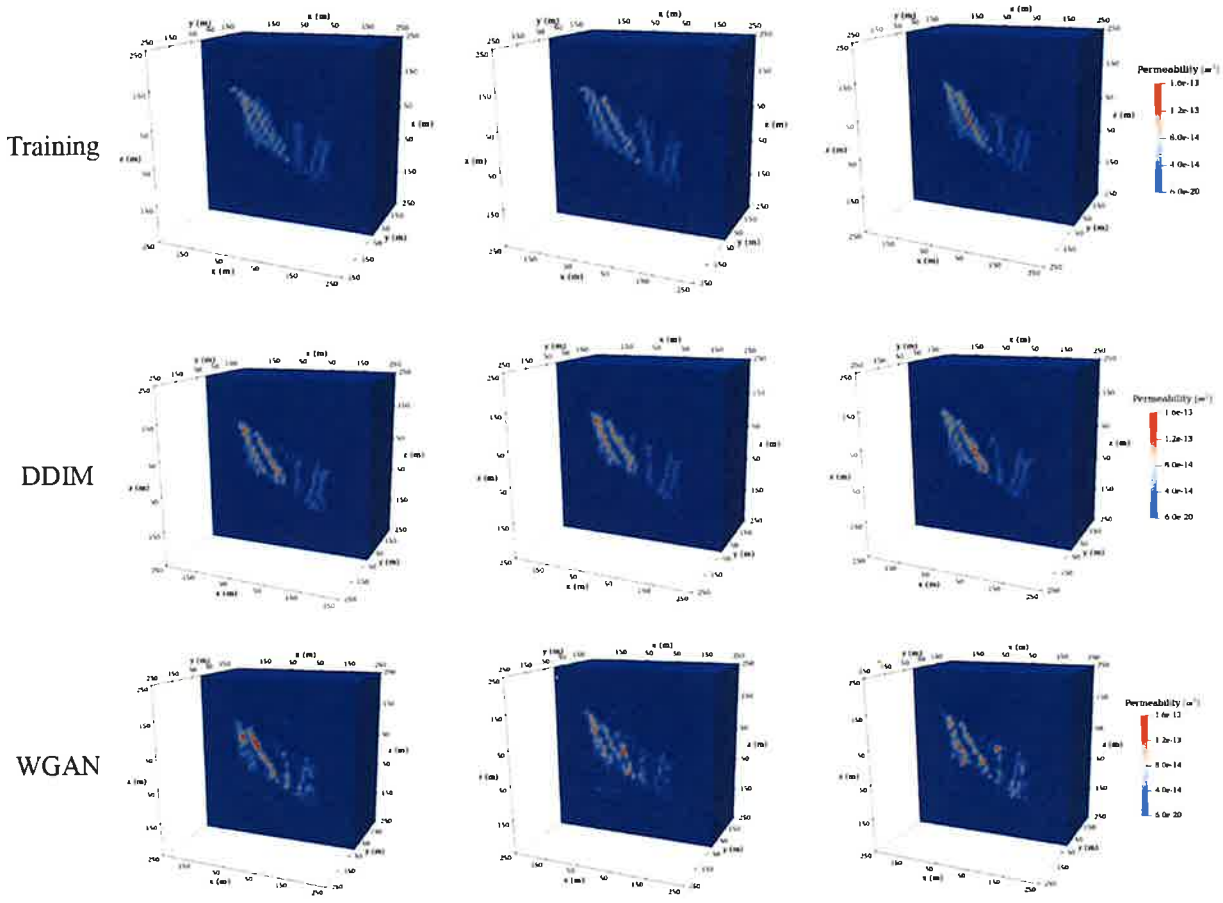

Figure 25. Examples of training and generated permeability fields. The first row shows the training data, the second row is the data generated by DDIM, and the third row is the data generated by another generative model Wasserstein generative adversarial network (WGAN) for comparison.

arrows represent different operations with the black arrows for convolutions over the inputs, the red arrows for max pooling, which is used as a down sampling operation to reduce the dimensions of feature maps, and the blue arrows are self-attention layers, which allow the model to look at how each part of the feature maps relates to other parts. It is noted that the self-attention was not used in the original U-net architecture, however, in this work we use the self-attention to improve the performance of the surrogate model. The green arrows indicate up-sampling to increase the dimensions of feature maps and the gray arrows represent skip connections between down-sampling and up-sampling processes, copying the feature maps from down-sampling to up-sampling.

3.4.3 Site Characterization

Once the permeability generation and numerical simulation models are constructed, the permeability field that can produce field-observed pressure and temperature at wells are searched. In this work, we used Ensemble Smoother with Multiple Data Assimilation (ES-MDA) (Emerick

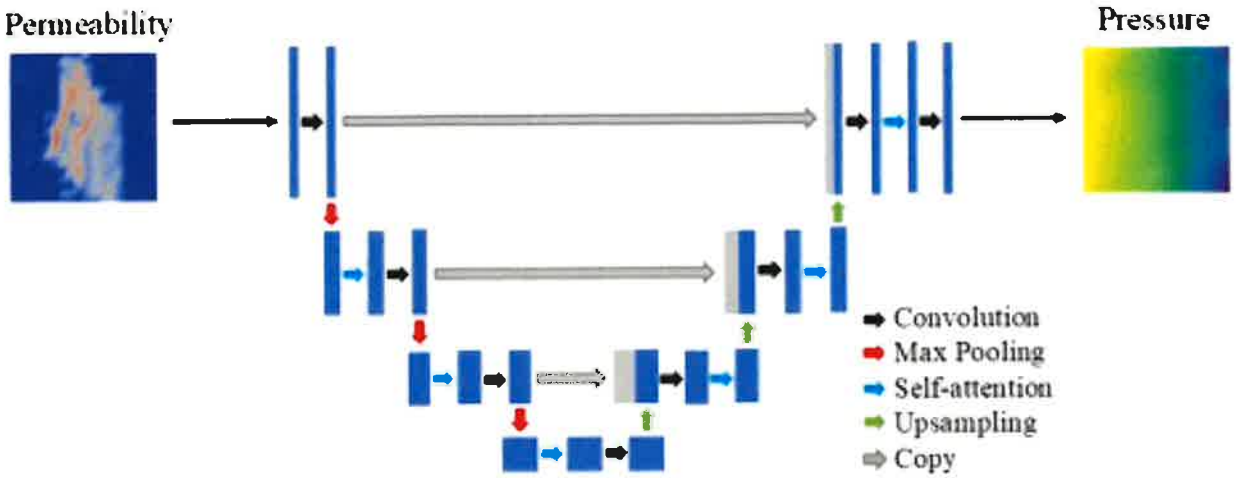

Figure 26. Surrogate model based on the U-net architecture. The blue boxes represent feature maps, and the gray boxes indicate the copied features. The arrows represent different operations.

and Reynolds, 2013) for its versatile inverse modeling capability with joint data sets and the updating process is defined as:

$$\boldsymbol{z}_j^{i+1} = \boldsymbol{z}_j^i + \boldsymbol{C}_{\boldsymbol{ZD}}^i \left(\boldsymbol{C}_{\boldsymbol{DD}}^i + \alpha_i \boldsymbol{C}_{\boldsymbol{D}}\right)^{-1} \left(\boldsymbol{d}_{uc,j}^i - \boldsymbol{d}_j^i\right), j = 1, \cdots, N_r$$

where $\boldsymbol{z}_j^i$ is the input of the generative model, i.e., the so-called latent variables, of j-th ensemble member at i-th iteration, $\boldsymbol{C}_{\boldsymbol{ZD}}^i$ is the cross-covariance between the latent variables and the simulated data, $\boldsymbol{C}_{\boldsymbol{DD}}^i$ is the auto-covariance of the simulated data, $\boldsymbol{C}_{\boldsymbol{D}}$ is the observation error covariance, and $\boldsymbol{d}_{\boldsymbol{uc}}$ is the perturbed observation data defined as:

$$\boldsymbol{d}_{uc} = \boldsymbol{d}_{obs} + \sqrt{\alpha_i}\, \boldsymbol{C}_{DD}^{\frac{1}{2}}\, \epsilon_d$$

where $\boldsymbol{\alpha_i}$ is the inflation coefficient of the i-th iteration ($\alpha_i = N_a$ where N_a is the number of iterations) and $\epsilon_d \sim \boldsymbol{N}(\boldsymbol{0}, \boldsymbol{I})$. The workflow of coupling DDIM with ES-MDA is shown in Figure 27.

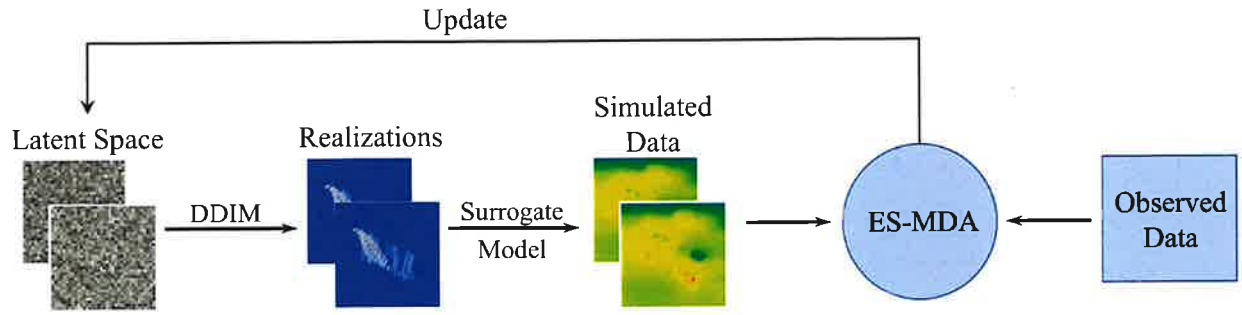

Figure 27. The workflow of coupling DDIM with ES-MDA. The forward model used here is the trained surrogate model based on the U-net architecture.

3.4.4 Field Site Modeling Set-up

A 9-hour circulation test was conducted between the injection well 16A(78)-32 and the production well 16B(78)-32 in April 2024 to confirm the hydraulic connection between injection and production wells created during a stimulation operation, and a one-month long-term circulation test was conducted in August - September 2024 to observe the long-term pressure and temperature responses (Xing et al., 2025). We used the pressure data from the April 2024 circulation test for the site characterization during model calibration step, and then the estimated permeability field from model calibration was used for validation of our estimate by comparing the simulation results from the estimate with the observed pressure and temperature responses at the long-term 2024 circulation test at the Utah FORGE site.

The model settings for April 2024 simulations are shown in Figure 28. A constant pressure of 2596 psi and 3292 psi and a constant temperature of 171°C and 213 °C were imposed on the top and bottom boundaries, respectively. The boundary and initial conditions are from the FORGE Phase 3 native state model (Liu et al., 2022). Seven injection points and seven production points were placed for recirculation simulation. The injection and production rates are shown in Figure 28b. The injection water temperature is 8 °C.

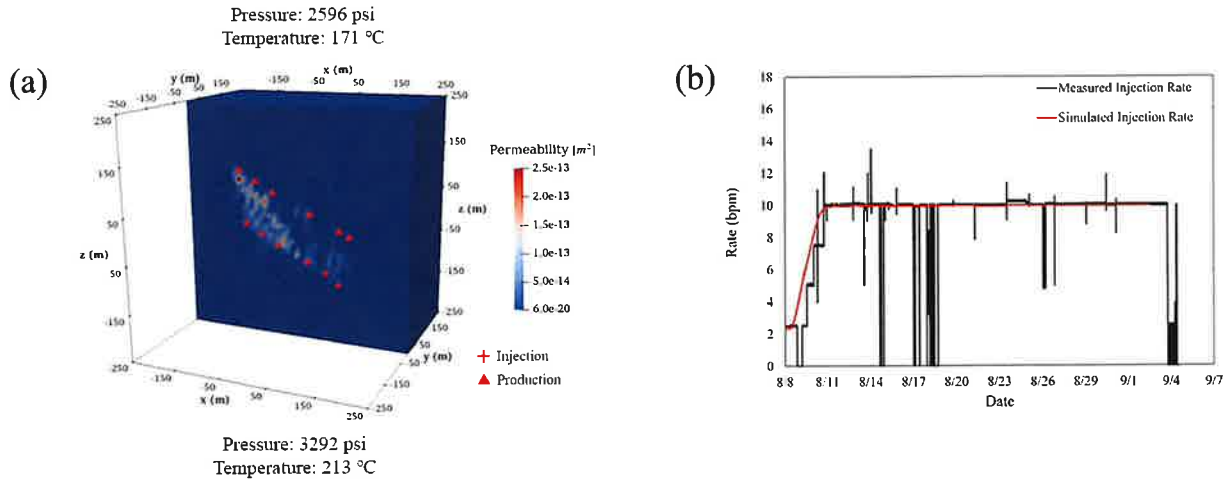

Figure 28. (a) Model settings for the April 2024 circulation test: 2596 psi pressure and 171 °C temperature applied to the top boundary and 3292 psi pressure and 213 °C temperature applied to the bottom boundary. The red crosses are injection points, and the red triangles are production points; (b) Injection and production rates.

Additional circulation test was conducted from August to September 2024, lasting about one month (Xing et al., 2025). The 1-month circulation test was conducted to evaluate the long-term thermal performance of the FORGE geothermal system. The estimated permeability field was used to simulate the 1-month circulation test. The model setup is similar to the model configuration of the April 2024 circulation test as shown in Figure 29. Figure 29b shows that the initial injection

rate is 2.5 bpm and gradually increased to 10 bpm within three days. The production rate is constant at 9 bpm and the simulation was conducted for 26 days.

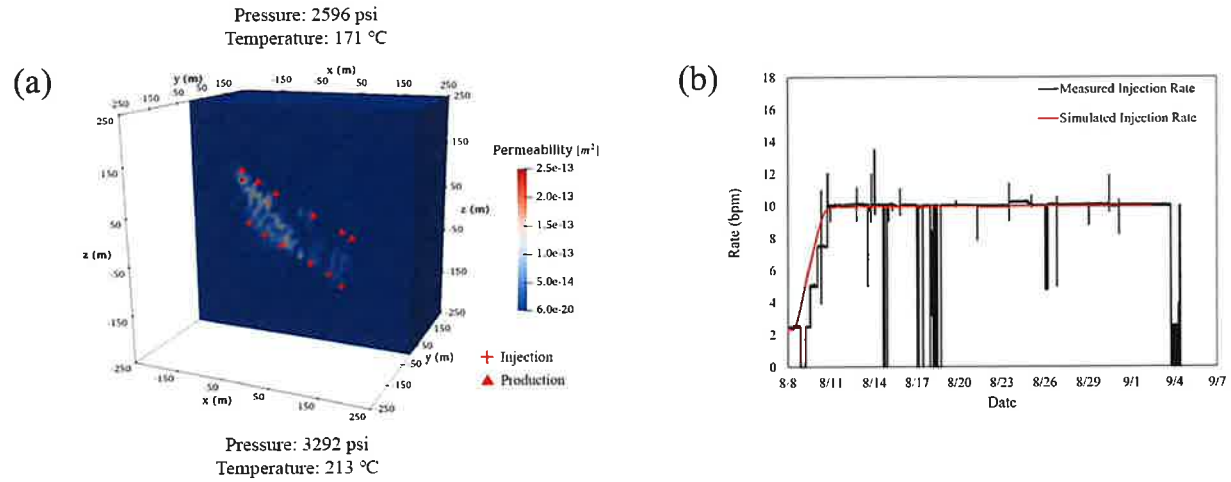

Figure 29. (a) Model settings for the August-September 2024 circulation test: 2596 psi pressure and 171 °C temperature applied to the top boundary and 3292 psi pressure and 213 °C temperature applied to the bottom boundary. The red crosses are injection points, and the red triangles are production points; (b) Injection and production rates.

Results and Discussion

4.1 Key Results

4.1.1 Experiments

4.1.1.1 Geophysical Monitoring of Fractures Undergoing Shear

B-Value Tests: Figure 30 displays the evolution of the B-values with back pressure for three Sierra White granite specimens. A back pressure of 5.0 ~ 5.5 MPa was needed for Sierra White granite, with the measured B-values ranging from 0.84 ~ 0.87. The values are consistent with those from Barre granite, 0.78 ~ 0.84 under an effective stress of 0.34 MPa (Adachi & Mesri, 1973). Although the B-value is dependent on the effective stress, the back pressure required for full saturation is independent of the effective stress (Mesri et al., 1976; Chiu et al., 1983). As a result, the back pressure values obtained from this study may be applied to different test setups at different effective stresses for Sierra White granite.

Direct Shearing Tests: The results of direct shear tests are summarized in Table 1. The peak shear strength as a function of the effective normal stress is shown in Figure 31. The peak friction angle of Sierra White granite specimens in the dry conditions was 66.4°. The test results indicate that the shear behavior of saturated fractures was not significantly affected by temperatures up to 100°C. The peak shear strength appears to decrease with saturation but increase with temperature. The peak friction angle changed by at most 2-3°, which is not significant considering experimental error.

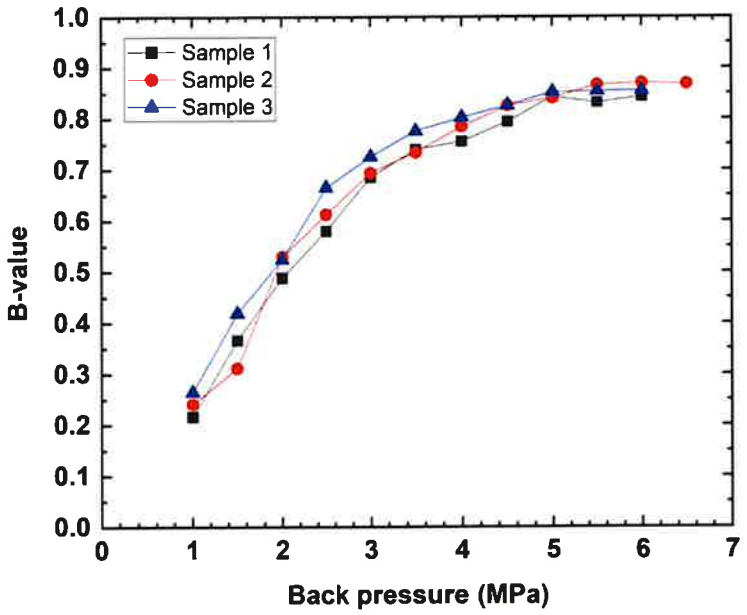

Figure 30. Evolution of the B-values with back pressure for Sierra White granite.

Table 4. Direct shear test results on Sierra White granite.

Conditions	Specimen	Effective normal stress (MPa)	Peak shear strength (MPa)	Peak friction angle (degrees)
Dry fractures at room temperature	Sample 1	2.00	4.52	66.1
	Sample 2	2.00	5.39	69.7
	Sample 3	2.00	4.69	66.9
	Sample 4	2.00	4.67	66.8
	Sample 5	3.00	6.90	66.5
	Sample 6	4.00	8.69	65.3
Saturated fractures at room temperature	Sample 7	1.92	5.00	69.0
	Sample 8	2.10	4.28	63.9
	Sample 9	1.76	3.20	61.2
Saturated fractures at 50°C	Sample 10	6.00	15.66	69.0
	Sample 11	6.00	15.57	68.9
Saturated fractures at 100°C	Sample 12	6.00	14.59	67.6

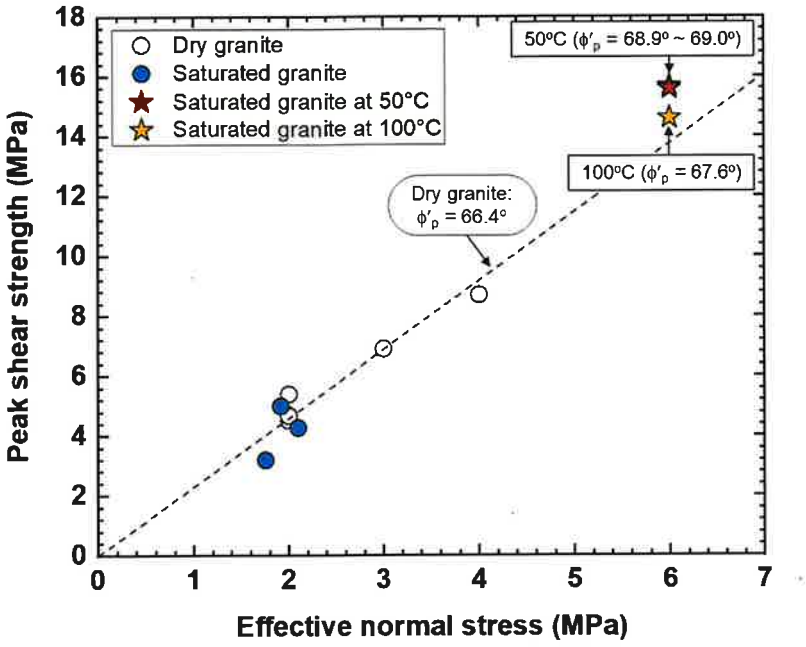

Figure 31. Summary of results of direct shear tests.

Figure 32 shows the shear stress as a function of time (black curve) for dry (Figure 32a) and saturated (Figure 32b) fractures in granite under an effective normal stress of 2 MPa and at room temperature. The shear stress increases with time until the rock fractures attain the peak shear strength. Subsequently, the shear stress decreases and approaches the residual shear strength.

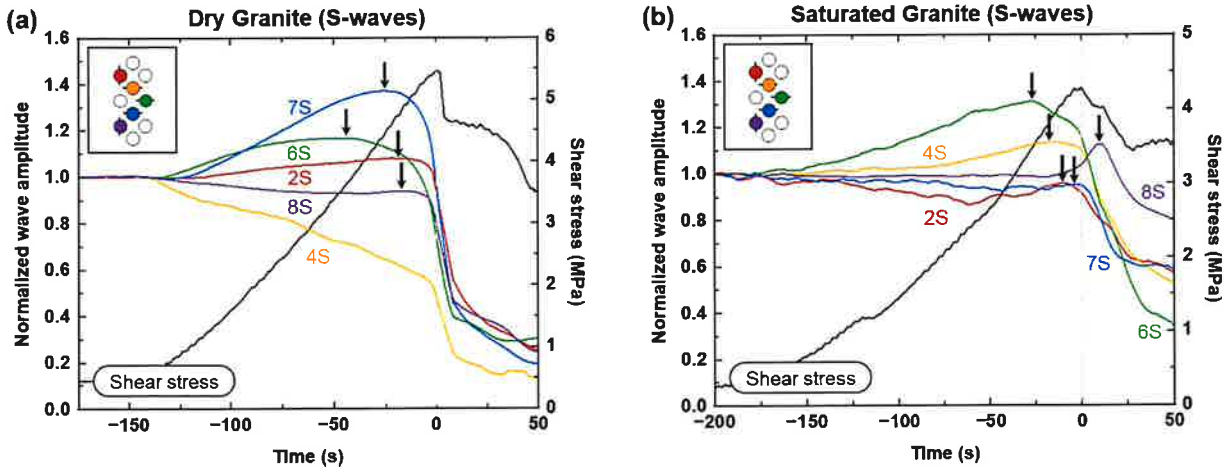

Figure 32. Transmitted S-wave amplitude: (a) Dry granite; (b) Saturated granite. Downward arrows mark the peak in wave amplitude.

The amplitudes of the transmitted S-waves for dry and saturated fractures are also shown in Figure 32. The transducer positions (inset Figure 32) and their recorded wave amplitudes are color-

coded. The magnitude of the amplitudes is directly related to the behavior of the local contact surface sampled by the transducer. An increase in normal or shear stiffness in the area monitored by the transducer increases the amplitude in transmission of P- and S-waves, respectively (Pyrak-Nolte et al., 1990). The opposite is also the case; a decrease in stiffness, normal or shear, translates into a decrease in the corresponding wave amplitude. Thus, as the shear stress in the discontinuity increases, better contact among asperities occurs, as well as asperity interlocking. This is associated with an increase in the amplitude of the transmitted (and converted) waves. When the shear stress exceeds the shear strength of local asperities, damage may be produced at the local contact, and a decrease in stiffness occurs, and thus, a reduction in transmitted and converted wave amplitudes is yielded. As a result of the reduction, a peak in transmitted and converted wave amplitudes is produced. Such peaks, when observed prior to the macroscopic failure of the frictional discontinuity, are taken as a precursor to failure of the discontinuity (Hedayat et al., 2014a, b; El Fil, 2021).

This trend is generally observed in the data displayed in Figure 32. However, not all transducers follow the ideal trend described. Indeed, similar experiments in perfectly matched, homogeneous, and uniform frictional surfaces consistently show the pattern described: an increase in amplitude of the transmitted and converted waves, a peak or precursor to failure before the peak shear stress, followed by a decrease in amplitude (Hedayat et al., 2014a, b; El Fil, 2021). However, when the discontinuities are mismatched (e.g., large voids between the two contact surfaces), experimental observations suggest that the changes in amplitude depend strongly on the characteristics and evolution of the local contact. For example, large shear displacements that are needed to enhance contact may delay or prevent the peak, such as from dilation (Han, 2024). Also, increased normal stress may improve contacts, i.e., decrease voids in the discontinuity, and thus change the evolution of the amplitude with shear compared to tests at lower normal stresses (El Fil et al., 2024). Given that the method used to create the discontinuity (the Brazilian technique) creates mismatched, non-planar discontinuities, it is expected that the results reflect the diverse conditions of the fracture geometry at the local scale.

The black arrows in the figures indicate the peaks in the wave amplitudes. The peaks are chosen such that they reflect the location of maximum amplitude. If more than one peak is produced, the first one is chosen. They may be observed before (precursors) or after the peak shear strength is achieved. However, there are cases when no peak occurs, so no arrows are displayed. Those occur for P-waves in transmission and S-to-P and P-to-S converted waves in saturated tests (discussed later).

Figure 32 includes plots of the transmitted waves in granite for dry and saturated tests. Please note that actual values of the magnitude depend on the normalization used, where wave magnitudes are normalized by their values prior to shear. Here, the discussion is based on the relative change in magnitude with load. Inspection of the data for transmitted S-waves (Figure 32) suggests that there is no noticeable effect of water saturation on the overall response in transmitted S-wave amplitude. However, some S-wave transducers exhibit different geophysical responses when compared to other transducers. Signals from transducer 4S from the dry granite specimen (Figure 32a) show a continuous decrease in S-wave amplitude without any increase. From transducer 8S on the saturated granite specimen (Figure 3b), the data exhibit a peak in amplitude but slightly later than the peak shear strength. This contrasts with most S-wave transducers that demonstrate peaks prior

to the peak shear strength. Those differences are caused by the local contact that is monitored by each transducer. As mentioned earlier, a decrease in amplitude may indicate a reduced contact (due to e.g., dilation), which may be followed by an increased amplitude (due to e.g., improved local contact with further shear), and the peak may not be observed or may occur after the macroscopic failure (due to e.g., large slip needed to improve local contact). The amplitude graphs reflect the complex behavior resulting from the diverse contact conditions under each transducer, which evolve with local compression and slip. The changes in signal amplitudes provide insight into the local mechanical response of the discontinuity.

Figure 33 shows the amplitudes of the transmitted P-waves for the dry and saturated fractures in granite. As shown in Figure 33a, P-wave transmission across the dry fractures shows behavior similar to the transmitted S-waves: an increase in transmission with shear, a peak, and subsequent reduction with further shear. However, under saturated conditions, the trend in P-wave transmission differs from that of dry fractures, as shown in Figure 32b: the transmitted P-wave exhibits initially either a monotonic decrease or a small change in amplitude, and it is followed by a later, somewhat sudden reduction in amplitude. This finding is explored in detail later.

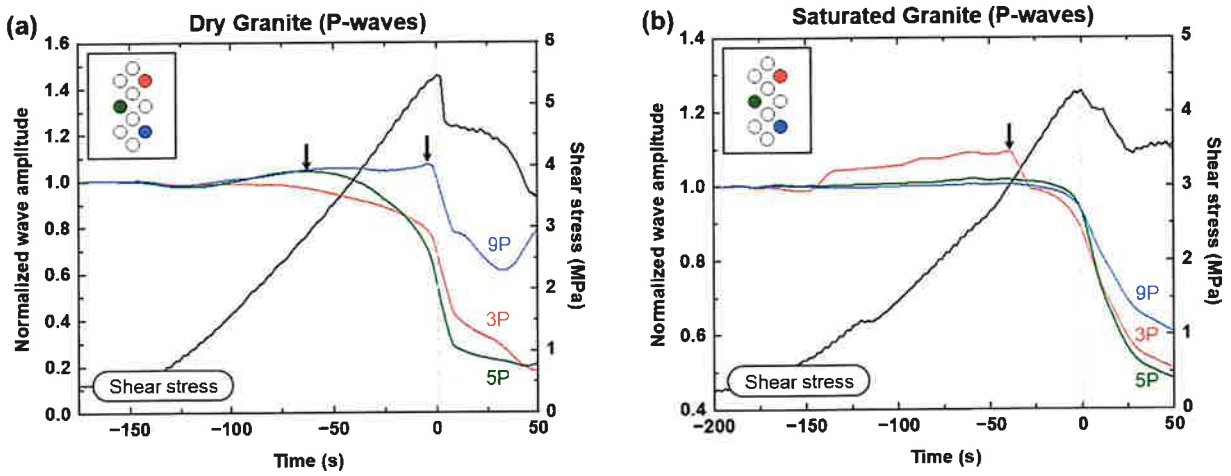

Figure 33. Transmitted P-wave amplitude: (a) Dry granite; (b) Saturated granite. Downward arrows mark the peak in wave amplitude.

Figure 34 and Figure 35 are analogous to Figure 32 and Figure 33, but with the results from converted wave amplitudes (P-to-S or S-to-P converted waves). The data in Figure 34 and Figure 35 reveal that the converted wave amplitude behaves consistently with the transmitted wave amplitude. Under dry conditions, most transducers show a peak in converted wave amplitude, followed by an amplitude reduction prior to the peak shear strength, as shown in Figure 34a for S-to-P converted waves and in Figure 35a for P-to-S converted waves. Interestingly, most converted waves across saturated fractures exhibit either a continuous decrease or a change/increase in the wave amplitude, as shown in Figure 34b and Figure 35b, while some transducers (3P & 9P of saturated granite) show peaks in converted wave amplitude. The converted wave amplitude is similar to the P-wave transmission under saturated conditions, rather than the S-wave transmission.

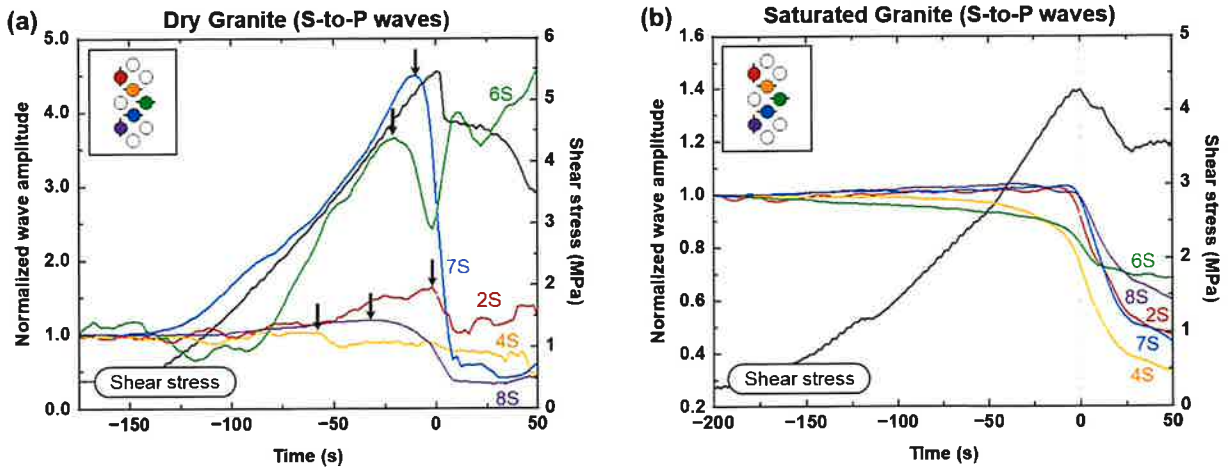

Figure 34. Converted S-to-P wave amplitude: (a) Dry granite; (b) Saturated granite. Downward arrows mark the peak in wave amplitude.

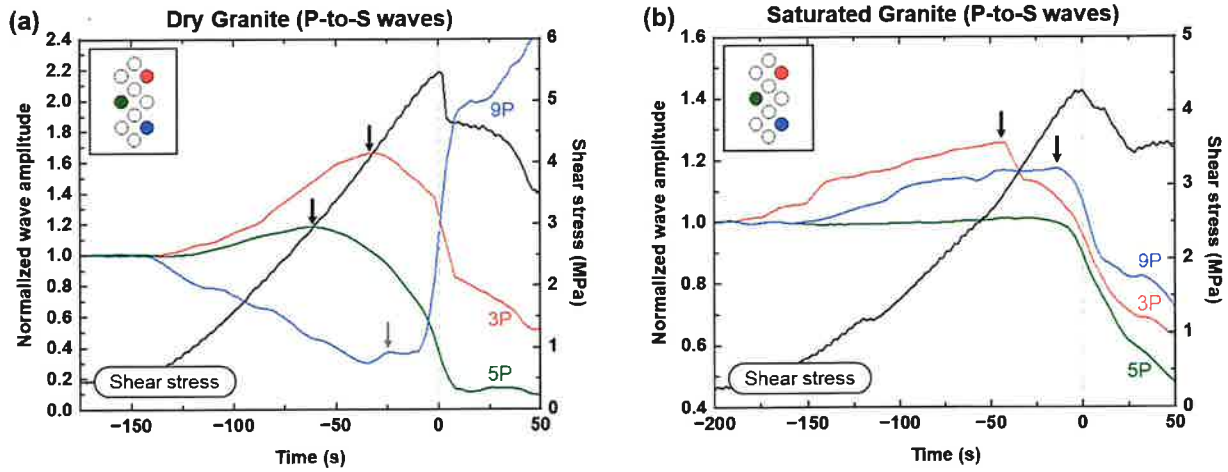

Figure 35. Converted P-to-S wave amplitude: (a) Dry granite; (b) Saturated granite. Downward arrows mark the peak in wave amplitude.

Figure 34 (S-to-P converted waves) shows that the amplitudes of the converted waves have significant fluctuations during shear, in contrast to the much smoother curves from the P- and S-waves. This is caused by the much smaller amplitude of the S-to-P and the P-to-S waves than the P- and S-waves amplitudes, as one can see in Figure 4 and Figure 5. Such small magnitudes introduce uncertainty in determining amplitudes using the windowing and wavelet process described earlier. This issue may be related to inconsistencies found between converted and transmitted waves. For example, the signals from transducer 4S in Figure 34a and 9P in Figure 35d exhibit a peak in converted wave amplitude even though they did not show peaks in the transmitted data (e.g., transducer 4S in Figure 32a and 9P in Figure 33b). In addition, the data from transducer 9P from the dry granite specimen (Figure 35a) show a small peak in the converted wave amplitude prior to macroscopic failure, followed by a larger peak post-failure. Again, these

differences may be the result of the low resolution of the converted waves that have much smaller amplitudes than the transmitted wave amplitudes.

During shear, the amplitude behavior of transmitted waves across dry fractures can be explained by the evolution of fracture specific stiffness and actual contact area between fractures (Hedayat et al., 2014a, 2014b, 2018; El Fil et al., 2024). For most transducers, an increase in P- or S-wave transmission is observed in the early to mid-stages of the tests, at the time generally between -150 s to -50 s, due to asperity interlocking and enhanced contact area with shear. With further shear, a peak (maximum) and a subsequent reduction in transmitted wave amplitude occur. This is interpreted as a decrease in local fracture stiffness due to the onset of damage to the area probed by the transducer. Thus, the peaks in the transmitted wave amplitudes observed prior to the peak shear strength can be considered seismic precursors to the shear failure of the rock. Some of the peaks, however (e.g., transducer 8S in saturated granite in Figure 16), occur after the macroscopic failure of the fracture. Our interpretation is that, in mismatched surfaces, large shear displacements may be needed to create local contact between the asperities. Thus, enhanced contact or damage may induce the delayed peaks in the amplitude. This is not the case for perfectly matched surfaces, where all the peaks in amplitude occurred prior to the macroscopic shear failure (Hedayat et al., 2014a, 2014b, 2018; El Fil et al., 2024).

As discussed earlier, some differences are observed in the transmitted mode: no precursors or late peaks with a large initial drop in wave amplitude after the peak shear strength. Those differences can be understood by linking the evolution of the contact area in the field of view of the wave sensor with wave amplitude (El Fil et al., 2024). Some transducers show almost no change or even a decrease in amplitude with shear, e.g., transducers 3P and 4S for dry granite (Figure 32a and Figure 33a). Such reduction is attributed to a decrease in the local contact area between the two fracture surfaces due to dilation or local reduction of normal stress. Transducer 8S for saturated granite (Figure 32b) shows a small change and a later increase in amplitude, then displays peaks after failure. Given the mismatched nature of the contact surfaces, this observation is interpreted as the local contact area requires a larger shear displacement to improve the contact and asperity interlocking.

Under dry conditions, the converted wave amplitude shows a similar behavior to the transmitted wave amplitude, as shown in Figure 34 and Figure 35. The magnitude of the converted waves depends on the cross-coupling fracture specific stiffness and the orientation of the apertures/microcracks between the fracture interfaces (Nakagawa et al., 2000). As the converted wave is directly associated with the contact area between two fracture surfaces and with the change in fracture stiffness, its response is similar to the transmitted wave, and its peak can also be taken as a precursor to shear failure (El Fil, 2021; Gheibi et al., 2021). However, as mentioned earlier, most S-to-P signals and a few P-to-S signals do not have a smooth evolution of magnitude with shear displacement and display some inconsistencies with the transmitted waves. For example, there are peaks in converted wave amplitude not found in transmission, or there are peaks in converted after the peak shear strength, but not prior to the peak shear strength. These discrepancies may be attributed to the low resolution of the converted modes that have a smaller amplitude than the transmitted, which makes analysis of the signals more difficult.
a

As discussed for dry fractures, the peak amplitude occurs because of an increase in contact and asperity interlocking between the two fracture surfaces, leading to the enhancement of fracture stiffness. Under saturated conditions, the S-wave transmission displays behavior similar to that of dry fractures (Figure 32b), while the P-wave transmission shows either a monotonic reduction or a very small change in the wave amplitude with shear (Figure 33b). Figure 34 and Figure 35 also show that the converted wave amplitudes from the saturated fractures exhibit a response similar to the transmitted P-waves. That is, they have a very slight peak or a continuous decrease in amplitude prior to failure. The results indicate that P-waves may be affected by the water saturation, in contrast to what happens with S-waves.

To investigate those observations, a comparison of P-, S-, and S-to-P wave amplitudes recorded by the same S-wave transducer was conducted. A full waveform measured by an S-wave transducer can capture both a P-wave and an S-wave signal, as well as the converted S-to-P wave signal, as shown in Figure 4b and Figure 5b. This enables a direct comparison between those wave signals because they propagated across the same fracture area and with the same sensor, thereby reducing any potential sensor and material variability. Thus, those waves captured by the same S-wave transducer experience the same evolution of the actual contact area undergoing shear.

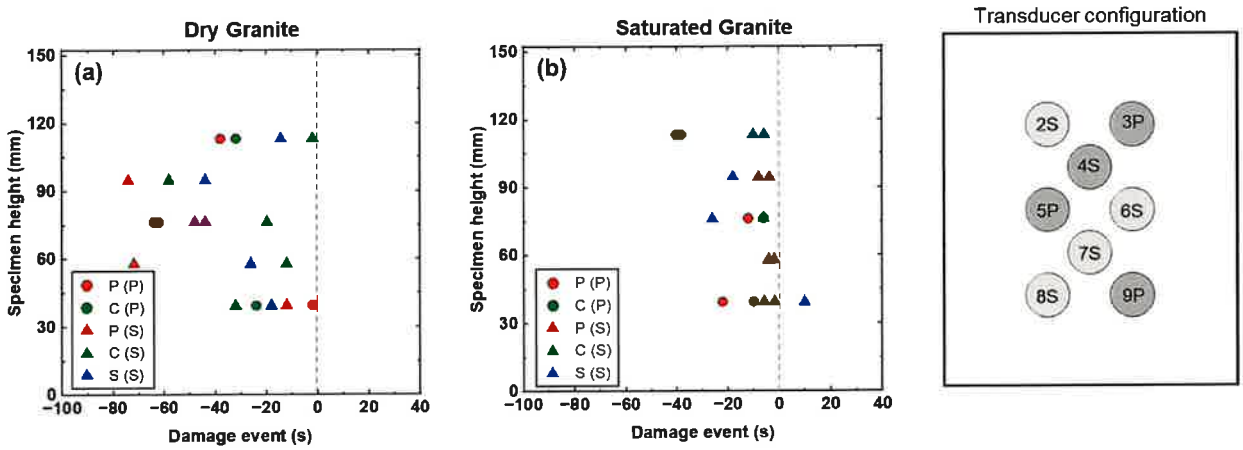

Figure 36. Sequence of damage events along rock fractures: (a) Dry granite; (d) Saturated granite. The first letter to describe the event is the type of measured signal and the second is the transducer type, e.g., C (S) is a converted wave signal measured by a S-wave transducer

The peaks and abrupt rate reductions in wave amplitudes, as mentioned, correspond to the onset of a local damage event to the fracture. The location of the damage events along the height of the specimen can be taken as an indication of the sequence of the local slip that occurs along the fracture. Figure 36 shows the distribution of damage events for dry and saturated fractures in granite. Note that, in the figures, the further the event are from the peak shear stress, the earlier the event occurs. It is important to mention that the shear load is applied to the top of the specimen, i.e., at the 152.4 mm height location. The sequence of the damage events generally shows a downward trend along the fractures, with the transducers at the top (152.4 mm height) detecting damage earlier than the transducers at the bottom (0 mm height). This observation implies that local slip/damage initiated at the top of the specimen and, with shear, propagated along the fractures from top to bottom. This observation agrees with previous findings that suggest that slip

along the contact surface is a progressive failure rather than a sudden event (Ohanaka & Shen, 1999; Mutlu & Bobet, 2006; McLaskey, 2019; Ji et al., 2022).

Figure 36 includes events that were identified after failure, i.e., Figure 36b. As previously mentioned, non-mated surfaces may have locations where larger slip may be needed so the two surfaces achieve contact. Because of that, precursors to failure/local damage at these locations may occur much later than at other locations in the fracture where the contact was initially tight. This finding points to some of the differences expected between laboratory and field observations, since at the field scale, the aperture size, contact area, etc., would be much larger than in the laboratory. Thus, for field applications, the size of the probing area needs to be scaled with the wavelength of the signals.

Figure 37 displays the evolution of the shear stress of granite fractures at 50°C and 100°C as a function of shear displacement, along with temperature and pore pressure. For convenience, the shear displacement at the peak shear strength is set to zero. During the shear test, the temperature recorded by the thermocouple located at the bottom of the chamber was used for the study. The pore pressure, 1 MPa, was held constant during the test. At the start of the test, after some seating deformations, the shear stress along the fracture linearly increased with shear displacement. Then, the shear stress suddenly and significantly decreased after the peak shear strength. The peak friction angles of the fractures at 50°C and 100°C were 69.0° and 67.6°, respectively, similar to that measured by Han et al. (2024b), who performed shear tests on saturated granite fractures at room temperature.

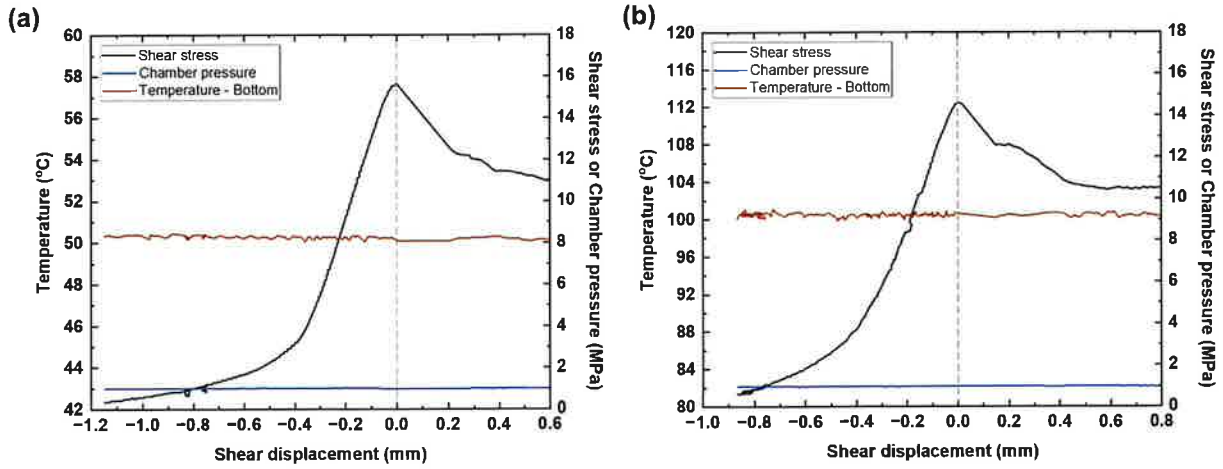

Figure 37. Evolution of shear stress of granite fracture as a function of shear displacement: (a) Sample 10 (50°C); (b) Sample 12 (100°C). Included in the figure are the temperature and pore pressure.

Changes in transmitted wave amplitudes are graphed as a function of shear displacement in Figure 38. As observed in Figure 38, the transmitted wave amplitudes increased with shear. Such an increase, as mentioned earlier, is attributed to the enhanced contact caused by asperity interlocking. Thus, an increase in transmission indicates an increase in fracture specific stiffness of the local area probed by the transducers. At some point, the transmitted wave amplitudes reached their peaks

(maxima) and subsequently began to decrease (the peaks are indicated by arrows in the figure). This decrease denotes a reduction in the local specific stiffness of the fracture, which can be interpreted as the onset of damage to the local fracture in the area probed by the transducer. This trend is consistent with previous studies at room temperature (Hedayat et al., 2014a, 2014b, 2018; El Fil et al., 2024; Han et al., 2024b). Hence, the peaks in transmitted wave amplitude are considered seismic precursors to the shear failure of the rock fracture.

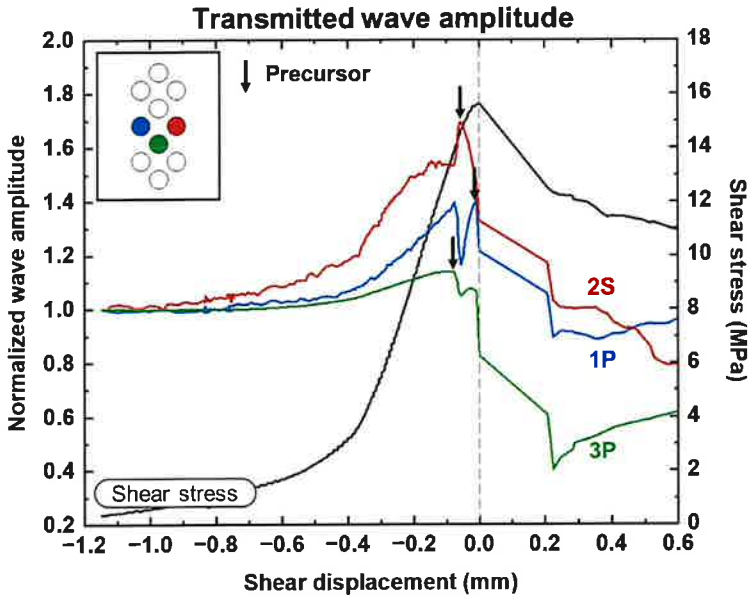

Figure 38. Transmitted wave amplitude through saturated granite fracture at 50oC.

Similar observations were found in the analysis of the converted modes (Figure 39). The intensity of the converted waves is associated with the cross-coupling fracture specific stiffness and the orientation of the voids/apertures between the fractures (Nakagawa et al., 2000). The cross-coupling stiffness is also related to the contact area between two fracture interfaces. Thus, the increase in converted wave amplitude before the peak shear stress is due to the increase in contact area induced by asperity interlocking (the arrows in the figure indicate the peaks of the converted amplitudes). After the peak, the subsequent amplitude reduction is attributed to the failure/damage of local contacts as the shear exceeds the shear strength of local rock asperities. Thus, the response of the converted wave is similar to that of the transmitted wave, and its peak can also be considered a seismic precursor to the shear failure of rock fractures (El Fil, 2021; Gheibi et al., 2021).

The behavior of the transmitted and converted wave amplitudes (Figure 38 & Figure 39) is similar to that of previous studies on dry and saturated fractures at room temperature (Han et al., 2024b). An increase in wave amplitude with shear is observed, followed by a peak (maximum) and subsequent decrease in wave amplitude with additional application of shear prior to the peak shear strength. An interesting finding is observed: the transmitted P-waves and converted waves display peaks in their amplitudes before shear failure, even though the rock fractures were water-saturated. Han et al. (2024b) showed that under saturated conditions, most P-waves and converted waves

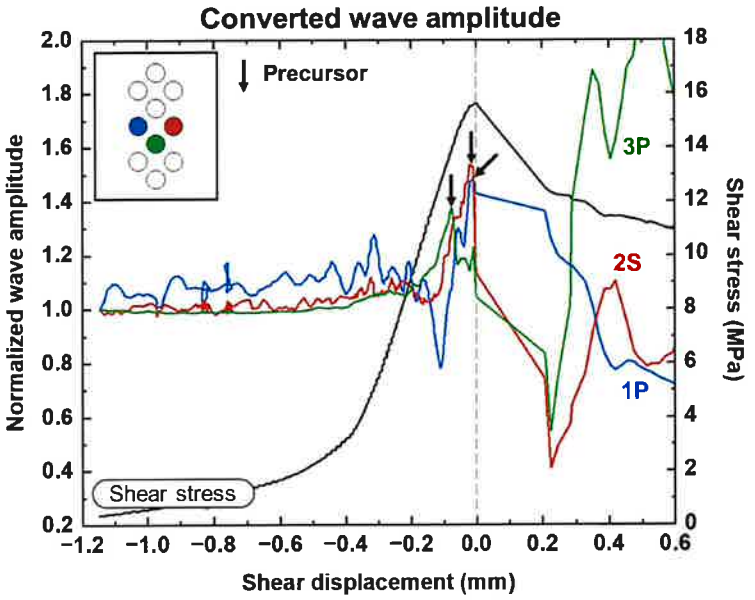

Figure 39. Converted wave amplitude through saturated granite fracture at 50oC.

exhibited either a monotonic reduction or a slight increase before a sudden rate reduction in amplitude. The authors explained that the highly incompressible fluid, water, between the saturated fractures could increase the fracture normal stiffness, and thus, enhance the normal stiffness, masking changes in normal fracture stiffness (P-wave amplitude) during shear. However, the increased magnitude of confinement most likely improved the contact between the surfaces for the temperature tests (2 MPa for the saturated rock joints versus 6 MPa for the saturated and heated rock joints).

4.1.1.2 Assessment of Fracture Aperture and Tortuosity through Electrical Impedance

Complex impedance measurements were conducted on idealized fractures. Fracture properties, such as aperture, tortuosity and porosity, were estimated using 3D X-ray microscopy. The equivalent channel model for electrical conduction in saturated rocks proposed by Walsh and Brace (1984) was used to estimate the electrical aperture and tortuosity for the smooth and tortuous fractures. A numerical model of electric conduction in saturated, idealized fractures, validated against experimental results, was also used to provide an understanding of the distribution of current density, particularly in the presence of tortuous flow paths and geometric constrictions.

Experimental Results: The geometric parameters of the fractures estimated with 3D X-ray microscopy include the nominal length between the voltage electrodes (L), the actual length and imaged (or geometric) tortuosity of the flow path (l and τ_{im}), the nominal fracture width (w), the mean imaged aperture (b_{im}), the cross-sectional area of the specimen (A), and the porosity (φ). Geometric tortuosity was determined by measuring the total length of the fracture wall path (in the flow direction) from representative 2D X-ray images of the fracture, covering the fracture length between the voltage electrodes.

Figure 40 shows the Bode plots of measured impedance for the two fracture geometries and for different concentrations of the NaCl solution. A Bode plot is a presentation form of complex impedance, where the impedance magnitude (on a logarithmic scale) and phase angle are plotted on a double y-axis plot, as a function of frequency (also on a logarithmic scale). The results for both fractures show a decreasing trend in the magnitude of impedance with decreasing fluid resistivity, which is expected due to the direct proportionality between impedance and fluid resistivity. Given that the fracture is made of polymer material, the only path for electrical conduction is through the electrolytic fluid within the fracture. For both the smooth and tortuous fracture, the impedance magnitude and phase angle show frequency dependence at high frequencies (10 kHz to 1 MHz). However, at low frequencies no obvious change in impedance with frequency is observed denoting the purely resistive behavior of the fluid-filled fracture. In this study, the focus was only on the impedance at the lowest frequency (10 mHz) that is representative of the fracture properties.

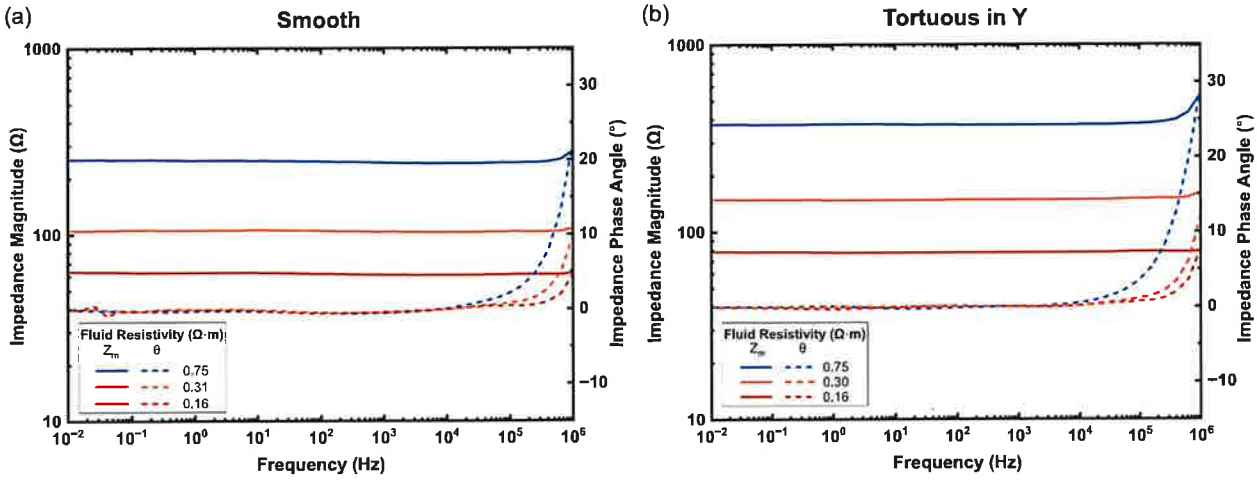

Figure 40. Bode plots of fluid-saturated fractures for various fluid resistivities: (a) smooth, and (b) tortuous in Y.

Based on the equivalent channel model ($F = \tau^2/\varphi$), considering a fracture porosity $\varphi = bw/A$, and specimen resistivity calculated from Eq. (4), the interpreted aperture from electrical impedance measurements is given by:

$$b_e = \tau^2 \frac{\rho_f}{Z} \frac{L}{w} \tag{7}$$

where $\tau = \tau_{im}$. For the tortuous fractures, the electrical aperture was also calculated using Eq. (x) but considering the indirect electrical tortuosity τ_e estimated using the modified Archie's power law between formation factor and porosity: $\tau = \tau_e = \sqrt{F\varphi}$, where φ is calculated using the volume ratio.

A comparison graph between the indirect electrical tortuosity estimated using the equivalent channel model and the geometric tortuosity estimated from X-ray images is shown in Figure 41. Geometric tortuosity was determined by measuring the total length of the fracture wall path (in the flow direction) from representative 2D X-ray images of the fracture, covering the fracture length between the voltage electrodes. As observed in Figure 41, the electrical tortuosity for the fracture

with tortuosity in X-axis and the centrally constricted channel was found to be up to 9-14% lower than the imaged tortuosity.

The aperture estimated using the equivalent channel model (or electrical aperture) is compared to the mean imaged aperture in Figure 42. For this graph, the electrical aperture of the tortuous fractures was estimated using the imaged tortuosity. The interpreted electrical apertures of the

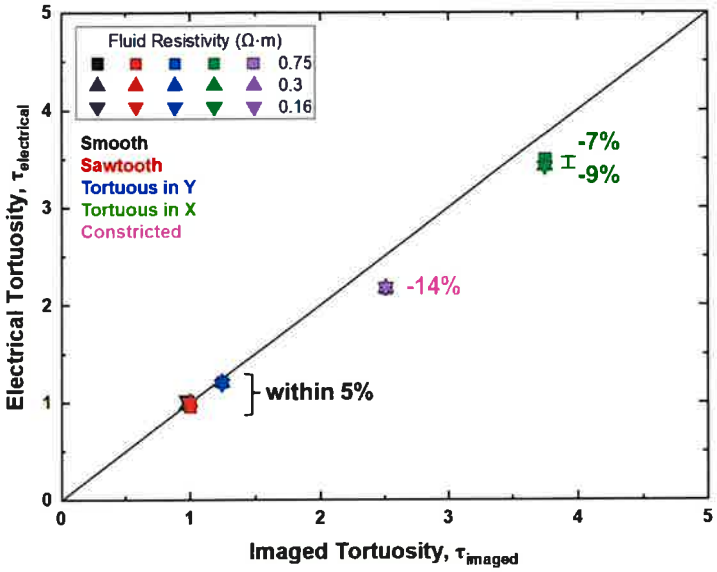

Figure 41. Electrical tortuosity compared to imaged tortuosity for five idealized fracture geometries.

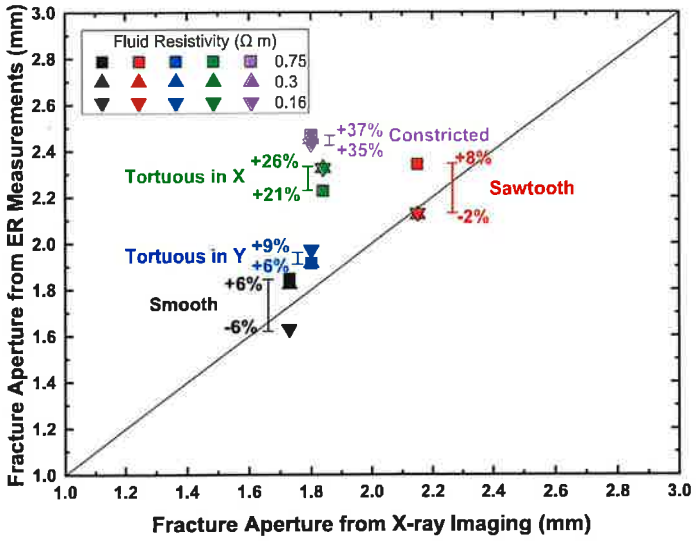

Figure 42. Electrical aperture estimated using imaged tortuosity compared to imaged aperture for five fracture geometries.

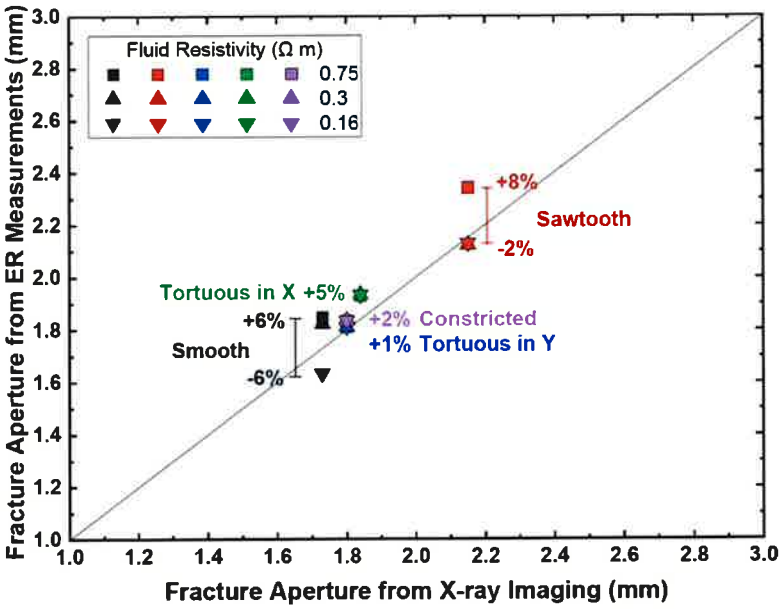

Figure 43. Electrical aperture estimated using electrical tortuosity compared to imaged aperture for five fracture geometries.

smooth and tortuous in Y fractures are shown to be within 10% of the imaged apertures when geometric tortuosity is used. However, for higher tortuosity (~3.8) and in the presence of constrictions, the electrical aperture was found to be 21% to 37% larger than the imaged aperture. The electrical aperture of the tortuous and constricted fractures was also estimated using the electrical tortuosity and the results are plotted in Figure 43. When electrical tortuosity was used in the estimation of aperture, the error was reduced to 5%.

Numerical Results; Figure 44a shows the resulting nodal potential field $V(x,y)$ (in volts, V) obtained from the solution of the governing equation for the fracture with tortuosity in the Y-axis. The current density $\vec{J}$ (in amperes per square meter, Am^{-2}) is then computed using Ohm's law:

$$\vec{J} = -\sigma\vec{\nabla}\mathrm{V}$$

where σ is the electrical conductivity (Sm^{-1}). The current density magnitude ($J(x,y) = |\vec{J}(x,y)|$), along with the corresponding electric field lines, is shown in Figure 44b. The results show that the current density is not uniformly distributed throughout the fracture aperture. Regions near the internal corners of the sawtooth walls exhibit locally intensified current density, while, away from the corners, along the nearly straight portions of the fracture, the current density magnitude is lower.

Similarly, Figure 45a&b depicts the simulated electric potential and current density field, respectively, in the constricted fracture. The results show that the current density is highly concentrated on and near the constricted channel. This behavior reflects the influence of geometric irregularities on the electric field distribution. As the current paths are forced to follow the tortuous geometry, they concentrate near sharp corners or constrictions and spread out in wider regions. The bending and convergence of current streamlines indicate an increase in the effective path

length for charge transport between the inlet and outlet boundaries. This deviation from a straight, uniform flow path represents electrical tortuosity, which quantifies how the fracture geometry elongates the effective current path relative to the direct length of the domain. For the tortuous and constricted fracture, it can also be seen that the current tends to follow a path that is shorter than that defined by the geometric tortuosity, consistent with the indirect electrical tortuosity estimated from the experimental measurements and the equivalent channel model.

To validate the numerical models of the idealized fractures, the numerical resistance was compared with the experimental resistance or impedance. The total current through the fracture was determined by integrating the component of J normal to a cross-section oriented perpendicular to the fracture walls. The total current I (A) was obtained by multiplying the line-integrated current density by the out-of-plane fracture width or aperture. The electrical resistance of the fracture was then evaluated using Ohm's law:

$$R = \frac{\Delta V}{I}$$

Figure 46 shows a comparison between the numerical and experimental resistances for four idealized fractured geometries. The measured resistances obtained from the four-electrode method were in good agreement (within 10%) with the numerical predictions, validating the modeling approach.

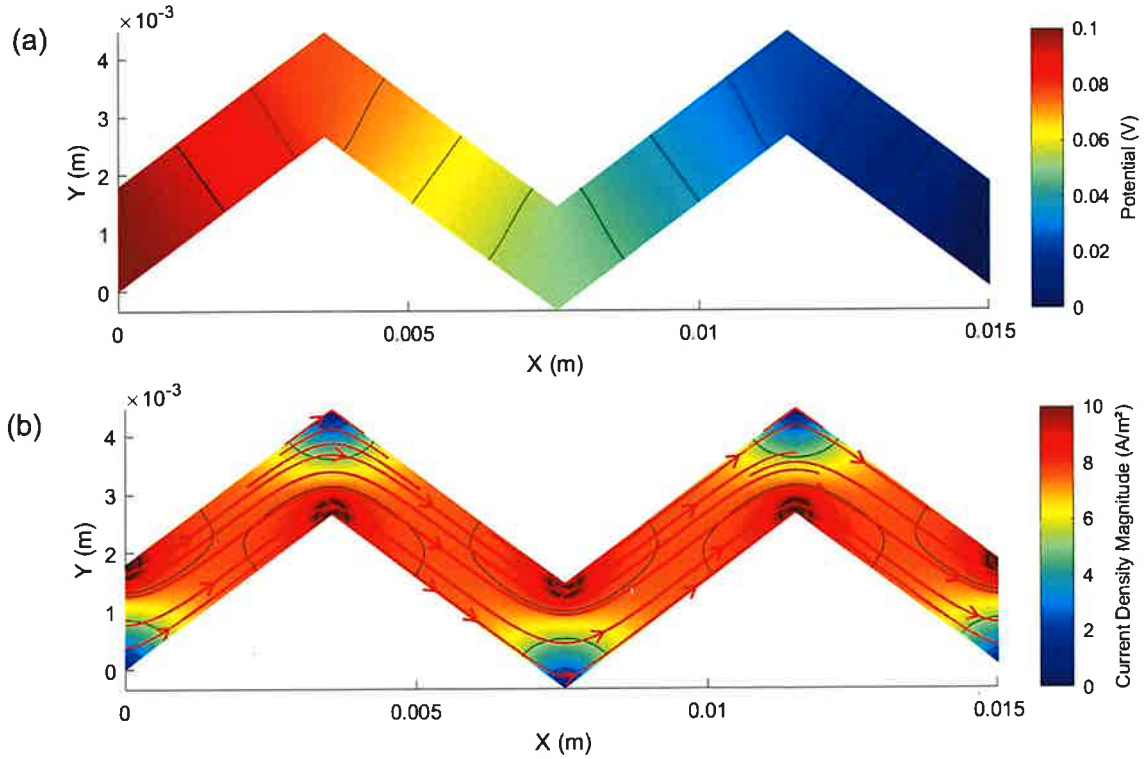

Figure 44. Simulated electric conduction in an idealized tortuous fracture: (a) Spatial distribution of electric potential; (b) Magnitude of the current density field and associated electric field lines.

fracture to its geometric characteristics, such as aperture, porosity, and tortuosity. The results of our study are consistent with the equivalent channel model, which introduces current path tortuosity in the relationship between the electrical response of saturated rocks and their pore geometry. The interpreted electrical apertures of the smooth and tortuous are shown to be within 10% of the imaged apertures when geometric tortuosity is used. However, for higher tortuosity (~3.8) and in the presence of constrictions, the electrical aperture was found to be 21% to 37% larger than the imaged aperture. When electrical tortuosity was used in the estimation of aperture, the error was reduced to 5%. This suggests that care must be taken in interpreting fracture aperture from electrical measurements. As shown by the work on rock with more complicated void geometry, the interpreted hydraulic and electrical aperture did not match by a factor 2 which if assuming the cubic law, would yield a difference of a factor of 8 in predicted flow rates. Accurate prediction of apertures would most likely require electrical resistivity tomography approach to probe different portions of the fractures, unlike these experiments that only probed a section of the fracture plane. However, both the hydraulic and electrical aperture showed the same overall trend with increasing stress (i.e., decreasing average aperture with increasing stress) as expected because both depend on the aperture of the fracture. This suggests, for application purposes at geothermal sites, monitoring the change in electrical resistivity is useful in monitoring the evolution of the fracture void geometry in response to changes in reservoir conditions (pressure, stress, geochemical interactions) that alter fracture flow paths. Finally, while the experiments showed no significant change in fluid conductivity, suggesting no significant geochemical reactions for Sierra White granite, studies at the Utah FORGE site show large changes in fluid chemistry over time. If these geochemical interactions significantly affect the fluid resistivity, this would also affect interpretation of fracture aperture if fluid resistivity is not monitored during electrical measurements.

Crack Initiation and Formation during Wellbore Breakout: Wellbore breakout experiments on Sierra White granite (SWG) samples using the Sandia Wellbore Experimental Simulation (SWESI) geometry in a conventional axisymmetric geomechanics load frame show the coupled hydrothermal effects on crack initiation and propagation around the simulated borehole. The addition of water (or any fluid tested) into the borehole region reduces the failure strength of SWG by 6%, and increasing temperature at 150 °C in wet boreholes further reduces the failure strength by 11%. Analysis of tested samples shows that microcrack density and the scale of microcrack extension increase with the addition of water and at high temperature, both in extent and density, compared to one at dry condition, indicating multiple minerals underwent higher deformations before failure. Localized, dense arrays of parallel transgranular (primarily along loading direction) and intragranular microfractures in quartz, less in feldspar, none/rare in biotite at breakout indicate mineral-specific deformation processes. Especially intragranular microfractures in quartz are more common directly adjacent to the main transgranular microfractures and are usually subparallel to the loading direction. Given the mineralogy of SWG tested, load-bearing minerals such as quartz and feldspar may be more subject to mineral dissolution once fractures are created, which can be used as an indicator of mineral dissolution at the production well. Another notable observation is that cracks initiated from the breakout zones rather than points along the main loading direction in all seven experiments, suggesting that damaged breakout zones triggered crack initiation and propagation as shown in computational validation. Although hydraulic fracturing is likely to induce fractures via tensile failures along the maximum stress direction at the field, our

experimental observation may indicate that failure mechanisms along the wellbore could be more complex, causing varying degree of permeability distributions that may impact the pressure response (e.g., shut-in pressure response).

Theoretical Analysis of Rate and State Friction: Using the extended Chen-Niemeijer-Spiers (CNS) model, we simulate steady-state friction and frictional stability parameter (*a-b*) for granite gouges, yielding results that align with experimental findings. As temperature increases, the extended CNS model effectively simulates the brittle-ductile transition (Figure 79a) and three regimes of velocity dependence of friction (Figure 79b). The temperature range of 150–350 °C favors seismic slip on granite gouges (Mei and Rudnicki, 2023). The extended CNS model incorporates the fluid injection rates, gouge, and bulk permeability. Notably, it favours slow slip compared to the standard rate-and-state friction (RSF) model. In Figure 80, the faster pressure rate can produce more frequent seismic events but tend to stabilize the fault slip finally. The extension of the microphysical CNS model to hydrothermal/geothermal conditions (Table 8) provides a theoretical basis for predicting potential fault behavior (creep, slow slip events, stick-slip events in Figure 81) as a function of temperature, gouge properties, grain friction and other parameters.

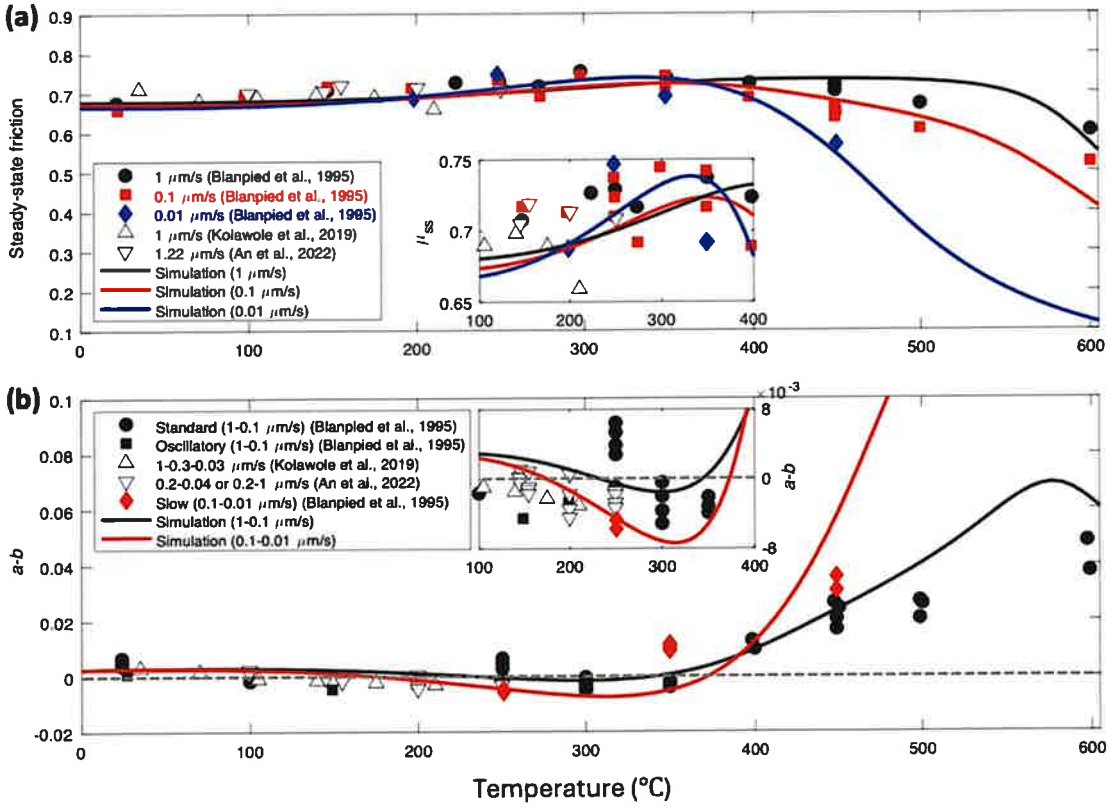

Figure 79. Comparisons between numerical and experimental results of (a) steady-state friction coefficient and (b) friction stability parameter (a − b) on granite fault gouges plotted against temperature. Copied from Mei et al. (2024).

Table 8. Microphysical Chen-Niemeijer-Spiers model is extended to hydrothermal conditions.

	Rate-and-state friction	Extended microphysical model
Constitutive equations	$\tau = (\sigma_n - p)\,[\mu_0 + a\ln(v/v_0) + b\ln(\theta v_0/d_c)]$ $\dot{\theta} = 1 - V\theta/d_c$ (aging law) $\dot{\theta} = -\frac{v\theta}{d_c}\ln\left(\frac{v\theta}{d_c}\right)$ (slip law)	$\tau = \frac{\tilde{\mu} + \tan\Psi}{1 - \tilde{\mu}\tan\Psi}(\sigma_n - p)$ $\tan\Psi = H(2\varphi_c - 2\varphi)^N$ $\tilde{\mu} = \tilde{\mu}^* + a_{\tilde{\mu}}(T)\ln[\dot{\gamma}_{gr}(T)/\dot{\gamma}^*_{gr}]$
Porosity	$\dot{\varphi} = -v/d_c[\varphi - \varphi_0 - \epsilon\ln(v/v_0)]$	$\dot{\varphi}/(1-\varphi) = (\tan\Psi)\dot{\gamma}_{gr}(T) - \dot{\varepsilon}pl(T,p)$
Fluid diffusion	$\dot{p} = -c^*(p - p_L) - \dot{\varphi}/\beta$	
Hydrothermal	Pore pressure p and temperature T	
Other factors	Bulk permeability: c^*; Far-field pressure p_L; Injection rate: $\dot{p}_\infty$; Gouge properties: a, b, d_c; Grain boundary friction $\tilde{\mu}$; Shear strain rate $\dot{\gamma}$; Normal strain rate $\dot{\varepsilon}$; Dilatacy angle Ψ; Frictional stability $(a-b) = \Delta\mu/\Delta\ln v$	

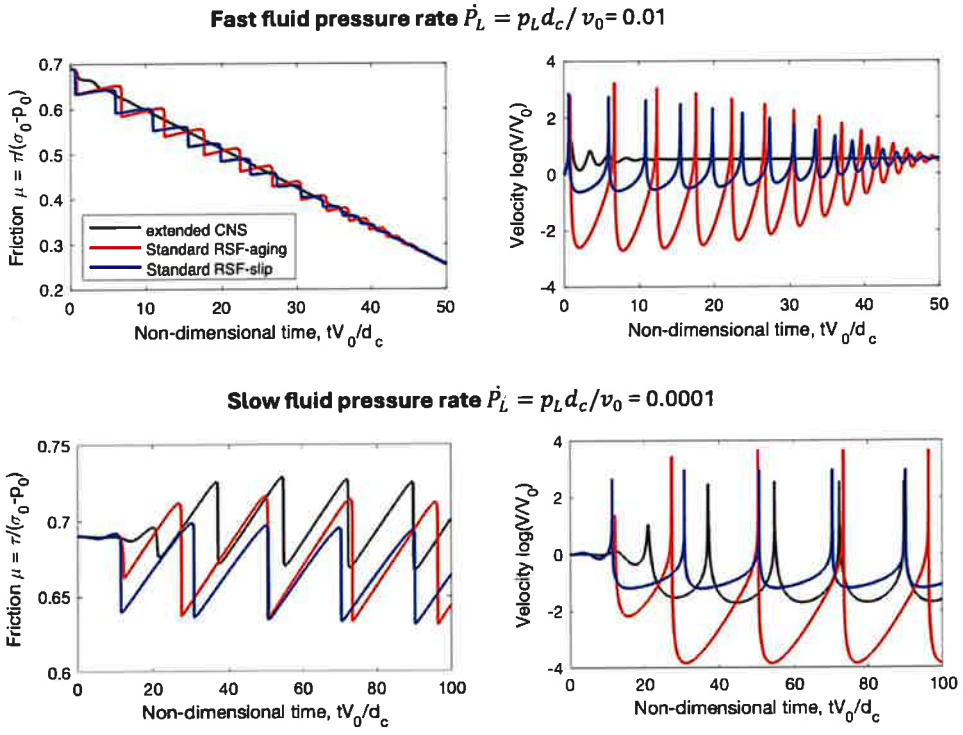

Figure 80. The simulated friction and non-dimensional slip velocity as a function of non-dimensional time for fast and slow fluid injection rates in three friction models. All numerical experiments are conducted at a fixed stiffness ratio of $k/k_c = 0.5$. Other parameters (e.g., permeability, specific storage) are within the experimental results on granite gouges. More detailed results are reported in Mei and Wang (2024).

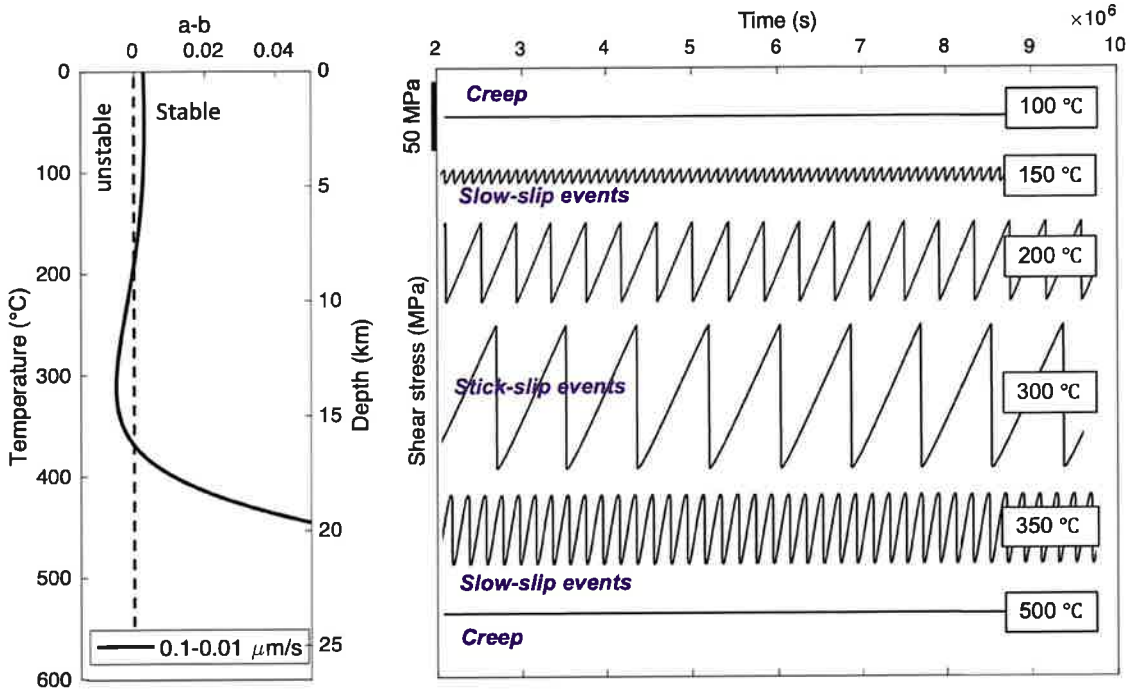

Figure 81. Using a spring-block fault analogue, our extended Chen-Niemeijer-Spiers model describes (a) the fault stability transition and (b) evolution of fault slip behaviors with depth (temperature), that is, from creep to stick-slip (earthquakes), then back to creep.

MOOSE-FARMS: We developed and validated a macroscopic model that can account for local deformation/frictional behavior, seismic/aseismic behavior, and determine the adequacy of classic Coulomb failure vs. rate-and-state friction. Through the integration of experimental data and mechanics-driven theory, a newly developed MOOSE-FARMS (FAult and Rupture Mechanics Simulations) simulator as a stand-alone module to MOOSE (e.g., Zhao and Elbanna, 2025) is now available to provide a tool for optimal reservoir design at the Utah FORGE site to enable the identification of key parameters for heat recovery and quantification of coupled THM(C) processes that govern fracture evolution. The proposed technology will provide a breakthrough to quantify both single fracture and reservoir scale states in coupled THMC processes and their evolutions in response to hydrothermally induced perturbations.

Joint Inversion: The computational framework and its estimation results for the circulation tests in 2024 at the Utah FORGE site demonstrate that the proposed inversion framework can identify probable fractured permeability field and predict geothermal reservoirs states such as temperature and pressure with good agreement with the measured data in the field. The computation efficiency of the developed framework has the potential for near real-time reservoir forecasts and operation design optimization.

4.3 Limitations/Lessons Learned

4.3.1 Direct Shearing

Direct shearing experiments along induced fractures in Sierra White Granite specimens were performed to determine the effect of temperature and fluid saturation on peak shear strength and friction angle, and to identify elastic wave signatures of fracture evolution during shearing. For conditions tested, the laboratory data showed that the shear behavior of saturated fractures compared to the dry condition did not significantly differ and was not significantly affected by temperatures up to 100°C The peak friction angle of Sierra White granite specimens in the dry conditions was 66.4° and only changed at most 2-3° with saturation and temperature which is not significant considering experimental error.

The ultrasonic data obtained during direct shear testing on induced fractures in granite contain signatures of precursors to slip (Han, 2024) for all tests conducted under the three conditions (i.e., dry, saturated, and temperature (room temperature, 50°C and 100°C). Identifiable precursors to slip, which consisted of a peak (maximum) in wave amplitude just prior to the peak shear strength, were consistently observed from analysis of the transmitted shear wave data sets. The increase in shear wave amplitude prior to failure is attributed to local contact surfaces that interlock and fail before macroscopic shear failure. While precursory signatures of failure/slip similar to the S-wave behavior were observed in the transmitted P-waves and converted waves (i.e. P-S & S-P) for dry conditions, saturation of the fracture water did not lead to no observable peak/maxima in amplitude prior to fail. Instead, these waves exhibited a continuous decrease in amplitude as shear stress increased. However, an abrupt change in the rate of reduction in the transmitted P-wave and converted amplitudes was observed that either coincided or occurred close to the peak shear strength. Thus, an onset of dramatic change in the reduction rate can be also taken as a seismic precursor to shear failure. The precursors to failure are understood through the displacement discontinuity theory for wave transmission across fractures (*Pyrak-Nolte et al.*, 1990; *Schoenberg*, 1980) which enables scaling of these laboratory observations made at frequencies of 200 kHz – 1MHz range to field frequencies of 10 Hz – 10s kHz. The measurable range of fracture specific stiffness that can be detected is obtained from the normalized frequency, ω_N, given by

$$\omega_N = \frac{\omega}{\omega_c} = \frac{\omega Z}{\kappa}$$

where ω is angular frequency, Z is the seismic impedance (i.e., density × phase velocity) and κ is fracture specific stiffness. When $0.1 < \omega_N < 10$, a fracture is detectable and at $\omega_N = 1$ reflection and transmission coefficient are equal (*Pyrak-Nolte*, 2019). As discussed by Nolte et al. (2025), a fracture with a normal fracture specific stiffness in the range of 1.2×10^{11} Pa/m $< \kappa < 1.3 \times 10^{13}$ Pa/m, and shear fracture specific stiffnesses 6.7×10^{10} Pa/m $< k < 6.8\ 10^{12}$ Pa/m would be detectable for a typical borehole field frequency of f = 10 kHz. Monitoring a fault/fracture with higher stiffnesses would not be possible at that frequency but changes in ensembles of high stiffness fractures would potentially be detectable.

4.3.2 Electrical Resistivity Measurements

Interpretation of fracture properties from electrical measurements (i.e., impedance measurements) rely heavily on theoretical models that link the electrical response of a fracture to its geometric characteristics, such as aperture, porosity, and tortuosity. From the laboratory measurements on idealized fracture geometry, a parallel plate model approximation works well for smooth fractures

but can underestimates fracture aperture by 30% for fractures with high tortuosity. An equivalent channel model introduces current path tortuosity in the relationship between the electrical response of saturated rocks and their pore geometry. When electrical tortuosity is used in the estimation of aperture, the interpreted aperture was found to be only within 1% of the imaged aperture. The test data from a fracture in Sierra White Granite found a mismatch between the interpreted hydraulic aperture from flow measurements and the aperture interpreted from electrical measurements. While both the hydraulic and electrical apertures showed the same trend with increasing stress, the magnitudes varied by a factor of 2. There are several possible explanations for these observations. For example, the electrical and hydraulic measurements are not sampling the same portions of the fractures. The electrical measurements sample the portion of the fracture between the electrodes while the hydraulic aperture is based on measurements made across the entire fracture plane. Another is that the theory cannot adequately account for complicated flow path geometry where connectivity of the voids dominates the behavior. Fluid flow in fractures can range from an effective medium regime where the fracture aperture or void volume dominates the flow behavior, to a percolation regime where the connectivity of the void space dominates. A parallel plate model may be sufficient for open or pumped open fractures but not fractures under stress. Additional experiments and theoretical research are needed to identify the source or sources of discrepancy between the interpreted hydraulic and electrical apertures observed for the induced fracture in Sierra White Granite to aid development of interpretation methods for field measurements.

4.3.3 Crack Initiation and Formation during Wellbore Breakout

Experimental results clearly show thermal-pore pressure effects on weakening mechanical strengths and microfracturing variations at wet and high temperatures compared to dry and room temperature condition using post sample image analysis and acoustic emission characteristics. Microfracturing around and from the borehole is also mineral-specific at microscale. However, all experimental works have been performed at static temperature conditions. Hence, these results did not capture thermal gradient effects during hydraulic fracturing with colder water than reservoir temperature. Another limit is the effect of loading rates on rock strength and characteristics of fracture initiation and propagation. Over the past 1-2 years, the effects of thermal gradient and cyclic thermal shock on mechanical behavior and acoustic emission characteristics for EGS have been more investigated in the literature. This topic needs to be further investigated at in-situ EGS conditions to facilitate the application of laboratory results to real EGS conditions.

4.3.4 Theoretical Analysis of Rate and State Friction

The modified Chen-Niemeijer-Spiers (CNS) model in this work is derived from the microphysical CNS model in the frictional regime and provides a direct link between the original CNS model and the standard rate-and-sate friction (RSF) model. Compared to the standard RSF, the modified CNS model was able to explain the frictional stability transition with varying slip velocities. Numerical simulations based on the modified CNS model show a more gradual transition for slow-slip events with a wider range of stiffness ratios, which are roughly consistent with experimental and natural observations. However, different micro-mechanisms in the gouge layer may influence velocity dependence of friction (a - b) and, therefore, modulate slow slip events. For example, a large a value can increase the velocity-strengthening of friction at high velocity (Mei and Wang, 2024), resulting in more slow slip events. The a value may vary under different hydrothermal and stress conditions due to its normal stress and temperature dependence. Hence, actual micro-mechanical processes at the Utah FORGE site need to be evaluated with proper parameterization

in our modified CNS model, which can be determined using a series of velocity-stepping experiments at in-situ conditions.

4.3.5 Simulation of Fracture/Fault Propagation

Our recent 3D computational model that includes continuum damage-breakage (CDB) model is implemented in the INL Multiphysics simulator, MOOSE as MOOSE-FARMS (FAult and Rupture Mechanics Simulations) as a stand-alone module to MOOSE. Our recent work was to validate updated dynamic rupture of fracture network with fluid injection through coupled hydro-mechanics. Our focus was on the parameter calibration process based on other experimental data (e.g., true-triaxial tests, uniaxial compression test) on the same SWG samples and current wellbore breakout tests. Preliminary results show good agreement with experimental data for dry samples and reasonably good agreement for fluid-saturated samples. Future work will focus on comparing breakout shape dimensions, performing quantitative comparisons with acoustic emission data, and investigating the impact of material heterogeneity on simulation outcomes. This validated simulator can be further developed and evaluated to account for more realistic fracturing processes at EGS conditions including Utah FORGE.

4.3.6 Joint Inversion

While the developed data assimilation method provided a reasonable estimation of the FORGE site permeability fields, there are limits with our effective permeability fields to represent discrete fracture networks (DFNs). To improve more realistic DFN estimation, forward simulation of thermo-hydraulic (TH) model needs to be performed with DFNs rather than only effective permeability fields. Although the developed data assimilation framework can be used for typical EGS conditions including Utah FORGE without modification, TH simulation results will contain more contrast pressure and temperature fields with preferential paths along the fractures. This will require the model accuracy of different deep learning models to capture high contrast pressure propagation through DFNs. Especially we noticed that shut-in pressure response and pressure increases at an early circulation stage would be influenced by permeability fields near injection locations, suggesting that reservoir models with DFNs would represent these pressure changes more accurately. Another restriction in forward modeling is the thermo-hydraulic (TH) model instead of thermo-hydro-mechanic (THM) model has been used. Although it could be practical to ignore the effect of mechanical processes on permeability changes associated with induced fracture systems over short time periods for circulation tests in 2024 at the Utah FORGE site, optimal operation needs to account for THM processes at an EGS lifetime. Related to DFNs for deep learning model training, natural fracture networks are generated stochastically, but induced DFNs were represented by single conceptual model. Although induced DFNs are needed to be constructed from other observations such as fiber optic sensing-based interpretation or geophone sensing analysis, it will be more general approach to generate induced DFNs stochastically conditioned on site specific conceptual models. It is noted again that the developed data assimilation framework and DFN generation method can account for this without any restriction. Due to time constraints, only 500 DFNs were used for training the generative model, which may not be sufficient for data-driven deep learning methods that usually require a large amount of training data. More DFNs for both natural and induced fractures need to be generated in the future, and more variations of fractures should be considered following future FORGE DFN models.

Conclusions and Recommendations

5.1 Summary of Conclusions

The key outcomes from this research are as follows:

Experimental Tasks

*X-ray imaging and electrical measurements on synthetic fractures were used to explore the robustness of the equivalent channel (Walsh and Brace, 1984) to estimate fracture aperture. While the parallel plate model approximation works well for uniform aperture fracture, it overestimates the aperture by 30% for fractures tortuosity. However, the error decreases to 1% when the electrical tortuosity rather than geometric tortuosity is used in the formulation.

* The design and initial testing of experimental approach were completed for concurrent measurements of fracture geometry, electrical resistivity, and ultrasonic waves in-situ in an X-ray microscope. Electrical resistivity measurements and X-ray imaging were performed on synthetic samples with different fracture void geometries to verify theories for interpreting fracture aperture from electrical measurements. The approach uses four Silver/Silver Chloride (Ag/AgCl) electrodes attached to a specimen saturated with a sodium chloride solution of specific ionic concentration to measure the complex impedance (Solartron 1260A impedance analyzer from 10-2 to 106 Hz). A numerical code for simulating electrical current density in fractures with variable void shape and aperture was developed to aid interpretation of electrical resistivity measurements on synthetic samples and fractured rock. For an induced fracture in granite, the hydraulic and electrical apertures showed the same trend with increasing stress, however, the magnitudes varied by a factor of 2. A parallel plate model may be sufficient for open or pumped open fractures but not for fractures under stress where connectivity of the voids dominates.

* A new direct shear testing apparatus, capable of withstanding an internal pressure of 10 MPa, was designed and fabricated to explore the shear behavior of unjacketed rock fractures under dry and saturated conditions. This new testing apparatus was equipped with a B-value testing setup to determine the back pressure required to achieve rock saturation through B-value tests. The minimum back pressure for saturation was 5.0 MPa for Sierra White granite. The repeatability and reliability of the new system were confirmed through a series of direct shear tests. Once the saturation tests were done, this testing apparatus was modified to accommodate water-immersion heaters and thermocouple probes to enable control of the internal temperature of the chamber (up to 120°C). Experiments on Sierra White granite found that the shear behavior of saturated fractures was not significantly affected by temperatures up to 100°C, which means that the strength changes were within the experimental error.

*The utilization of active seismic monitoring (i.e., P- and S-waves) enables the identification of precursors to shear failure for both dry and saturated fracture conditions. However, the precursory signatures observed in P-waves and converted modes (P-S & S-P) differ for these two conditions while the signatures in S-wave data is the same. S-waves are often insensitive to change in fluid saturation in a fracture (e.g., going from air to water) and they sample changes in the shear stiffness of the fracture that arises from asperity interlocking and failure as shearing progresses. Thus, the observed maxima in shear wave amplitude prior to slip occurs for both the saturated and dry conditions. However, P-waves are sensitive to changes in the

fluid compressibility in void spaces (i.e., air versus water) and probe the normal stiffness of the fracture. Water is less compressible than air which tends to mask changes in normal fracture specific stiffness. Most transmitted P-waves and converted waves did not exhibit peaks in wave amplitude with increasing shear displacement, but a noticeable drop in the rate of their amplitude decay was observed prior to the shear failure of saturated fractures. It has been demonstrated that such a rate reduction occurred near the peak in S-wave amplitude. As a result, a sudden change in the rate of P-wave and converted wave amplitudes can also be considered a seismic precursor to the shear failure of saturated rock fractures. Seismic precursors to shear failure/slip have the potential for early identification of failures, such as rock slope failures and earthquakes.

*In the experimental task on single wellbore breakout test on fracture initiation and propagation, we performed six complete fracturing experiments at high pressure (17.2 MPa effective stress) under three temperature conditions (room, 100 & 150 °C) and with either DI water, mineral oil or salt solution to evaluate the effect of fluid type and temperature on fracture patterns and near wellbore damage characteristics during borehole breakout with acoustic emission monitoring during testing and microCT imaging and thin section imaging of post-testing samples. We found that (1) wet conditions regardless of fluid type created much more complex micro-fracture patterns in damaged zones near the wellbore compared to the dry condition and lowered failure strength, (2) high temperature conditions (100 & 150 °C) in wet solutions tend to create more wellbore damage, complex micro fracture patterns through multiple minerals, and longer fracture propagation and lowered wellbore break failure strengths further. Although hydraulic fracturing is likely to induce fractures via tensile failures along the maximum stress direction at the field, our experimental observation may indicate that failure mechanisms along the wellbore could be more complex, causing varying degree of permeability distributions around wellbore that may impact the pressure response (e.g., shut-in pressure response and pressure increasing rate during initial injection). These experiments provide validation experimental data for the effect of fluid and temperature on damage mechanics and fracture patterns near a wellbore system in computational task.

Theoretical Tasks

*We extended the microphysically based CNS model by incorporating grain-boundary sliding coupled with thermally activated diffusion creep to describe the frictional behavior of granular fault gouges under hydrothermal conditions. Using a spring-slider system, the model quantitatively reproduces the evolution of steady-state friction and the friction rate parameter (a-b). The results show that steady-state friction increases moderately from low to intermediate temperatures but decreases sharply at high temperatures. Moreover, the extended model captures three regimes of velocity dependence, that is, velocity-strengthening at low temperatures (~0–160°C), velocity-weakening at intermediate temperatures (~160–370°C), and velocity-strengthening again at high temperatures (>370°C), in agreement with experimental data in the literature. Further analysis of the extended microphysical CNS model shows that slow slip is favored, compared to aging, and slip laws. Fast pressure rate may produce frequent seismic event but tend to stabilize the fault slip finally. In addition, the high (low) permeability can cause the fully (poorly) drained condition, resulting in small (large) shear dilatancy effect, to promote (inhibit) the fault slip.

Computational Tasks

*In the computational task, we developed a new stand-alone module in INL Multiphysics Simulator MOOSE framework as MOOSE-FARMS (FAult and Rupture Mechanics Simulations) that include constitutive equations for modeling dynamic frictional fracture 2D and 3D elastodynamics with a continuum damage-breakage (CDB) model. The theoretical finite deformation formulation for both dry (only mechanics) and hydro-thermal processes has been implemented into the MOOSE-FRAM. The code includes two of the most widely used friction laws including the slip-weakening friction law and the rate-and-state friction law to perform simulations with and without pore pressure that account for dynamic poro-elastic effects on damage evolution representing fracture initiation, propagation, and coalescence. The code of 2D and 3D CDB model has been quantitatively verified with borehole breakout problems from existing experimental data in the literature and new wellbore breakout experimental testing data with Sierra White granites (SWGs) from experimental task that included the dry, pore pressure effects, and thermal effects. Model validation with the wellbore experimental data has been performed with model parameterization with true-triaxial experimental results and other experimental data for Sierra White granite in the literature to apply the CDB model for laboratory wellbore breakout testing. Model validation cases match the experimental observation of failure strength and wellbore damage patterns relatively well to confirm the effect of fluid and temperature observed from the experimental task.

Joint Inversion Tasks

*We developed a deep generative model-based data assimilation framework that includes a reduced order (i.e., surrogate) model for fast prediction of the reservoir state (i.e., pressure and temperature) and DFN generator using deep learning diffusion models. The ML joint inversion method was applied to the Utah FORGE site characterization using the short-term and long-term recirculation testing performed in 2024 at the Utah FORGE site. The fractured EGSs are highly heterogeneous, which cannot be handled by traditional data assimilation methods that commonly result in smoothly changing spatial field estimation. In this work, we used an AI-driven generative method, denoising diffusion implicit model (DDIM), to create discrete fracture networks. DDIM learned to represent the non-Gaussian fractured fields with latent variables that follow the Gaussian distribution, and then the trained model can generate new fractured fields by projecting Gaussian latent samples into fractured fields. For data assimilation, ensemble smoother-multiple data assimilation (ES-MDA) framework was then applied to update latent space variables using pressure data at injection and production wells. First, the 9-hour circulation test conducted in April 2024 was used as calibration dataset for permeability fields, and then the calibrated model has been used as input to an open-source reservoir simulation (MRST) to validate AI-based data assimilation (i.e., history matching) approach against a long-term circulation data observed from August/September testing. The simulated temperature response was in good agreement with the measured temperature, showing the accuracy and computation efficiency for the proposed data assimilation framework.

Finally, this project led to the development and validation of 3 open-source tools that are available to the geothermal community:

(1) **MOOSE-FARM** – to simulate dynamic frictional fracture (2D & 3D) elastodynamics with a rate-and-state friction model and a 3D visco-poro-plastic, finite deformation, nonlocal continuum damage-breakage;

(2) **Theory** - that includes temperature, bulk permeability, injection fluid rate, and gouge properties such as friction parameters to improve insight into stable versus unstable sliding;

(3) **AI Data Assimilation** – for fast model prediction of the reservoir state. These tools provide a breakthrough to quantify both single fracture and reservoir scale states in coupled THMC processes and their evolutions in response to hydro-thermally induced perturbations.

5.2 Recommendations for Future Work

1) Laboratory testing on shear testing, electrical resistivity in fractured aperture, and fracture initiation and propagation from single wellbore remains challenging to perform at high temperature and wet conditions (>150 °C) with in-situ sensing (e.g., transducers for passive and active acoustic emission, coupling of transducers on samples, microCT imaging). Experimental protocols for coupled thermo-hydro-mechanical-chemical processes in EGS rock samples at high temperatures need to be more established with in-situ sensing capability.

2) Laboratory data remain limited, and additional measurements on the temperature dependence of Utah FORGE reservoir rocks including temperature shock and cyclic thermal loading are essential for a more reliable assessment of their induced seismicity potential and longevity of stimulated conditions.

3) Design a field experiment to test geophysical monitoring of fractures undergoing shear to demonstrate scalability of laboratory observed precursory signatures of slip.

4) The rock permeability, gouge grain size, and injection rates in Utah FORGE reservoir can largely affect the fault stability, which requires more field tests and continuous monitoring.

5) The current version of the MOOSE-FARMS (Fault and Rupture Mechanics Simulations) simulator includes a standard rate-and-state friction model in coupled hydro-mechanical formulation. The extended rate-and-state friction model as a function of temperature developed in this project needs to be incorporated into the MOOSE-FARMS with coupled thermo-hydro-mechanical formulation to fully account for dynamic frictional fracturing at Utah FORGE site.

6) Future data assimilation using the developed deep learning generative model framework needs to be extended with either finer grid discretization with carefully assigned well-function or embedded discrete fracture model (EDFM) formulation to accurately represent reservoir fractured systems with well configurations. In EDFM, DFNs can be represented explicitly and with matrix grids constructed independently, the fracture and matrix grids can be coupled to each other via source/sink relations. A recent DFN model at the Utah FORGE site after stimulations in 2024 includes 131 individual fractures within an area of 1.8 km x 1.5 km x 1.1 km based on recent Formation Micro-Imager

(FMI) logs, microearthquake (MEQ) monitoring, and other data sources (Finnila, 2025). Hence, it is desired to evaluate this new DFN model with EDFM formula in our deep learning-based data assimilation framework to improve automatic DFN characterization at the Utah FORGE site and evaluate the long-term operations.

A. Uploaded GDR Datasets/Reports List

Choens, C., & Yoon, H. (2023). *Utah FORGE 5-2557: Triaxial Shear and Wellbore Breakout Tests Report and Data*. [Data set]. Geothermal Data Repository. Sandia National Laboratories. https://doi.org/10.15121/2208745

Han, K., Pyrak-Nolte, L., & Bobet, A. (2022). *Utah FORGE: Results of Direct Shear Tests on Saturated Joints in Sierra White Granite*. [Data set]. Geothermal Data Repository. Purdue University. https://doi.org/10.15121/1987550

Han, K., Pyrak-Nolte, L., & Bobet, A. (2025). *Utah FORGE: Results of Direct Shear Tests on Saturated Joints in Sierra White Granite at Elevated Temperatures*. [Data set]. Geothermal Data Repository. Purdue University. https://gdr.openei.org/submissions/1802

Yoon, H., & Choens, R. (2025). Utah FORGE 5-2557: Wellbore Breakout Tests Data. [Data set]. Geothermal Data Repository. Sandia National Laboratories. https://gdr.openei.org/submissions/1798

B. Journal Articles, Conference Papers & Abstracts

Abdelmeguid, M., Zhao, C., Yalcinkaya, E. *et al.* Dynamics of episodic supershear in the 2023 M7.8 Kahramanmaraş /Pazarcik earthquake, revealed by near-field records and computational modeling. *Commun Earth Environ* **4**, 456 (2023). https://doi.org/10.1038/s43247-023-01131-7

Bao, J., Lee, J., Yoon, H., and L. Pyrak-Nolte. Subsurface Characterization Using Bayesian Deep Generative Prior-Based Inverse Modeling for Utah FORGE Enhanced Geothermal System. Paper presented at the 57th U.S. Rock Mechanics/Geomechanics Symposium, Atlanta, Georgia, USA, June 25-28, 2023

Bao, Jichao, Lee, Jonghyun, and Hongkyu Yoon. Enhanced Geothermal Site Characterization Using Generative Adversarial Network and Ensemble Method. Paper presented at the 58th U.S. Rock Mechanics/Geomechanics Symposium, Golden, Colorado, USA, June 23-26, 2024

Choens, R.C., Wilson, J.E., and H. Yoon. Water enhanced borehole breakout formation in granite at elevated temperatures. Paper presented at the 59th U.S. Rock Mechanics/Geomechanics Symposium, Santa Fe, New Mexico, June 8-11, 2025

Christoforidou, E., Bobet, A., Pyrak-Nolte, L.J., (2024). *Monitoring Geochemical Alteration of Fracture Surfaces in Granite with Electrical Conductivity Measurements*, Proceedings of the 58th US Rock Mechanics/Geomechanics Symposium held in Golden, Colorado, USA, 23-26 June 2024, ARMA 24-0589

Christoforidou, E., Bobet, A. and L. J. Pyrak-Nolte, Interpreting fracture aperture with electrical resistivity measurements, 2024 Annual Fall Meeting of the American Geophysical Union, Dec 9-13, 2024, NS24A-06;

Christoforidou, E., Bobet, A., Pyrak-Nolte, L.J., (2025). *Assessment of Fracture Aperture and Tortuosity through Electrical Impedance*, Proceedings of the 59th US Rock Mechanics/Geomechanics Symposium held in Santa Fe, New Mexico, USA, 8-11 June 2025, ARMA 25-0532;

Han, K., Pyrak-Nolte, L. J. and Bobet, *Monitoring of Shear Failure along Rock Fractures in Limestone and Granite with Seismic Wave Transmission*, Proceedings of the 57th US Rock Mech./Geomech. Symp., Atlanta, Georgia, USA, 25-28 June 2023, ARMA 23-0290

Han, K., Pyrak-Nolte, L. J., Bobet, A., (2024). *Monitoring Slip along Saturated Fractures in Granite at Elevated Temperatures*, Proceedings of the 58th US Rock Mechanics/Geomechanics Symposium held in Golden, Colorado, USA, 23-26 June 2024, ARMA 24-0495.

Han, K., Pyrak-Nolte, L. J., & Bobet, A. (2024). Seismic Precursors to Shear Failure of Dry and Saturated Rock Fractures. *Rock Mechanics and Rock Engineering*, 1-20 (invited paper)

Han K, Pyrak-Nolte LJ, Bobet A. Direct Shear Testing Apparatus for Saturated Rock Joints. Geotechnical Testing Journal. 2024 Nov 1;47(6):1229-42

Mei, C. and Rudnicki, J.W., 2022, December. A Comparison between Classical, Power-Law Rate-and-State Friction, and CNS Models Based on Numerical Simulations of Seismic Cycles. In AGU Fall Meeting Abstracts (Vol. 2022, pp. MR25B-0077).

Mei, C., & Rudnicki, J. W. (2023). *Microphysical modeling of fault slip and stability transition in hydrothermal conditions*. Geophys. Res. Let., 50, e2023GL103730;

Mei, C., & Rudnicki, J. W. (2023). *Microphysical modelling of frictional slip in hydrothermal conditions*, Proceedings of the 57th US Rock Mechanics/Geomechanics Symposium held in Atlanta, Georgia, USA, 25-28 June 2023, ARMA 23-0352.

Mei, C., Mercuri, M. and Rudnicki, J.W., (2024). *Rock friction experiments and modeling under hydrothermal conditions*. Earth-Science Reviews, p.104824

Mei, C. and Rudnicki, J.W., 2023. *Temperature-Dependent Frictional Stability and Behaviors*. AGU Fall Meeting 2023, T23A-02, San Francisco, CA.

Mercuri, M. and Rudnicki, J.W., 2023, *Effect of Normal Stress Variation in Triaxial Compression on Determination of Rate-and State-Frictional Parameters and Slip Stability Due to Fluid Injection*. AGU Fall Meeting 2023, T31C-023, San Francisco, CA

Rudnicki, J. W., & Mei, C. (In revision, October 2025). Homogeneous and membrane pore fluid diffusion in spring block simulations of fault slip with rate and state friction. For the Journal of Geophysical Research: Solid Earth.

Yoon, H., Bao, J., and J. Lee, Machine Learning-based History Matching of Discrete Fracture Network Fields at the Utah FORGE Enhanced Geothermal System, Geothermal Rising Conference, Reno, Nevada, Oct. 26-29, 2025.

Zhao, C., Mia, M. S., Elbanna, A., & Ben-Zion, Y. (2024). Dynamic rupture modeling in a complex fault zone with distributed and localized damage. *Mechanics of Materials*, *198*, Article 105139. https://doi.org/10.1016/j.mechmat.2024.105139

Acknowledgments

Sandia National Laboratories is a multi-mission laboratory managed and operated by National Technology & Engineering Solutions of Sandia, LLC (NTESS), a wholly owned subsidiary of Honeywell International Inc., for the U.S. Department of Energy's National Nuclear Security Administration (DOE/NNSA) under contract DE-NA0003525. This written work is authored by

References

Bao, J., Lee, J., Yoon, H., & Pyrak-Nolte, L. (2023). Subsurface characterization using Bayesian deep generative prior-based inverse modeling for Utah FORGE enhanced Geothermal system. In ARMA US Rock Mechanics/Geomechanics Symposium.

Biot, M. A. (1941). General theory of three-dimensional consolidation. Journal of Applied Physics, 12(2), 155-164.

Biot, M. A. (1956). Theory of deformation of a porous viscoelastic anisotropic solid. Journal of Applied Physics, 27(5), 459-467.

Butt, A., Hedayat, A., Tudisco, E., & Roshan, H. (2020, June). Evaluation of progressive damage in barre granite using ultrasonic velocity tomography and digital image correlation. In ARMA US Rock Mechanics/Geomechanics Symposium.

Chen, M., Mei, S., Fan, J., & Wang, M. (2024). Opportunities and challenges of diffusion models for generative AI. National Science Review, 11(12), nwae348.

Choens, R. C., Ingraham, M. D., Lee, M. Y., Yoon, H., and T. A. Dewers. (2018). Acoustic Emission During Borehole Breakout. Paper presented at the 52nd U.S. Rock Mechanics/Geomechanics Symposium, Seattle, Washington, ARMA-2018-619, June 2018.

Choens, R.C., Wilson, J.E., and H. Yoon. (2025). Water enhanced borehole breakout formation in granite at elevated temperatures. Paper presented at the 59th U.S. Rock Mechanics/Geomechanics Symposium, Santa Fe, New Mexico, June 2025. doi: https://doi.org/10.56952/ARMA-2025-0603.

Chiu, H. K., Johnston, I. W., & Donald, I. B. (1983). Appropriate techniques for triaxial testing of saturated soft rock. In International Journal of Rock Mechanics and Mining Sciences & Geomechanics Abstracts (Vol. 20, No. 3, pp. 107-120). Pergamon.

Cook, N. G. (1992, May). Natural joints in rock: mechanical, hydraulic and seismic behaviour and properties under normal stress. In International Journal of Rock Mechanics and Mining Sciences & Geomechanics Abstracts (Vol. 29, No. 3, pp. 198-223). Pergamon.

El Fil, H. (2021). Shear Response of Rock Discontinuities: through the Lens of Geophysics (Doctoral dissertation, Purdue University).

El Fil, H., Pyrak-Nolte, L. J., & Bobet, A. (2024). The Role of a Rock Discontinuity's Micro-structure and Aperture on the Detection of Seismic Precursors to Shear Failure. Rock Mechanics and Rock Engineering, 57(4), 2469-2482.

Emerick, A. A., & Reynolds, A. C. (2013). Ensemble smoother with multiple data assimilation. Computers & Geosciences, 55, 3-15.

Favero, V., Ferrari, A., & Laloui, L. (2018). Anisotropic behaviour of opalinus clay through consolidated and drained triaxial testing in saturated conditions. Rock Mechanics and Rock Engineering, 51, 1305-1319.

Finnila, A. (2025). Utah FORGE: Updated Discrete Fracture Network Model - 2025. [Data set]. Geothermal Data Repository. WSP Golder. https://gdr.openei.org/submissions/1750.

Finnila, A., & Jones, C. (2024). Updated reference discrete fracture network model at Utah FORGE. In Proceedings, 49th Workshop on Geothermal Reservoir Engineering, Stanford University, Stanford, CA.

Garg, P., Hedayat, A., & Griffiths, D. V. (2020). Numerical simulation of fracture initiation in Barre Granite using an experimentally validated XFEM model. In ARMA US Rock Mechanics/Geomechanics Symposium. Paper number ARMA-2020.

Goodfellow, I., Pouget-Abadie, J., Mirza, M., Xu, B., Warde-Farley, D., Ozair, S., Courville, A., Bengio, Y. (2014). Generative Adversarial Nets. Advances in neural information processing Systems, pp. 2672–2680.

Griffiths, L., Heap, M. J., Baud, P., & Schmittbuhl, J. (2017). Quantification of microcrack characteristics and implications for stiffness and strength of granite. International Journal of Rock Mechanics and Mining Sciences, 100, 138-150.

Han, K. (2024). Monitoring of Saturated Rock Discontinuities Under Elevated Temperatures and Water Pressures (Doctoral dissertation, Purdue University).

Han, K., Pyrak-Nolte, L. J., & Bobet, A. (2021). Experimental Investigation of Rock Saturation Determination. In ARMA US Rock Mechanics/Geomechanics Symposium.

Han, K., Pyrak-Nolte, L. J., & Bobet, A. (2024a). Direct Shear Testing Apparatus for Saturated Rock Joints. Geotechnical Testing Journal, 47(6), 1229-1242.

Han, K., Pyrak-Nolte, L. J., & Bobet, A. (2024b). Seismic Precursors to Shear Failure of Dry and Saturated Rock Fractures. Rock Mechanics and Rock Engineering, 1-20.

Heap, M. J., & Faulkner, D. R. (2008). Quantifying the evolution of static elastic properties as crystalline rock approaches failure. International Journal of Rock Mechanics and Mining Sciences, 45(4), 564-573.

Hedayat, A., Pyrak-Nolte, L. J., & Bobet, A. (2014). Precursors to the shear failure of rock discontinuities. Geophysical Research Letters, 41(15), 5467-5475.

Hedayat, A., Pyrak-Nolte, L. J., & Bobet, A. (2014a). Multi-modal monitoring of slip along frictional discontinuities. Rock Mechanics and Rock Engineering, 47, 1575-1587.

Hedayat, A., Haeri, H., Hinton, J., Masoumi, H., & Spagnoli, G. (2018). Geophysical signatures of shear-induced damage and frictional processes on rock joints. Journal of Geophysical Research: Solid Earth, 123(2), 1143-1160.

Hu, L., A. Ghassemi, J. Pritchett, and S. Garg. (2020). Characterization of laboratory-scale hydraulic fracturing for EGS. Geothermics, 83, 101706.

Hyman, J. D., Karra, S., Makedonska, N., Gable, C. W., Painter, S. L., & Viswanathan, H. S. (2015). dfnWorks: A discrete fracture network framework for modeling subsurface flow and transport. Computers & Geosciences, 84, 10-19.

Ingraham, M. D., T. A. Dewers, M. Williams, C. S. N. Cheung, and B. C. Haimson. (2017). Bifurcation Theory Applied to Granite Under General States of Stress. In Proceedings of 51st US Rock Mechanics/Geomechanics Symposium, June 25-28, 2017, San Francisco, CA, USA: American Rock Mechanics Association.

Jaeger, J. C., Cook, N. G. W., & Zimmerman, R. W. (2007). Fundamentals of Rock Mechanics. John Wiley & Sons.

Ji, Y., Wang, L., Hofmann, H., Kwiatek, G., & Dresen, G. (2022). High-rate fluid injection reduces the nucleation length of laboratory earthquakes on critically stressed faults in granite. Geophysical Research Letters, 49(23), e2022GL100418.

Kahraman, S. (2002). Correlation of TBM and drilling machine performances with rock brittleness. Engineering Geology, 65(4), 269-283.

Katsman, R., and Z. Ben-Avraham. (2025). Modeling reservoir-induced seismicity: A dynamic poro-visco-elasto-plastic earthquake simulator with spontaneous dilatant coseismic rupture. Earth and Space Science 12.2.

Kim, S. E., Yoon, H., & Lee, J. (2021). Fast and scalable earth texture synthesis using spatially assembled generative adversarial neural networks. Journal of Contaminant Hydrology, 243, 103867.

Labuz, J. F., Shah, S. P., & Dowding, C. H. (1985). Experimental analysis of crack propagation in granite. In International Journal of Rock Mechanics and Mining Sciences & Geomechanics Abstracts (Vol. 22, No. 2, pp. 85-98). Pergamon.

Labuz, J. F., Shah, S. P., & Dowding, C. H. (1987). The fracture process zone in granite: evidence and effect. In International Journal of Rock Mechanics and Mining Sciences & Geomechanics Abstracts (Vol. 24, No. 4, pp. 235-246). Pergamon.

Li, B. Q., & Einstein, H. H. (2019). Direct and microseismic observations of hydraulic fracturing in barre granite and opalinus clayshale. Journal of Geophysical Research: Solid Earth, 124(11), 11900–11916.

Lie, K. A., & Møyner, O. (Eds.). (2021). Advanced modelling with the MATLAB reservoir simulation toolbox. Cambridge University Press.

Liu, R., Podgorney, R., Finnila, A., Xing, P., McLennan, J., & Moore, J. (2022). Development of a Coupled Multi-Field Utah FORGE Native State Model: Phase 3 Update. In 2022 Geothermal Rising Conference: Using the Earth to Save the Earth, GRC 2022 (pp. 589-596). Geothermal Resources Council.

Lokajíček, T., R. Vasin, T. Svitek, M. Petružálek, M. Kotrlý, I. Turková, R. Onysko, and H. R. Wenk. (2021). Intrinsic elastic anisotropy of Westerly granite observed by ultrasound measurements, microstructural investigations, and neutron diffraction. Journal of Geophysical Research: Solid Earth 126, no. 1: e2020JB020878.

Lowe, J., & Johnson, T. C. (1960). Use of back pressure to increase degree of saturation of triaxial test specimens. In Proc., ASCE Research Conf. on Shear Strength of Cohesive Soils (pp. 819–836).

Lyakhovsky, V., Ben-Zion, Y. & Agnon, A. (1997). Distributed damage, faulting, and friction. Journal of Geophysical Research: Solid Earth 102, 27635–27649.

Lyakhovsky, V., W. Zhu, and E. Shalev (2015), Visco-poroelastic damage model for brittle-ductile failure of porous rocks, J. Geophys. Res. Solid Earth, 120, 2179–2199, doi:10.1002/2014JB011805.

Lyakhovsky, V., Ben-Zion, Y., Ilchev, A. & Mendecki, A. (2016). Dynamic rupture in a damage-breakage rheology model. Geophysical Journal International 206, 1126–1143.

Makhnenko, R. Y., & Labuz, J. F. (2013). Saturation of porous rock and measurement of the B coefficient. In ARMA US Rock Mechanics/Geomechanics Symposium (pp. ARMA-2013). ARMA.

McLaskey, G. C. (2019). Earthquake initiation from laboratory observations and implications for foreshocks. Journal of Geophysical Research: Solid Earth, 124(12), 12882–12904.

Mei, C., & Rudnicki, J. W. (2023a). Microphysical modeling of fault slip and stability transition in hydrothermal conditions. Geophysical Research Letters, 50 (13), e2023GL103730. https://doi.org/10.1029/2023GL103730.

Mei, C., & Rudnicki, J. W. (2023b). Microphysical modelling of frictional slip in hydrothermal conditions. ARMA US Rock Mechanics/Geomechanics Symposium, ARMA–2023. https://doi.org/10.56952/ARMA-2023-0352.
Mei, C., Mercuri, M., & Rudnicki, J. W. (2024). Rock friction experiments and modeling under hydrothermal conditions. Earth-Science Reviews, 104824. https://doi.org/10.1016/j.earscirev.2024.104824.
Mesri, G., Adachi, G., & Ullrich, C. R. (1976). Pore-pressure response in rock to undrained change in all-round stress. Géotechnique, 26(2), 317–330.
Morgan, S. P., Johnson, C. A., & Einstein, H. H. (2013). Cracking processes in Barre granite: fracture process zones and crack coalescence. International Journal of Fracture, 180(2), 177–204.
Mutlu, O., & Bobet, A. (2006). Slip propagation along frictional discontinuities. International Journal of Rock Mechanics and Mining Sciences, 43(6), 860–876.
Nakagawa, S., Nihei, K. T., & Myer, L. R. (2000). Shear-induced conversion of seismic waves across single fractures. International Journal of Rock Mechanics and Mining Sciences, 37(1–2), 203–218.
Nasseri, M. H. B., & Mohanty, B. (2008). Fracture toughness anisotropy in granitic rocks. International Journal of Rock Mechanics and Mining Sciences, 45(2), 167–193.
Nasseri, M. H. B., Schubnel, A., & Young, R. P. (2007). Coupled evolutions of fracture toughness and elastic wave velocities at high crack density in thermally treated Westerly granite. International Journal of Rock Mechanics and Mining Sciences, 44(4), 601–616.
Nasseri, M. H. B., Tatone, B. S. A., Grasselli, G., & Young, R. P. (2009). Fracture toughness and fracture roughness interrelationship in thermally treated Westerly granite. Pure and Applied Geophysics, 166(5), 801–822.
Nolte, D. D., Pyrak-Nolte, L. J., Beachy, J. and C. Ziegler. (2000). Transition from the displacement discontinuity limit to the resonant scattering regime for fracture interface waves, International Journal of Rock Mechanics Mining Science & Geomechanics Abstracts, vol 37, p219-230.
Nolte, D.D., Pyrak-Nolte, L. J. and C. Hopp. (2025). Monitoring Fracture Hydromechanical Evolution in the Lab and Field using Unsupervised Metric Learning, Journal of Geophysical Research – Machine Learning and Computation, vol 2, no. 3, September 2025, e2025JH000657, https://doi.org/10.1029/2025JH000657.
Ohnaka, M., & Shen, L. F. (1999). Scaling of the shear rupture process from nucleation to dynamic propagation: Implications of geometric irregularity of the rupturing surfaces. Journal of Geophysical Research: Solid Earth, 104(B1), 817–844.
Peng, S. S. (1976). A photoelastic coating technique for rock fracture analysis. In International Journal of Rock Mechanics and Mining Sciences & Geomechanics Abstracts (Vol. 13, No. 6, pp. 173–176). Pergamon.
Petružálek, M., Z. Jechumtálová, J. Šílený, P. Kolář, T. Svitek, T. Lokajíček, I. Turková, M. Kotrlý, and R. Onysko. (2020). Application of the shear-tensile source model to acoustic emissions in Westerly granite. International Journal of Rock Mechanics and Mining Sciences 128, 104246.
Pourahmadian, F., & Guzina, B. B. (2018). On the elastic anatomy of heterogeneous fractures in rock. International Journal of Rock Mechanics and Mining Sciences, 106, 259–268.
Pyrak-Nolte, L. J., Myer, L. R., & Cook, N. G. (1990). Transmission of seismic waves across single natural fractures. Journal of Geophysical Research: Solid Earth, 95(B6), 8617–8638.

Pyrak-Nolte, L.J., (2019). Chapter 14: Fracture Specific Stiffness: the Critical Link between the Scaling Behavior of Hydro-Mechanical Coupling in Fractures and Seismic Monitoring, for "Science of Carbon Storage in Deep Saline Formations: Process Coupling Across Time and Spatial Scales", eds P. Newell and A. Ilgen, Elsevier.

Ronneberger, O., Fischer, P., & Brox, T. (2015). U-net: Convolutional networks for biomedical image segmentation. In International Conference on Medical image computing and computer-assisted intervention (pp. 234-241). Cham: Springer international publishing.

Rudnicki, J. W. (1986). Fluid mass sources and point forces in linear elastic diffusive solids. Mechanics of materials, 5(4), 383-393.

Rutter, E. H., & Neumann, D. H. K. (1995). Experimental deformation of partially molten Westerly granite under fluid-absent conditions, with implications for the extraction of granitic magmas. Journal of Geophysical Research: Solid Earth, 100(B8), 15697–15715.

Sawayama, K. (2021). Study on the Relationships between Fracture Flow Behaviors and Geophysical Properties for the Quantitative Monitoring of Fractured Reservoirs. PhD dissertation, Kyushu University.

Schoenberg, M. (1980). Elastic wave behavior across linear slip interfaces. The Journal of the Acoustical Society of America, 68(5), 1516–1521.

Scott, J. H., LaDelfe, C. M., & Mathews, M. A. (1985). Test pits for calibrating well logging equipment in fractured hard-rock environment. In SPWLA Annual Logging Symposium (pp. SPWLA-1985). SPWLA.

Simmons, S., Kirby, S., Allis, R., Moore, J., & Fischer, T. (2018). Update on production chemistry of the Roosevelt Hot Springs reservoir. Stuart F Simmons/University of Utah.

Song, J., Meng, C., & Ermon, S. (2020). Denoising diffusion implicit models. arXiv preprint arXiv:2010.02502.

Sprunt, E. S., & Brace, W. F. (1974). Direct observation of microcavities in crystalline rocks. In International Journal of Rock Mechanics and Mining Sciences & Geomechanics Abstracts (Vol. 11, No. 4, pp. 139–150). Pergamon.

Sweeney, M. R., Gable, C. W., Karra, S., Stauffer, P. H., Pawar, R. J., & Hyman, J. D. (2020). Upscaled discrete fracture matrix model (UDFM): an octree-refined continuum representation of fractured porous media. Computational Geosciences, 24(1), 293-310.

Tarokh, A., Makhnenko, R. Y., Fakhimi, A., & Labuz, J. F. (2017). Scaling of the fracture process zone in rock. International Journal of Fracture, 204(2), 191–204.

Walsh, J. B., & Brace, W. F. (1984). The effect of pressure on porosity and the transport properties of rock. Journal of Geophysical Research: Solid Earth, 89(B11), 9425-9431.

Ward, S. H., Parry, W. T., Nash, W. P., Sill, W. R., Cook, K. L., Smith, R. B., D. S. Chapman, F. H. Brown, J. A. Whelan, and Bowman, J. R. (1978). A summary of the geology, geochemistry, and geophysics of the Roosevelt Hot Springs thermal area, Utah. Geophysics, 43(7), 1515-1542.

Walton, N. R. G. (1989). Electrical conductivity and total dissolved solids—what is their precise relationship?. Desalination, 72(3), 275-292.

Wissa, A. E. (1969). Pore pressure measurement in saturated stiff soils. Journal of the Soil Mechanics and Foundations Division, 95(4), 1063–1073.

Xia, K., Nasseri, M. H. B., Mohanty, B., Lu, F., Chen, R., & Luo, S. N. (2008). Effects of microstructures on dynamic compression of Barre granite. International Journal of Rock Mechanics and Mining Sciences, 45(6), 879–887.

Xing, P., England, K., Moore, J., & McLennan, J. (2025). Analysis of the 2024 Circulation Tests at Utah FORGE and the Response of Fiber Optic Sensing Data. In 50th Workshop on Geothermal Reservoir Engineering, Stanford University, Stanford, California.

Ye, Z., M. Janis, and A. Ghassemi. (2017). Injection-driven Shear Slip and The Coupled Permeability Evolution of Granite Fractures for EGS Stimulation. In Proceedings of 51st US Rock Mechanics/Geomechanics Symposium, June 25-28, 2017, San Francisco, CA, USA: American Rock Mechanics Association.

Zafar, S., Hedayat, A., & Moradian, O. (2020). Evaluation of crack initiation and damage in intact Barre granite rocks using acoustic emission. In Geo-Congress 2020 (pp. 399–408). Reston, VA: American Society of Civil Engineers.

Zhao, C., Md S. Mia, A. Elbanna, and Y. Ben-Zion. (2024). Dynamic rupture modeling in a complex fault zone with distributed and localized damage. Mechanics of Materials 198: 105139.

Zhao, C. Abdelmeguid, M., Ibrahim, A. and A. Elbanna, (2025). "FARMS" : Fault And Rupture Mechanics Simulations, available at https://github.com/chunhuizhao478/farms.

Zietlow, W. K., & Labuz, J. F. (1998). Measurement of the intrinsic process zone in rock using acoustic emission. International Journal of Rock Mechanics and Mining Sciences, 35(3), 291–299.

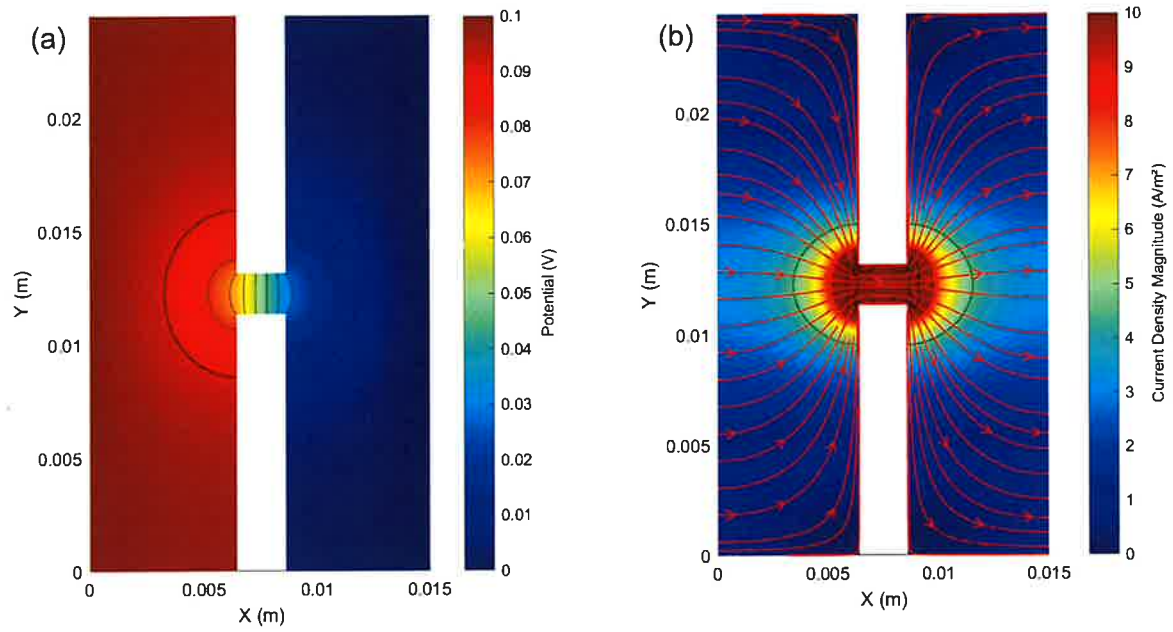

Figure 45. Simulated electric conduction in the constricted fracture: (a) Spatial distribution of electric potential; (b) Magnitude of the current density field and associated electric field lines.

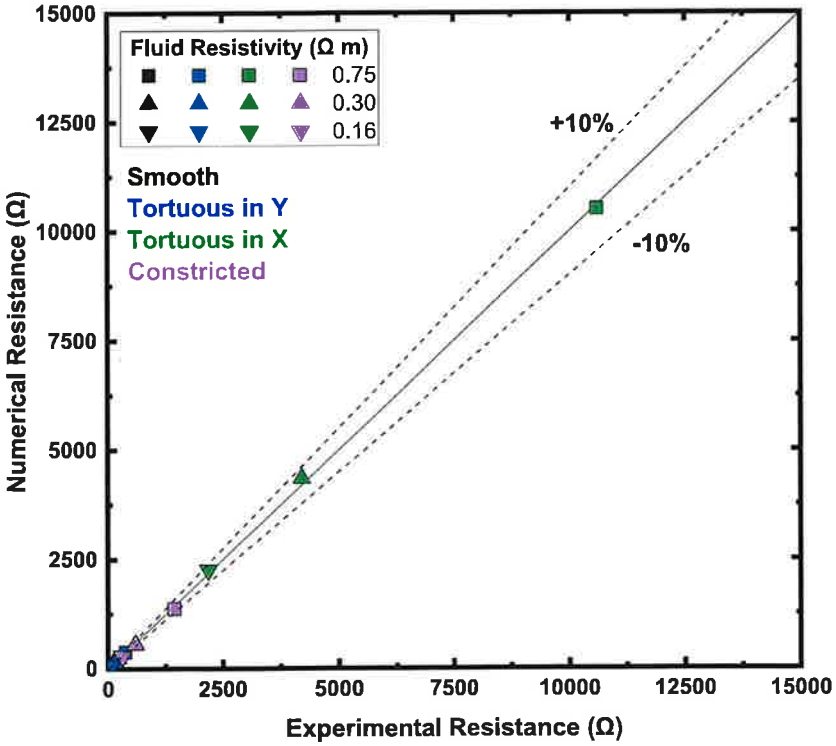

Figure 46. Comparison between the numerical and experimental resistances for four idealized fracture geometries (smooth, tortuous in Y, tortuous in X, constricted).

4.1.1.3 Effluent Chemistry & Geochemical Alterations of Fracture Surfaces

Laboratory fluid flow tests, using an acidic brine solution, were conducted on individual fracture surfaces of Sierra White granite at room temperature. Figure 47a&b show the variation of relative change in effluent conductivity and pH at 25°C, respectively, as a function of time during a representative fluid flow test, using acidic brine solution, on granite. The initial conductivity and pH of the solution in the monitoring reservoir at the start of the flow tests are also shown in the figures. In addition, the graphs include the data from the control experiment (without rock specimen) to determine if observed changes were greater or smaller than the systematic bias in the experimental set-up (the relative changes in conductivity and pH are always calculated with respect to the initial state of the solution in the reservoir). At the start of the test in granite, the conductivity of the solution in the monitoring reservoir was observed to be approximately 10% higher than that of the acidic-brine solution prior to its placement in the reservoir ($\sigma \sim 1{,}050$ µS/cm), possibly due to ion leaching from the pH probe. As observed in Figure 47a, there were two peaks in effluent conductivity that occurred at similar times to the control test, but with different magnitudes. During the fluid flow test in granite, the effluent conductivity increased by 17% within the first 4 hours of the test and then decreased following a trend similar to the control test. A steady state was not reached at any point during the test and the conductivity continued to decrease until it approached the value of the solution prior to its placement in the monitoring reservoir. This suggests a tendency of the fluid to return to its original chemical state. Throughout the test, the relative change in conductivity ranged from -10% to 17%. As shown in Figure 47b, the relative change in effluent pH ranged from -2% to 0%, with an average value of -1%, which are values similar to those of the control test. Given the similarity to the control test, the observed peaks in conductivity during this test are likely due to an increased concentration of potassium and chloride ions released by the pH probe during these two phases. Therefore, this behavior is attributed primarily to probe interference, rather than granite dissolution.

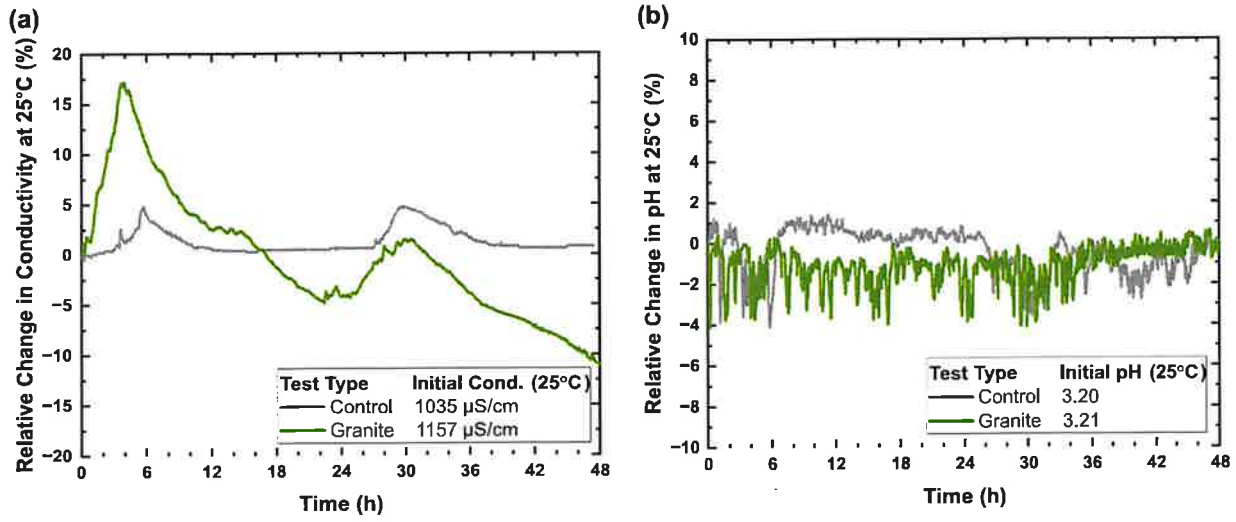

Figure 47. Relative change in effluent: (a) electrical conductivity; and (b) pH at 25°C with time, for granite. Note that the measurements obtained during the control test represent the systematic bias of the experimental set-up.

Figure 48 is a map of the difference in asperity height for the granite sample within the ROI from 3D X-ray microscopy. The asperity height differences for each fracture surface were calculated by subtracting the asperity height data before the test from the data after the test. Asperity height differences within the range of -0.08 to 0.06 mm represent the systematic bias of the measurement method and are therefore displayed in a uniform gray color. For the granite sample, the change in effluent conductivity and pH were negligible and minimal changes in fracture surface roughness were observed (Figure 48). Only 0.7% of the fracture area exhibited alterations greater than the systematic bias, with 0.4% showing positive asperity height differences (greater than 0.06 mm), which indicates localized precipitation, and 0.3% negative asperity height differences (less than -0.08 mm), indicating localized dissolution.

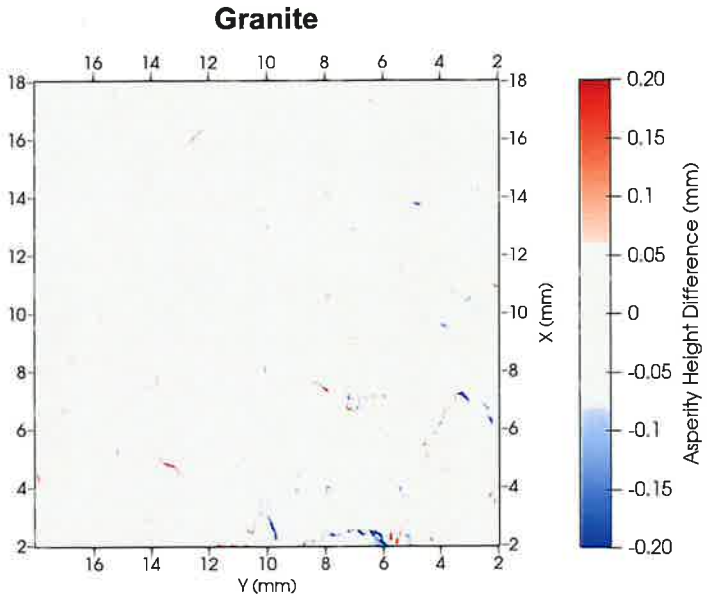

Figure 48. Spatial distribution of asperity height differences within the ROI for a fracture surface of granite obtained with 3D X-ray microscopy. The color scale represents the asperity height difference in mm. The zone between -0.08 and 0.06 mm represents the systematic bias of the measurement method.

Laboratory fluid flow tests, using a sodium chloride solution, were conducted on individual fracture surfaces of Sierra White granite at room temperature and at 120°C. Figure 49a shows the variation of relative change in conductivity at 25 °C and effluent temperature over time during a representative fluid flow test on a fracture surface of Sierra White granite at room temperature. During the 10-h flow test, the change in fluid conductivity was less than 0.5 %, indicating negligible chemical dissolution or alteration of the rock specimen by the brine solution. Representative results of the high-temperature fluid flow tests on Sierra White granite fracture surfaces are presented in Figure 49b. The relative change in conductivity and temperature of the fluid, together with the temperature readings of the two thermocouples are graphed as a function of time. Thermocouples T1 and T2 monitored the oven temperature and the temperature near the conductivity beaker, respectively. The total duration of the experiment was 75 hours with approximately 21 hours of brine flow. Throughout the test period, the relative change in

conductivity remained below 5 %. This result was supported by fracture surface roughness measurements that determined that the alterations were within the calculated measurement error.

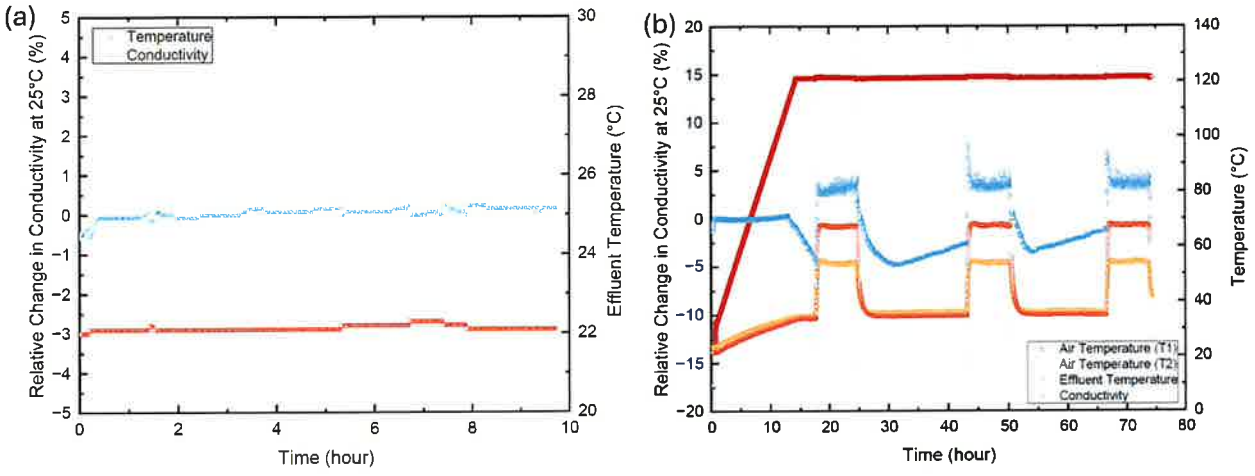

Figure 49. Relative change in conductivity at 25 °C and effluent temperature with time for: (a) a room temperature and (b) a high-temperature fluid flow test on Sierra White granite fracture.

4.1.1.4 Geophysical Monitoring of the Hydraulic & Mechanical Behavior of Rock Fractures

Laboratory flow-through experiments were performed on saturated rock fractures of Sierra White granite using a custom-made X-ray transparent core holder. Simultaneous measurements of electrical impedance reflected P-wave signals and permeability were performed on fractured cores under varying confining pressures (up to 5 MPa). The parallel plate model for flow and electric conduction was used to provide estimates of hydraulic and electric mean aperture.

Figure 50 shows representative reflected P-wave signals recorded by the transducer located at the midpoint of the fractured specimen. The peak amplitudes of the reflected waveforms generally decrease with increasing confining pressure, with changes becoming negligible above 3 MPa. This decrease in reflected wave amplitude with increasing stress is attributed to progressive fracture closure and increased contact area, which reduce the acoustic impedance contrast across the fracture. Reflected wave amplitudes corresponding to the fourth major peak (see Figure 50) are plotted as a function of confining pressure in Figure 51. The graph also includes the reflected wave amplitude measured after the fracture was unloaded back to 50 kPa. The reflected P-wave amplitude generally decreases with increasing confining pressure, reflecting progressive fracture closure. Up to a confining pressure of 750 kPa, the amplitude drops by approximately 40% relative to the initial value. Between 750 kPa and 1–1.5 MPa, a slight rebound of about 1% is observed, possibly due to minor readjustment of microcontacts, after which the amplitude continues to decrease, reaching a total reduction of 43% at 5 MPa. This trend indicates that the fracture's contact area increases progressively with pressure, with most asperities coming into contact at intermediate pressures. As shown in Figure 51, when the fracture is unloaded back to 50 kPa, the reflected wave amplitude returns to a value similar to that observed at a confining pressure of 250 kPa, indicating partial fracture closure and hysteresis in the response.

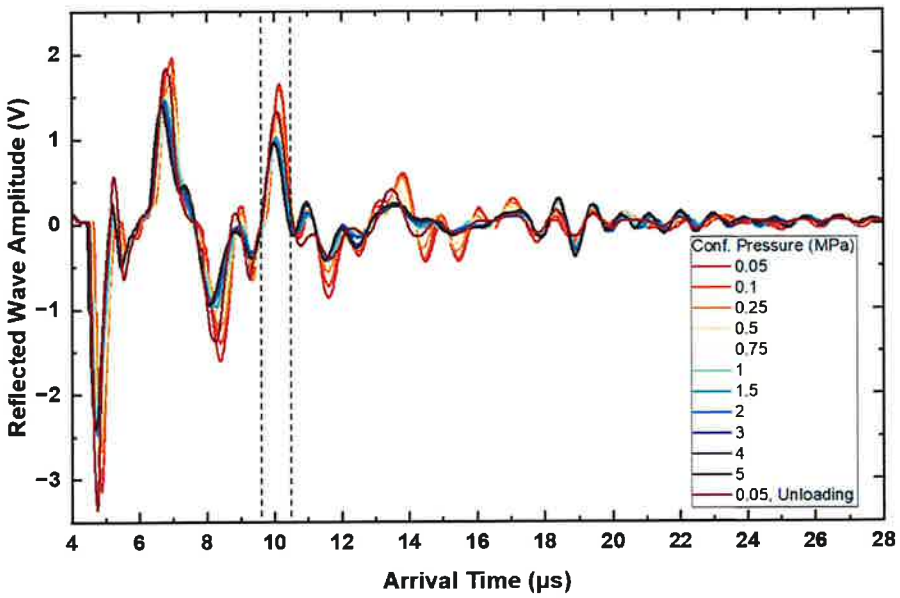

Figure 50. Reflected P-wave signals at different confining pressures.

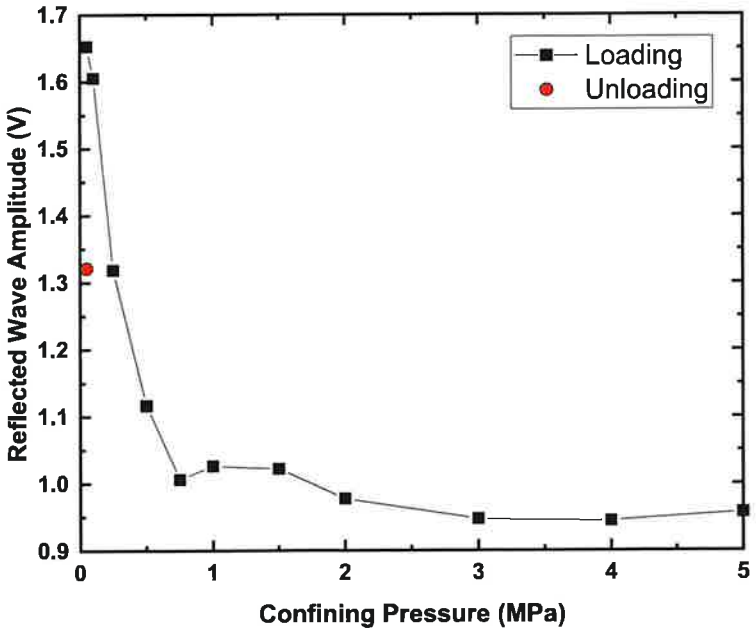

Figure 51. Reflected wave amplitude as a function of confining pressure.

Figure 52 shows the Bode plots of the measured impedance at each confining pressure. These measurements reflect the electrical resistance of the middle section of the specimen, which has an approximate length of 15 mm. At low frequencies (below 1 Hz), the impedance magnitude is relatively flat and the phase angle approaches zero (within 7°). This indicates that the electrical

response is dominated by bulk conduction through the fluid-filled fracture, behaving nearly as a pure resistor. In contrast, increasing the confining pressure significantly alters the frequency response at higher frequencies, where capacitive contributions from the fluid–rock interface become more pronounced. The evolution of impedance magnitude at 0.01 Hz with increasing confining pressure is shown in Figure 53. The graph also includes the impedance amplitude measured after the fracture was unloaded back to 50 kPa. As shown in Figure 53, the impedance rises sharply by about 160% up to a confining pressure of 750 kPa. A rebound of approximately 30% occurs between 750 kPa and 1 MPa, likely due to minor microcontact adjustments and fluid redistribution effects, after which the impedance continues to increase, reaching a total increase of 238% at 5 MPa. This trend in impedance reflects progressive fracture closure, in which the aperture decreases and more asperities come into contact, while the fluid is forced through increasingly tortuous paths, leading to higher impedance. Finally, when the fracture is unloaded back to 50 kPa, the impedance returns to a value similar to that observed at confining pressures of 100–250 kPa, indicating partial fracture closure and hysteresis in the response. Both the reflected P-wave amplitude and measured impedance show similar trends, both reflecting the fracture's progressive closure with increasing confining pressure.

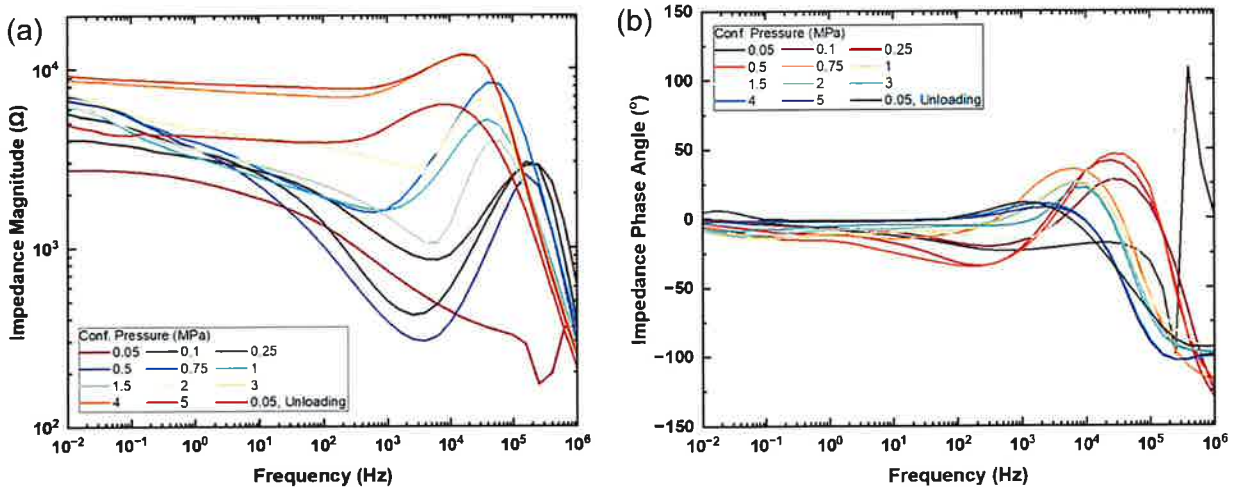

Figure 52. Bode plots of a fluid-filled granite fracture under varying confining pressures.

Figure 55 compares the electric and hydraulic fracture apertures as a function of confining pressure. The hydraulic aperture represents the mean aperture for flow (Figure 54) along the entire length of the specimen, while the electric aperture reflects the central portion of the fracture (approximately 20% of the total fracture length). Both measurements show a decreasing trend with increasing confining pressure, reflecting progressive fracture closure. A change in the trend, indicating a shift in the rate of reduction with pressure, is observed at approximately 750 kPa for both cases. However, the change is more gradual and smoother for the hydraulic aperture, whereas the electric aperture exhibits a small rebound of approximately 5% at 750 kPa before continuing to decrease with increasing confining pressure. It is also observed that, below 750 kPa, the electric aperture remains smaller than the hydraulic aperture, while above 750 KPa, a change in the trend is observed, and the electric aperture becomes larger than the hydraulic aperture. A possible explanation is that below 750 kPa, the central part of the fracture (represented by the electric

aperture) closes more tightly than the edges, resulting in smaller electric than hydraulic apertures. Above 750 kPa, the trend reverses as the central region resists further closure, while the edges continue to deform.

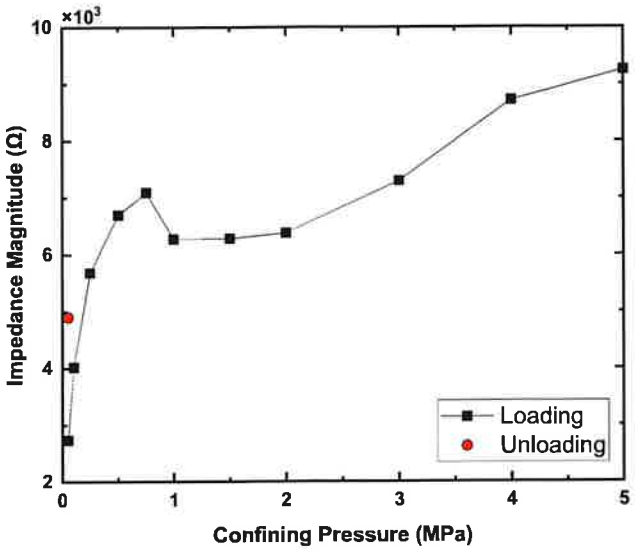

Figure 53. Impedance magnitude at 0.01 Hz as a function of confining pressure.

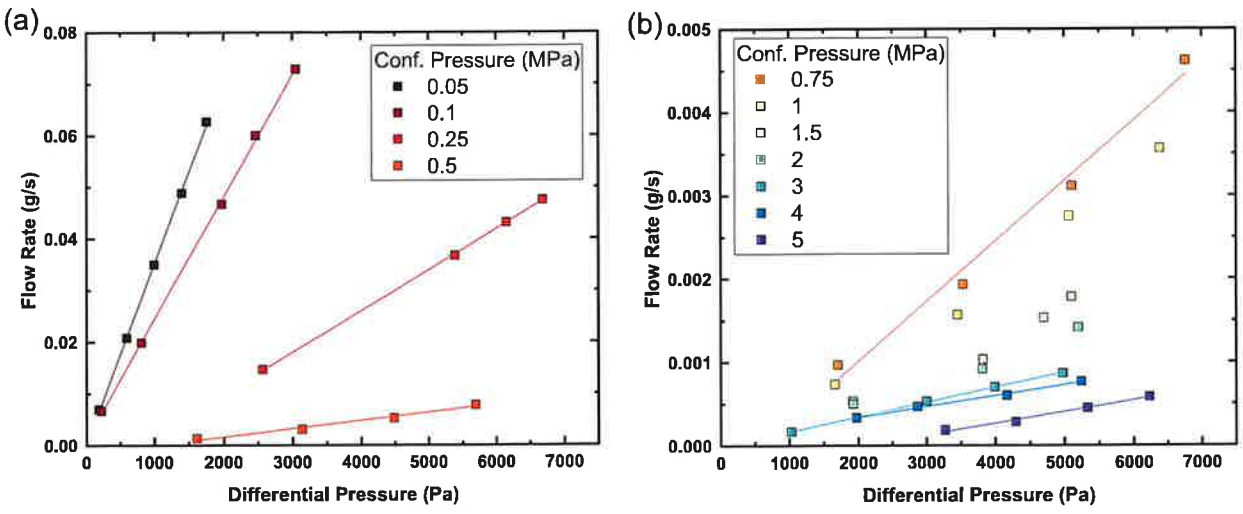

Figure 54. Flow rate versus differential pressure for a granite fracture at different confining pressures.

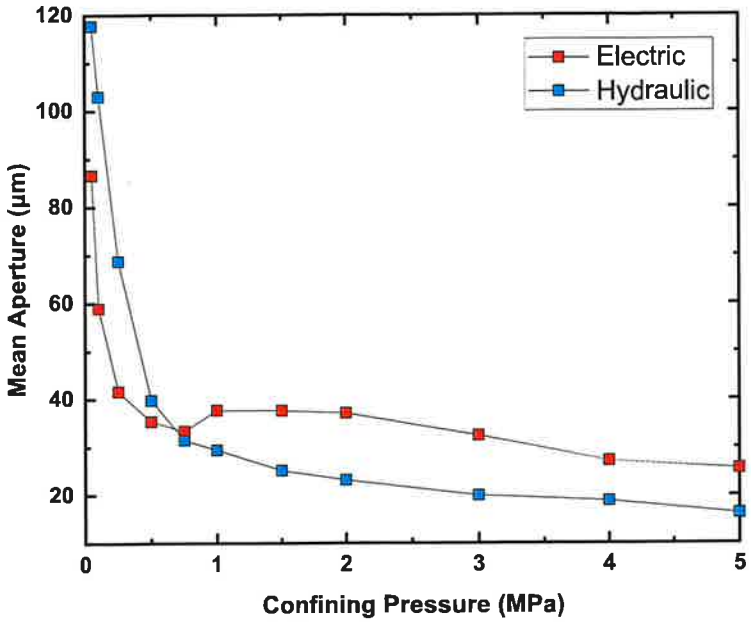

Figure 55. Comparison of electric and hydraulic fracture apertures under varying confining pressures.

4.1.1.5 Role of Gouge on Shearing

Coefficient of friction: dry vs. saturated: Figure 56 shows the coefficient of friction and shear displacement rate as a function of shear displacement. The coefficient of friction is higher for lower effective pressure. The saturated test at 75 MPa P_E has similar results to the dry test at the same conditions. Effects of shear displacement rate changes are observed in all tests, as the coefficient of friction temporarily drops with decreases in the rate and temporarily increases with increases in the rate.

Shear Behavior of Saturated Granite Joints: Shear stress versus shear displacement for all three specimens are shown in Figure 57. Despite having a high coefficient of friction, the shear stress is much lower for the 15 MPa P_E test. Differences from rate changes are muted. Shear stress increases with increasing confinement. Shear stress results are similar for the 75 MPa P_E tests, wet and dry. At higher displacements, shear stress drops slightly for dry samples compared to saturated samples.

Overall, measured coefficients of friction conducted on pulverized Sierra White granite (SWG) for a range of effective pressures, displacement rates, and saturation states are within the expected range for silicate rocks. Behavior with rate changes is consistent with rate-and-state friction formulations to enable calculations of *a-b* parameters for modeling inputs (e.g., Mei and Rudnicki, 2023).

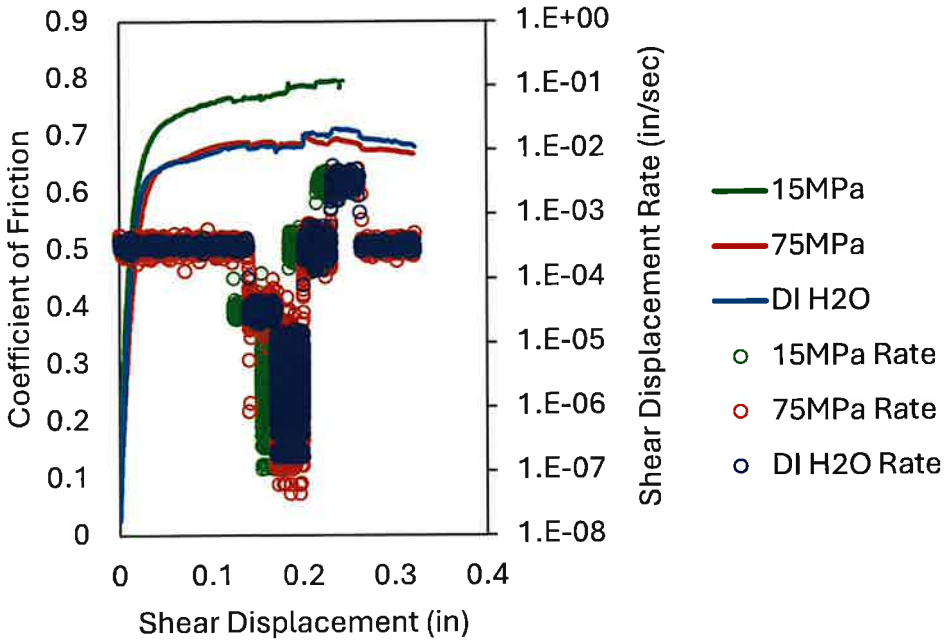

Figure 56. Coefficient of friction and shear displacement rate versus shear displacement under three different experiments. 15 MPa and 75 MPa rates were performed under dry condition and DI H_2O rate was performed at 75 MPa under water-saturated (wet) condition.

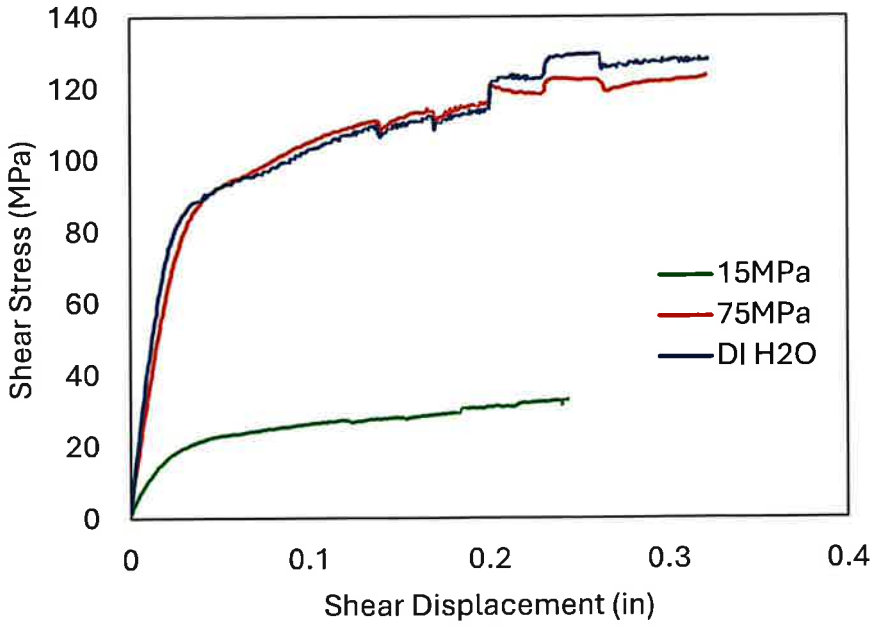

Figure 57. Shear stress versus shear displacement.

4.1.1.6 Crack Initiation and Formation during Wellbore Breakout

Figure 58 shows failure strengths of six borehole breakout tests and the differential stress as a function of axial strain. Results are compared against previous testing at similar conditions for dry SGW (Choens et al., 2018) as a reference case. Failure strengths are significantly impacted by temperature from room to 150 °C and by the presence of fluid. For example, failure strength in the water wet condition has decreased from 207.7 MPa at room temperature to 181.6 MPa at 150 °C, while failure strength at room temperature decreased from 221.1 MPa under dry condition to 207.7 MPa at water wet condition. The effect of temperature on failure strength under wet conditions was much higher from room to 100 °C, compared to from 100 to150 °C. All tests displayed similar loading curves despite varying temperature and fluid conditions, suggesting that Young's Moduli values are relatively similar for the different conditions tested. Stress-strain data also shows that sample did not yield (or just yielded before failure) at room temperatures until failure, but tests at higher temperatures (100 and 150 °C) did yield prior to failure.

Acoustic Emission Results: Although AE signals were observed during all tests, the quantity and quality of observed AE data depends on the testing conditions, primarily due to the integrity of AE pins at high temperature conditions. Hence, we report only three testing conditions where clear AE signals were observed as shown in Figure 59. Overall, AE signals have been recorded the highest at the dry condition, while AE hits decreased with the addition of water into the borehole and decreased further at elevated temperatures of 150 °C. A number of AE hits at 150 °C were only ~10% of the observed levels of the dry test, partly, due to fewer AE pins functional during the test. However, a number of hits per each pin still remain significantly lower than those in the dry test.

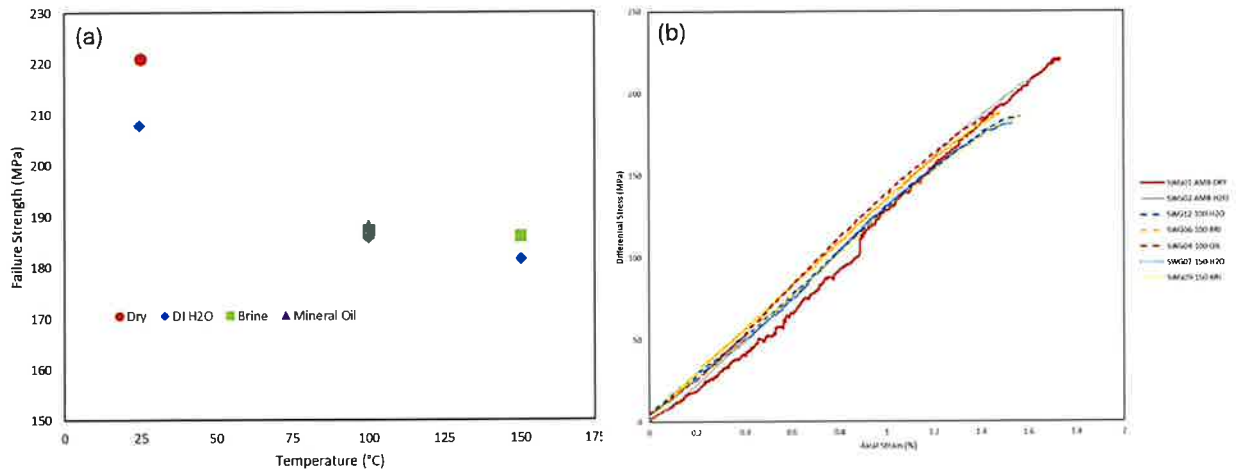

Figure 58. (a) Failure strength versus temperature for four different fluid conditions and (b) differential stress versus axial strain for borehole experiments. (a) Failure strength versus temperature for four different fluid conditions and (b) differential stress versus axial strain for borehole experiments. Note that loading has been stopped manually when borehole failure got started. In test names of SWG##-XXX-YYY, ## is a testing number, XXX is an experimental temperature (AMB for ambient room temperature), and YYY is the dry/wet fluid conditions. All experimental data is available at GDR in Yoon and Choens (2025).

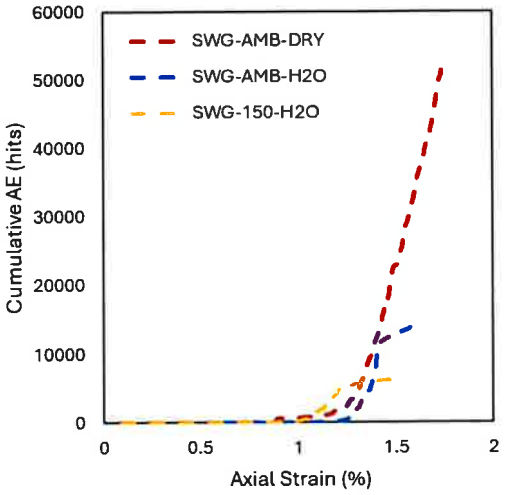

Figure 59. Cumulative AE hit versus axial strain for three testing conditions.

AE development differed for wet and dry tests (Figure 60 & Figure 61). Once AE initiated in the dry tests, levels quickly increased and remained at a nearly constant rate for the remainder of the tests. In the wet test at ambient temperature, AE initiation occurred later than the dry test. AE levels increased to rates similar to the dry tests, but dramatically slowed after 1.4% axial strain where AE increased at a much lower rate. For the test at 150 °C, the rapid onset of AE occurred at lower strain than the other experiments, and similarly slowed after 1.2% strain to a lower rate.

AE events were located for dry and wet tests conducted at room temperatures and evolution of event locations are shown in Figure 60. In the dry test, AE events are concentrated in the center of the sample where the borehole is located, and clusters of AE events are densely observed around the wellbore location. AE events cluster in a ~20 mm diameter circle at the center of the sample and remain at a low level closer to the outer diameter of the sample. The events are not evenly distributed along the length of the wellbore, either. In the wet test, AE events are clustered along fracture growth plane(s) away from the wellbore. Events cluster in the center of the sample where the borehole is located, but a linear feature extends downward and to positive Y positions in this view.

In the dry test, during the early stage of loading, AE activity remains minimal while differential stress and axial strain increase steadily, reflecting stable elastic deformation. A sharp spike in absolute energy around 3500 s occurs prior to significant AE activity, likely signaling an early episode of microcrack linkage or partial fracture within the sample. Following this, AE hits increase rapidly between 4000 – 4700 s, marking the main phase of distributed cracking and coalescence leading to macroscopic failure. A temporary reduction in AE hits near 4800 s indicates brief relaxation after partial failure, followed by renewed AE bursts as deformation focuses along the dominant fracture. Overall, the dry sample shows a delayed but intense AE response, with the highest total number of events and longest time to failure among the tested conditions. This behavior suggests that in the absence of pore fluids, the rock accommodates greater stress accumulation before undergoing sudden brittle failure, producing a pronounced energetic release once instability initiates.

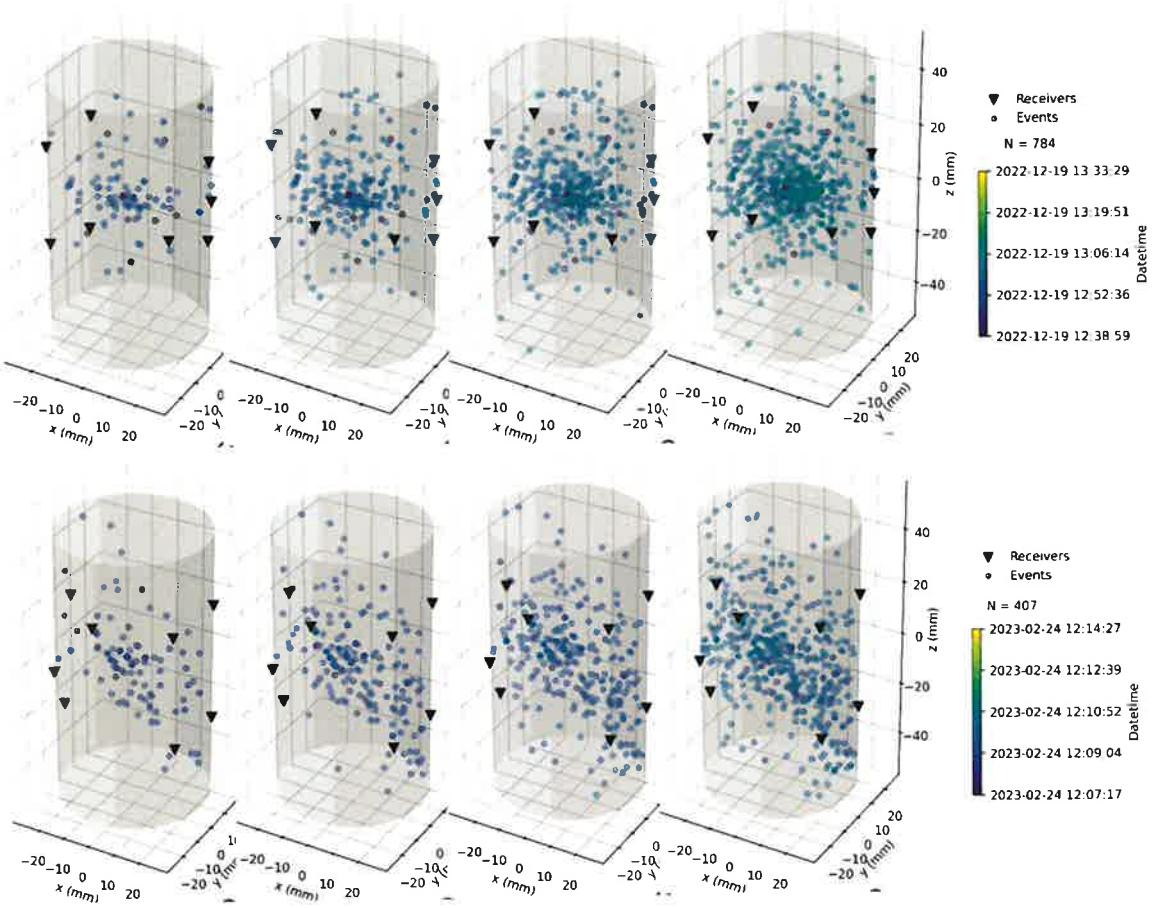

Figure 60. Evolution of located events over time for dry (top) and water-wet (bottom) conditions.

In the water wet test at room temperature, AE activity in the wet experiment begins slightly earlier in the loading cycle than in the dry condition, around 2200 s, even though differential stress continues to increase smoothly. This early onset of AE suggests that the presence of pore fluids promotes microcrack initiation at lower stress levels by reducing effective normal stress and facilitating fracture opening. Between 2400–2550 s, AE counts increase sharply and reach a broad peak that coincides with several short-lived spikes in absolute energy, indicating repeated microfracture growth and local stress redistributions. The temporal clustering of these bursts reflects a more distributed failure process rather than a single dominant rupture event. The experiment terminates at a significantly shorter total duration (~2800 s) compared to the dry case, with lower differential stress at failure, confirming that fluid saturation accelerates damage accumulation and weakens the sample. Overall, the wet condition exhibits an earlier onset, shorter duration, and more frequent energy bursts, consistent with fluid-assisted crack propagation and reduced fracture strength under hydrostatic conditions.

In the wet and high temperature condition AE activity begins around 3000 s, similar to the dry experiment, marking the onset of distributed cracking under increasing differential stress. The mean absolute energy rises later, after AE hit rates have already intensified, indicating that while

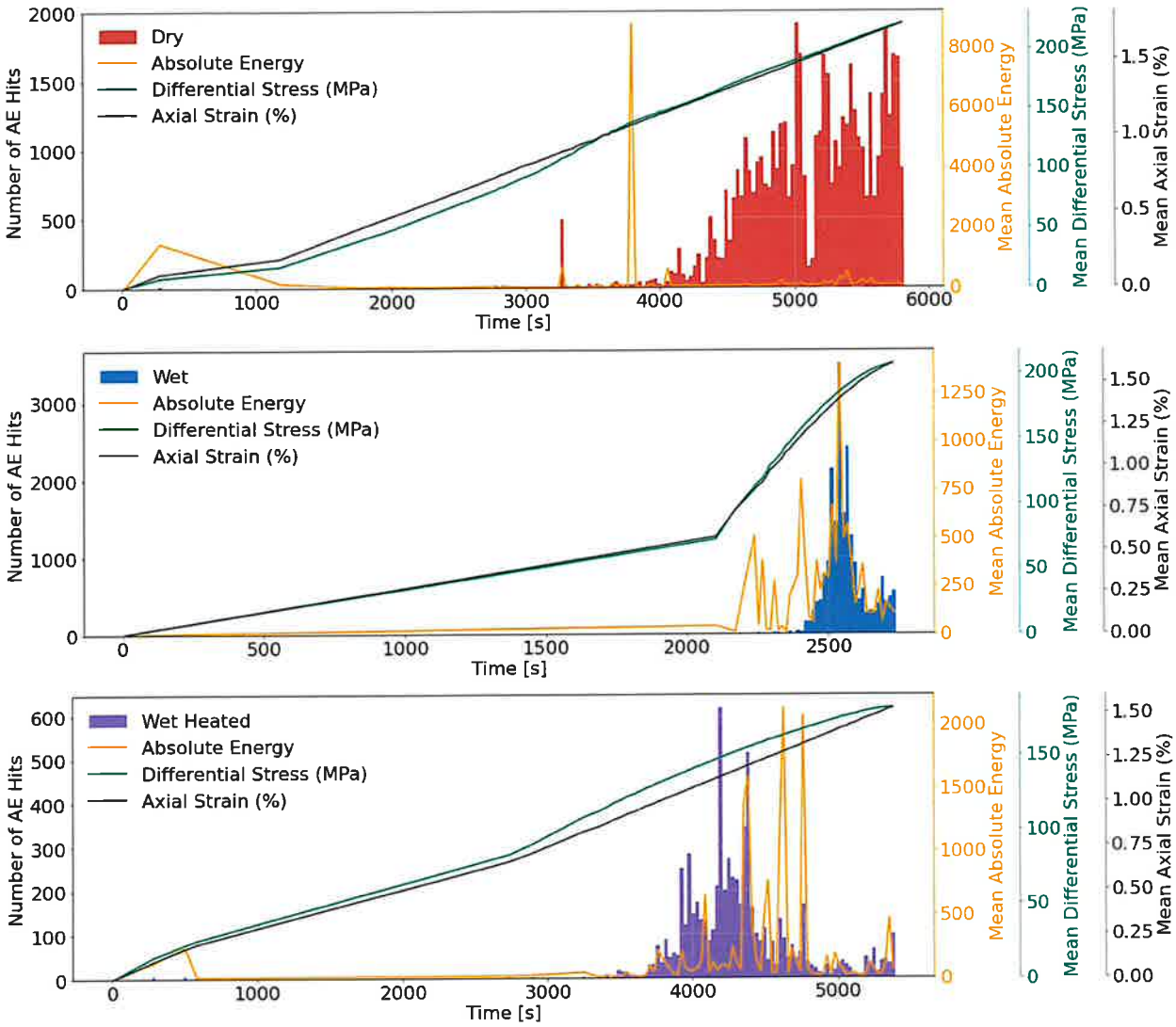

Figure 61. Time evolution of AE activity, mechanical stress, and strain during wellbore breakout experiments conducted under (top) dry, room temperature, (middle) water-wet, room temperature, and (bottom) water-wet, 150 °C conditions. Histograms represent the number of AE hits per time interval (left axis), and overlaid curves show the evolution of mean absolute energy (orange), mean differential stress (green), and mean axial strain (black) (right axis). Stress-strain data is available at GDR in Yoon and Choens (2025).

many low-energy microcracks form early, individual events become progressively more energetic as damage localizes and fractures begin to coalesce. AE activity remains intermittent throughout the test, with clusters of events between 3500–4500 s corresponding to episodic energy release, despite the smooth, continuous increase in stress and strain. The total number of AE hits is lower than in the dry and wet experiments, but the delayed increase in absolute energy suggests that fewer, higher-energy events dominate the later stages of deformation. Overall, the wet heated condition exhibits AE onset timing comparable to the dry sample but a delayed and amplified energy response, consistent with thermally assisted weakening and fluid pressurization, which promote localized, high-energy fracture during the final approach to failure.

Microstructural analysis of wellbore breakout samples: The sample from the dry test and the wet samples from ambient temperatures and 150 °C were imaged using microCT scans and the microscope (Figure 62). In the dry test, damage is concentrated at the borehole wall, and large fractures do not extend away from the borehole. Sharp, triangular borehole breakout-like features form at the borehole wall on the plane perpendicular to axial loading direction. Fractures grow from the end of these breakouts that run roughly concentric to the borehole but do not extend past the borehole towards the ends of the sample.

In the wet sample deformed at ambient temperature, fractures emanating from the borehole extend past the borehole and towards the end of the sample. Fractures extend upward on the left side, and downward on the right side. Note that the loading direction in the thin section is from top to bottom. Fractures running perpendicular to the axial loading direction cut from these fractures back to the top and bottom of the borehole. Breakout formation is defined by a broader, rounded zone of damage in the wet sample. Fractures grow from the end of the borehole towards the end of the sample. Multiple fracture strands can be observed. Fractures can be seen growing in both directions from each borehole, but upward fractures on the left and downward fractures on the right have higher apertures.

In the wet sample deformed at 150 °C, fractures grow towards the end of the sample. Fractures extend upward on the right side, and finer fractures extend downward on the left side. Further developed fractures running perpendicular to the axial loading direction cut from the larger fractures back to the top and bottom of the borehole. At the borehole wall, the sample displays very broad and rounded breakouts (Figure 62, right). The breakout on the left side encompasses most of the borehole wall. Fractures grow from the end of the borehole towards the end of the sample. Multiple fracture strands and diffuse networks can be observed. Fractures can be seen growing in both directions from each borehole, but downward fractures on the right have higher apertures.

Figure 63 shows transmitted polarized microscopic images for wet samples at room temperature and at 150 °C with key minerals identified. Localized, dense arrays of parallel trans-granular (primarily along loading direction) are clearly shown and intra-granular microfractures are primarily in quartz, less in feldspar, none/rare in biotite at breakout. Higher microfracture densities are observed at room T than at 150 °C, indicating that multiple minerals underwent higher deformations before failure (i.e., higher failure strength at room T). Intragranular microfractures are more common directly adjacent to the main trans-granular microfractures and are usually subparallel to the loading direction. Microfractures in quartz tend to be subparallel to loading/main fracture directions. Especially, local deflections around quartz grain boundaries occur on microfractures oriented at high angle to loading direction, while curved microfractures in quartz are consistent with point-contact fracturing at boundaries with biotite and other quartz grains. Microfractures in plagioclase/feldspar are commonly deflected by cleavage planes, resulting in stepped or inclined microfractures where these cleavage planes are not parallel to the main fractures.

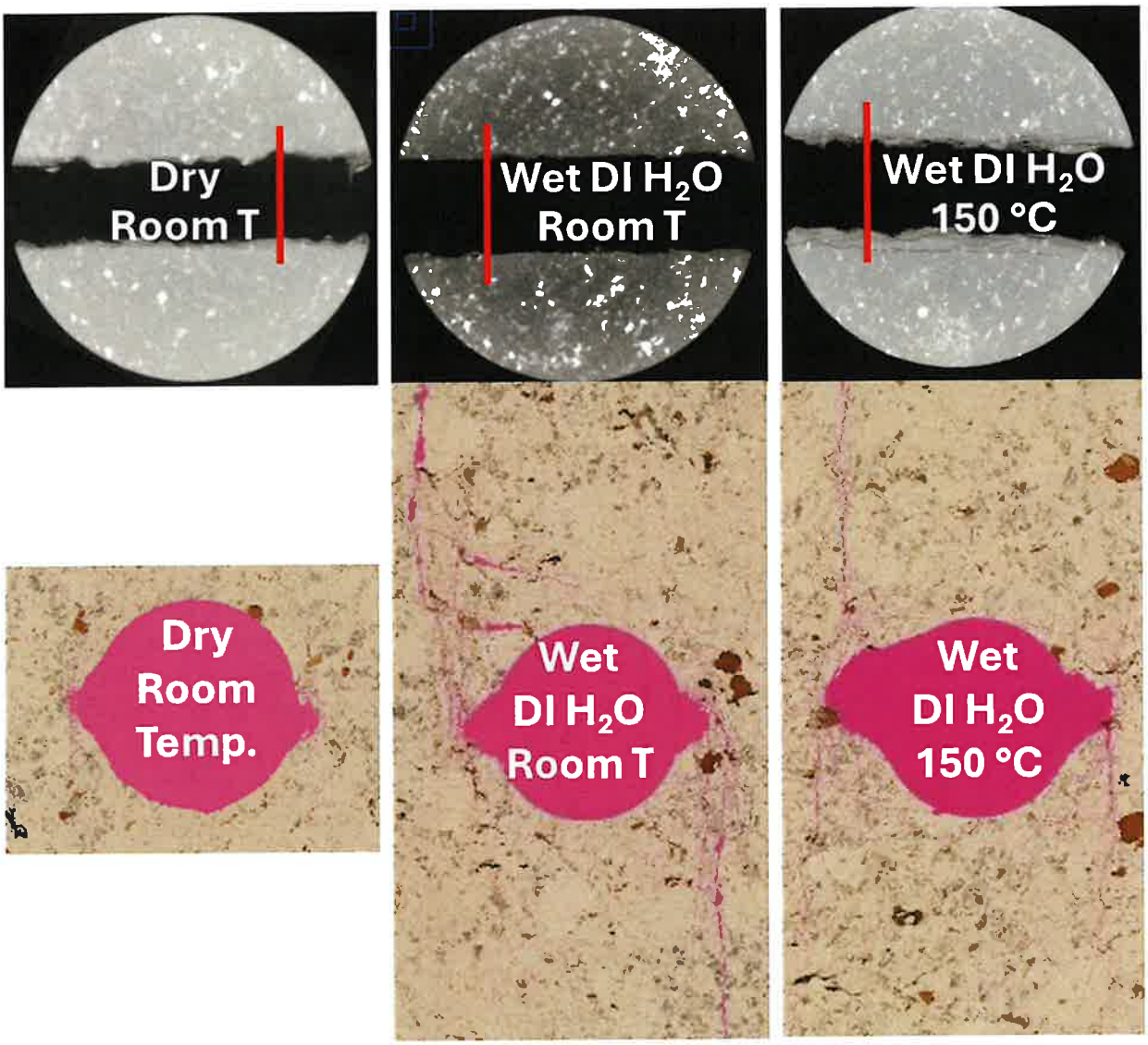

Figure 62. Microstructural observations for SWG-AMB-DRY, SWG-AMB-H2O, and SWG-150-H2O samples. Top images show horizontal microCT slices (perpendicular to the vertical loading direction) with central wellbore and bottom images show the reflected optical images of thin sections along the vertical loading direction from top to bottom. Pink color is an epoxy to show damages and micro-cracks around central wellbore. Thin section samples were taken along the vertical direction of cylinder sample across the wellbore along the red line in CT images.

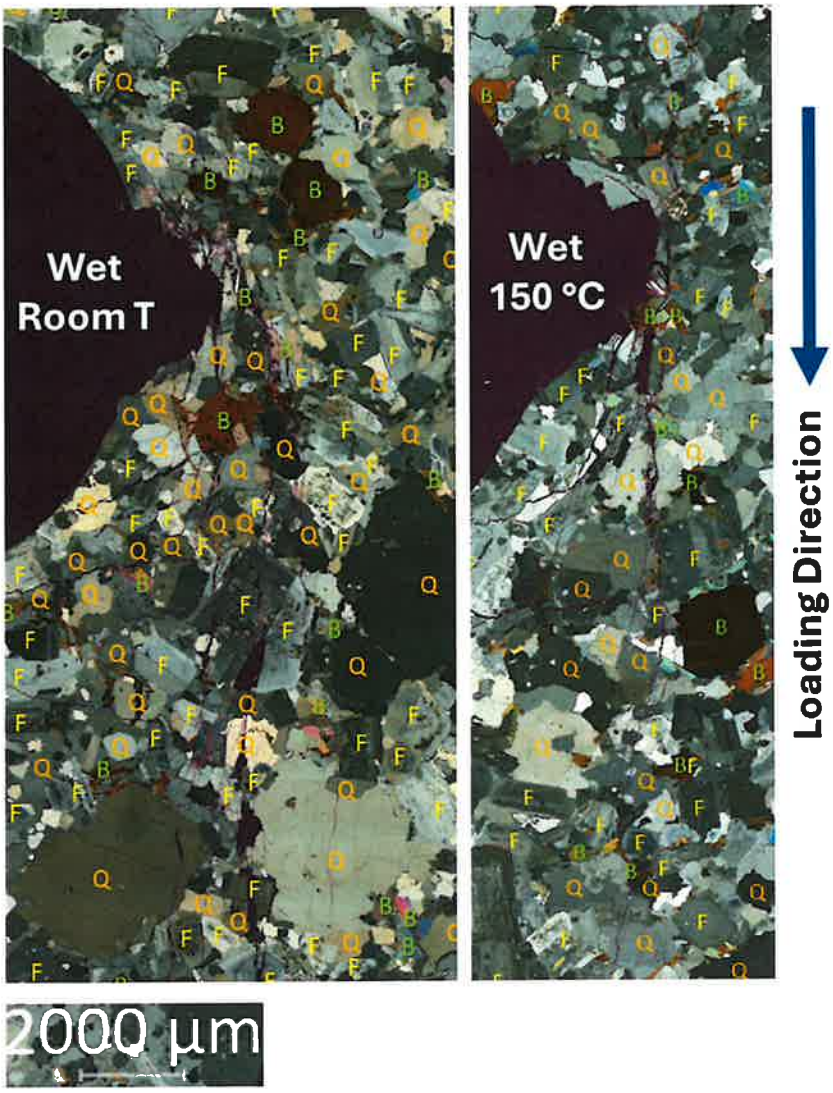

Figure 63. Transmitted polarized microscopic images captured at 100X total magnitude for SWG-AMB-H2O and SWG-150-H2O samples. Corresponding reflected mode images are shown in Figure 62. Quartz (Q), Plagioclase/K-Feldspar (F), and Biotite(B) are identified. At this transmitted mode, Plagioclase/K-Feldspar are not discernable.

4.1.2 Theoretical Analysis of Rate-and-State Friction

We reviewed extensive hydrothermal friction experiments on single, mixed, and natural gouges (Mei et al., 2024). These experimental results show that steady-state friction and fault stability vary significantly with temperature, gouge types, sliding velocity, and normal stress. We also examined four friction models under hydrothermal conditions. The extended microphysically based Chen–Niemeijer–Spiers (CNS) model (Mei and Rudnicki, 2023) represents an advancement over the ad-hoc parameter adjustments commonly used in standard rate-and-state friction. The model successfully reproduces laboratory measurements on granite gouges, revealing temperature-dependent variations in frictional parameters within the range of approximately 150–350 °C. These changes promote seismic slip within this temperature range. The microphysical CNS friction has

been incorporated into a spring-slider model that accounts for the effects of injection pressure rate, gouge permeability, and bulk permeability. Compared with the standard rate-and-state friction law, the CNS model tends to favor slow slip behavior. While rapid pressure increases may trigger more frequent seismic events, they ultimately tend to stabilize fault slip.

4.1.3 Simulation Results of MOOSE-FARM

Constitutive equations for modeling dynamic frictional fracture 2D and 3D elastodynamics with a continuum damage-breakage model (MOOSE-FARMS: FAult and Rupture Mechanics Simulations) have been implemented as a stand-alone module to MOOSE (e.g., Zhao, 2025). The code includes two of the most widely used friction laws: (1) the slip-weakening friction law and (2) the rate-and-state friction law and can perform simulations with and without pore pressure that account for dynamic poro-elastic effects on damage evolution representing fracture initiation, propagation, and coalescence. Here we report our early work using the cohesive zone model (CZM) on fracture ruptures due to fluid injection as the first example. Note that we updated our model using a continuum damage-breakage (CDB) model as described in the method section (Section 3.3) to implement an implicit integration scheme computationally efficiently for the coupled diffusion-deformation during both the slow deformation and fast rupture phases using adaptive time stepping in an implicit time integration scheme. This updated model has been used for our validation against wellbore breakout tests as the second example.

Dynamic rupture of fracture network with fluid injection: This problem is demonstrated in the 2D plane strain setting to manage the computational cost. The implementation, however, is consistent with 3D solid mechanics formulation. For this part, we utilize the cohesive zone model to represent frictional sliding on fault interfaces that can also potentially open. The evolution of pore pressure due to fluid injection is modeled using the analytical solution for continuous fluid mass injection in poroelastic media developed by Rudnicki (1986). The model used in this problem considers the effect of fluid pressure on the effective stress of the solid matrix and its bulk and interfacial strengths.

To illustrate the effects of injection location, we consider two cases: on-fault injection and off-fault injection in a small region (i.e., 1600m by 1600m) with each fault length of 200m. Each fault is idealized as straight segment with its frictional behavior governed by linear slip weakening law. All model parameters are listed in Table 5. As shown in Figure 64, the injection location has pressure at 30% of the mean stress (100MPa) of the background stress. On the left figure, the injection pressure is applied directly on the fault, whereas on the right figure, the injection pressure is applied in the surrounding media. We assume the calculation starts at injection after 1 day for pressure to reach a desired level. The pressure time history at the injection location is also given.

Figure 65 shows particle velocity time history, highlighting the fault which pressure is directly applies to nucleates due to the drop of the effective normal stress which governs the fault strength. The rupture carries stress perturbations and quickly nucleates surrounding faults, which ends up with a complex velocity field. Figure 66 shows the shear wave speed ratio that represents shear wave speed reduction as well as damage accumulation. We observe the predominant locations for

reduction to take place are corners or intersections where the faults are unable to propagate, thus releasing significant energy on the off-fault media. This is an example of how rupture affects the material properties of off-fault bulk media during a dynamic rupture event. The continuum damage-breakage model can capture the bulk damage due to fluid injection on the off-fault as well. As shown in Figure 67, as the first rupture nucleates, it carries stress perturbations and complicate the velocity field in the faults in the same way as in the previous on-fault injection case, with the damage located at the corners and around the injection location (Figure 68). This is an example of how off-fault damage could affect the fault nucleation by perturbing the surrounding deformation field. In Figure 68, the injection produces damage which spreads out in the bulk media

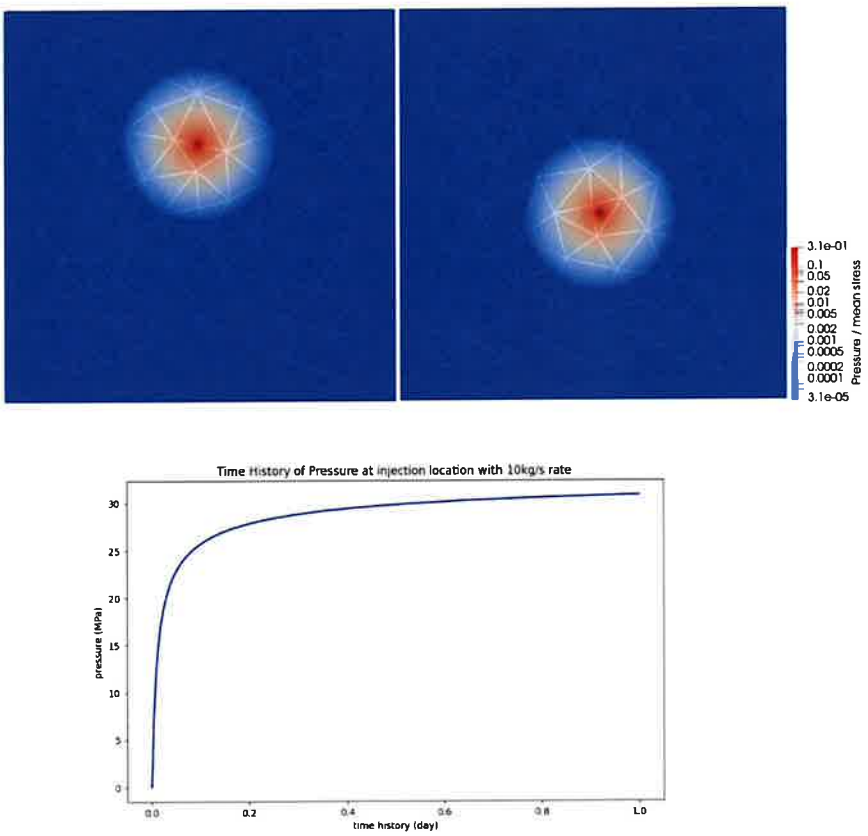

Figure 64. (Top) Distributions of the ratio of pore pressure to the mean stress (100 MPa) for two injection locations (on-fault (left) and off-fault (right)) and (bottom) pressure time history at injection location.

Table 5. Material Properties for Dynamic Rupture of Fault Network with Fluid Injection

Poroelastic Properties	**Value**	**Unit**	**Comments**
Shear Modulus μ	32.04	MPa	
Drained Poisson Ratio ν	0.25	-	
Undrained Poisson Ratio ν_u	0.3	-	
Biot Coefficient α	0.31	-	
Transport Properties	**Value**	**Unit**	**Comments**
Permeability k	3×10^{-12}	m^2	
Fluid Viscosity η	0.4×10^{-3}	Pa s	
Hydraulic Diffusivity	10^{-2}		
Reference Fluid Density ρ_o	10^3	kg / m^3	
Volume Injection Rate q/ρ_o	1	m^3/s	
Rock Material Properties	**Value**	**Unit**	**Comments**
Internal Friction Angle ϕ	46.8	Degree	
Density ρ	2650	kg / m^3	
Initial Stress Condition	**Value**	**Unit**	**Comments**
Stress σ_{xx}	-135	GPa	
Stress σ_{yy}	-120	GPa	
Stress σ_{xy}	70	GPa	
Damage-Breakage Properties	**Value**	**Unit**	**Comments**
Strain invariant ratio: onset of damage evolution ξ_o	-0.8	-	Material property associated with internal friction angle
Strain invariant ratio: onset of breakage evolution ξ_d	-0.9	-	
Compliance or fluidity of the fine grain granular material C_g	10^{-10}	1/(Pa*s)	
Flow rule index m_1, m_2	10, 1	-	
Damage solid modulus γ_r	37.15	GPa	
Critical point of three phases ξ_1	0.8248	-	
Coefficients for granular stress a_0, a_1, a_2, a_3	7.4289, -22.14, 20.929, -60.672	GPa	
Damage rate C_d	10^6	1/s	
Breakage rate C_B	10^7	1/s	
Damage healing rate C_1, C_2	300, 0.05	1/s	
Breakage healing rate C_{BH}	10^4	1/s	
Width of transitional region β	0.03	M	
Slip Weakening Friction Properties	**Value**	**Unit**	**Comments**
Characteristic length Dc	0.4	M	
Static friction coefficient μ_s	0.677	-	
Dynamic friction coefficient μ_d	0.4	-	
Fault Geometry Dimensions	**Value**	**Unit**	**Comments**
Fault segment length L_f	1	Km	
Domain Length L	30	Km	
Mesh Size Δx	30 (800)	M	Fault region (outer boundary)
Time Step Δt	2×10^{-4}	S	

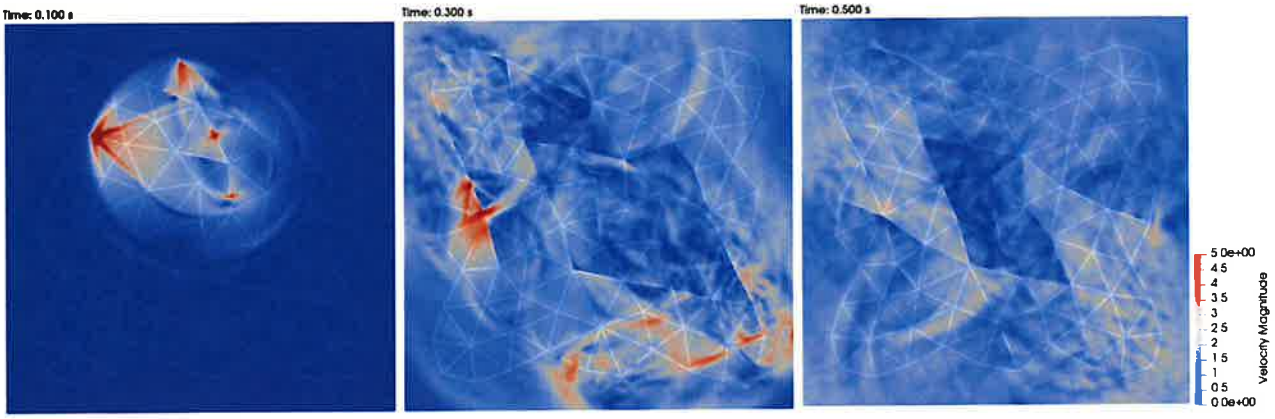

Figure 65. Particle velocity distribution of on-fault injection at three different times.

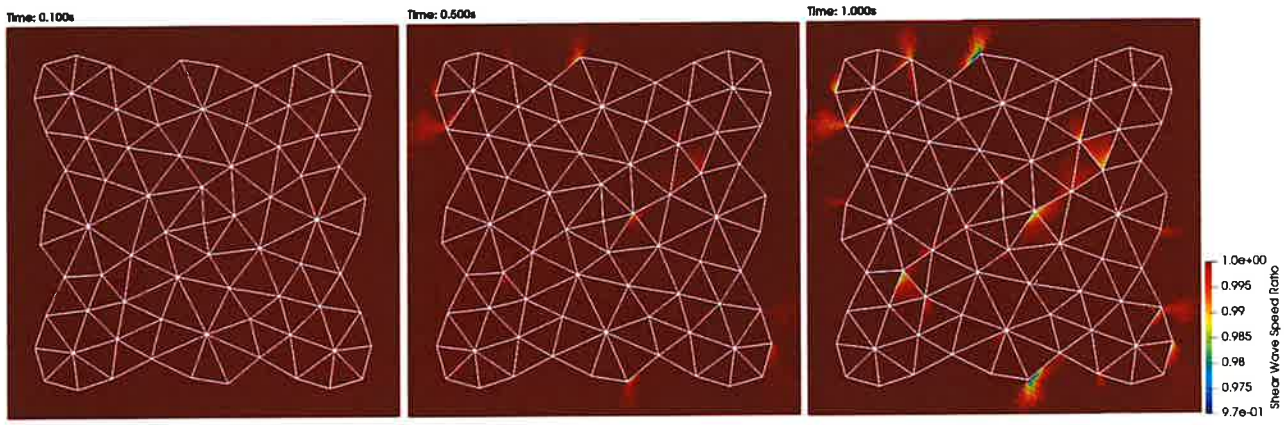

Figure 66. Shear wave speed ratio distribution of on-fault injection at three different times.

and touches the nearby fault, which is responsible for the nucleation of rupture on the nearby fault. As a detailed value check, the pressure along that fault segment is around ~7MPa, whereas the required normal stress reduction for shear strength to overtake shear stress is around ~10MPa, so the normal stress reduction alone cannot promote the nucleation, but the deformation near the fault caused by the damage contributes to the nucleation of rupture as well.

Computational verification on synthetic 3D wellbore breakout tests: We verified our model implementation with 3D synthetic wellbore breakout tests. Model parameters and material properties are listed in

Table 6. Following Rudnicki (1986), we setup the problem as shown in Figure 69. We assume the prescribed pressure is applied initially and hole is drilled to mimic the wellbore breakout test under dry condition. The implementation is fully implicit to avoid time stepping constraint in the explicit

scheme. As shown in Figure 70, the damage concentrates along the minimum principal stress direction, and there are heterogeneities along the borehole depth (on the right plot of Figure 70): close to the boundary, the damage is more pronounced while inside the borehole, the damage is smaller and distributed nonuniformly.

Additional 2D slices of XY plane in Figure 71 illustrate the boundary effect on stress distribution along the wellbore with much higher impact on the outer boundary (front and back) than near the center (20 mm and 30mm). 2-D snapshots of 3-D microCT images of two experimental cases performed at 100 °C with brine injection fluid (SWG-100-BRI) and 150 °C with clean water (SWG-150-H2O) are also shown in Figure 72. Comparison of Figure 71 and Figure 72 shows similar patterns of wellbore damage between simulation and experimental outcomes. For example, Figure 72b&d and Figure 71 planes at 10mm and 40mm show that the damage profiles from the simulation results are qualitatively similar to experimental observations at the middle location along the wellbore. Also, the damage profile was much smaller near the central locations at 20mm and 30mm as shown in the central location of microCT images in Figure 72a&c. This model comparison clearly shows that the current damage model can be utilized to analyze experimental data properly with proper model parameter update and geometrical update.

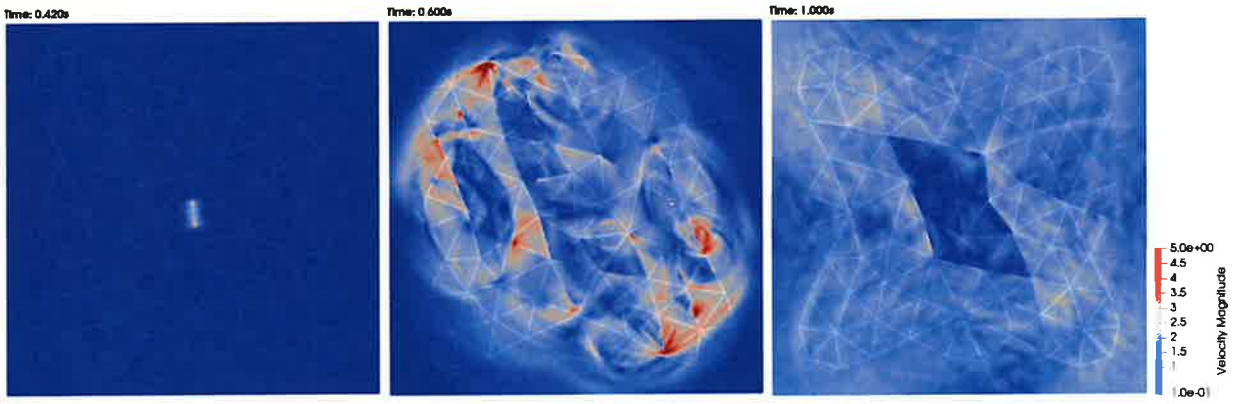

Figure 67. Particle velocity distribution of off-fault injection at three different times.

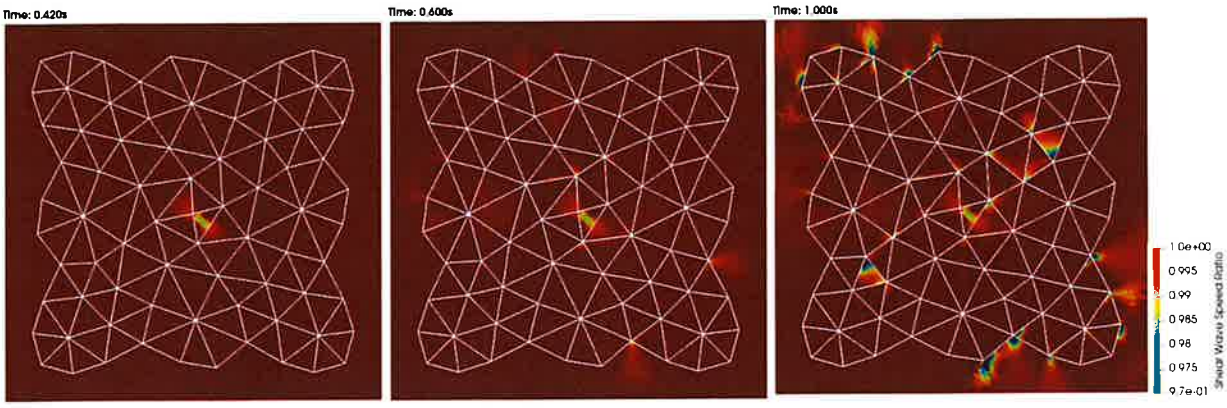

Figure 68. Shear wave speed ratio distribution of on-fault injection at three different times.

Table 6. Model domain and computational parameters for 3D borehole breakout problem.

Geometry Dimensions	**Value**	**Unit**	**Comments**
Domain Length (x)	50	mm	
Domain Length (y)	75	mm	
Domain Length (z)	50	mm	
Borehole Diameter	11.3	mm	
Mesh Size $\boldsymbol{\Delta x}$	2	mm	
Time Step $\boldsymbol{\Delta t}$	Adaptive	second	Initial dt = 1e-3 s
Rock Mechanical Properties	Value	Unit	Comments
Shear Modulus	6.125	GPa	
First Lamé Constant	4.083	GPa	
Internal Friction Angle	39.7	°	
Density	1918.77	kg/m^3	
Loading Conditions	**Value**	**Unit**	**Comments**
Stress $\boldsymbol{\sigma_{xx}}$	-50	MPa	Compression
Stress $\boldsymbol{\sigma_{yy}}$	-20	MPa	Compression
Stress $\boldsymbol{\sigma_{zz}}$	-30	MPa	Compression

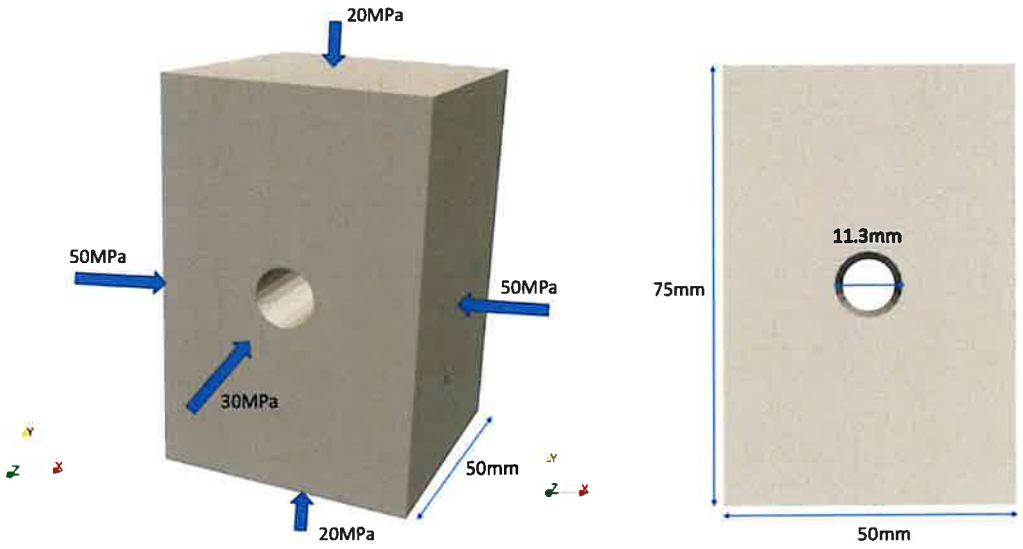

Figure 69. Problem Setup of 3D wellbore breakout problem.

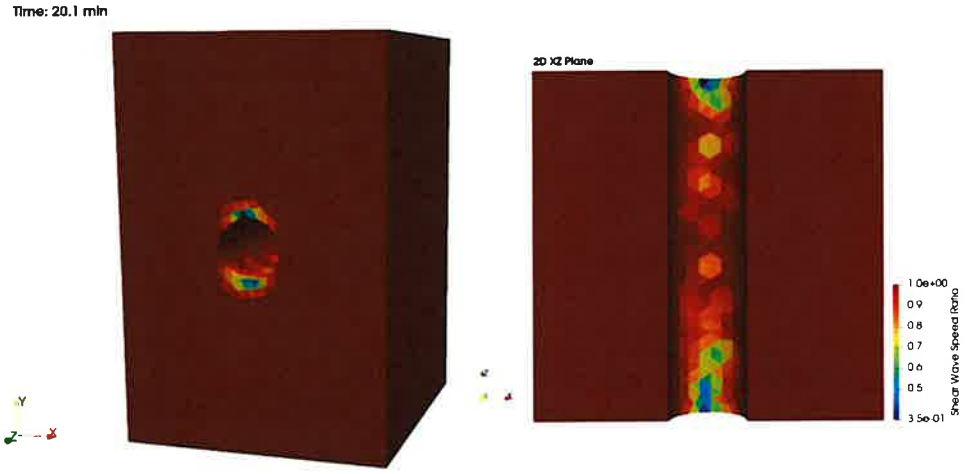

Figure 70. 3D distribution and XZ Plane of Shear Wave Speed Ratio.

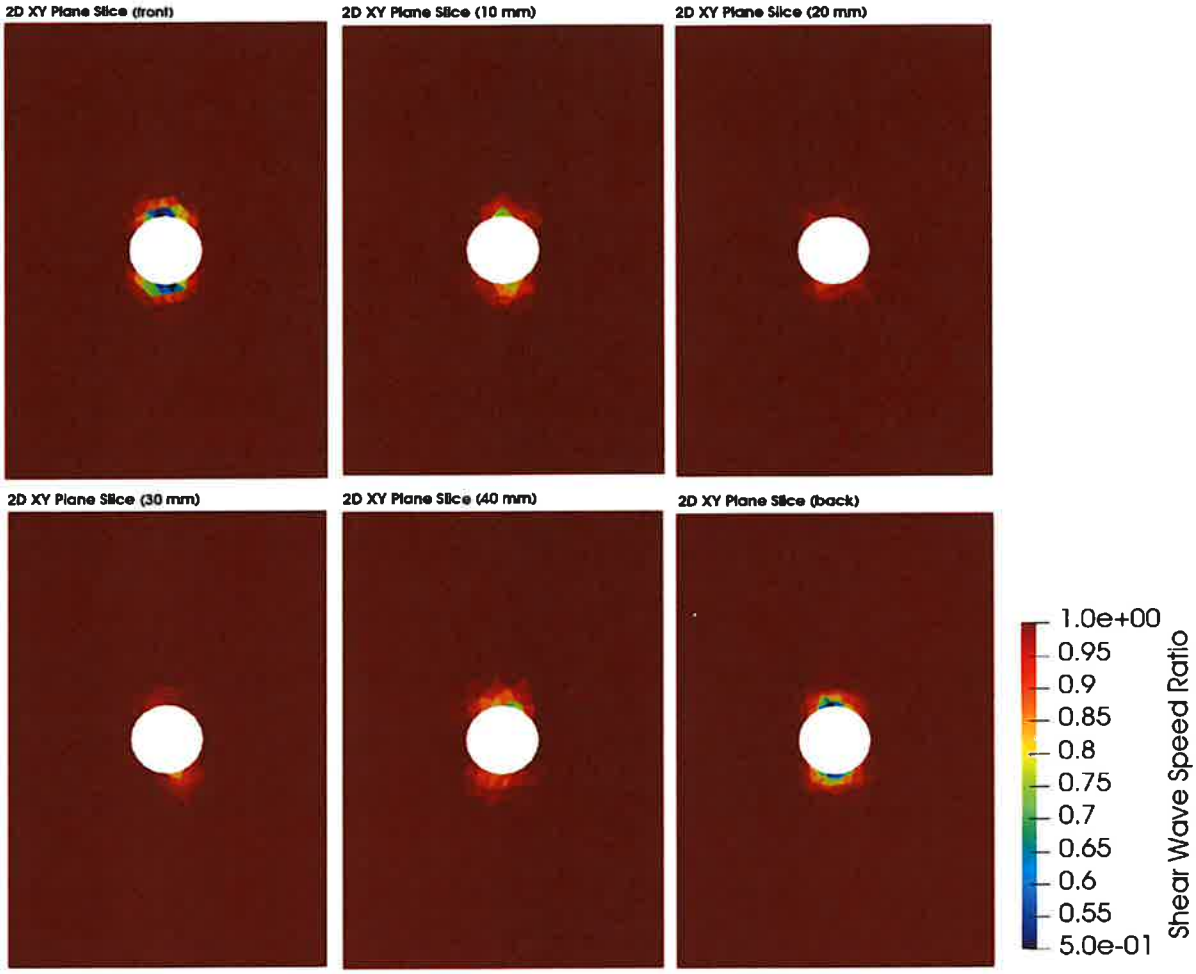

Figure 71. 2D XY plane view of shear wave speed ratio at three different locations from a location close to the center (30 mm) to the back side (50 mm).

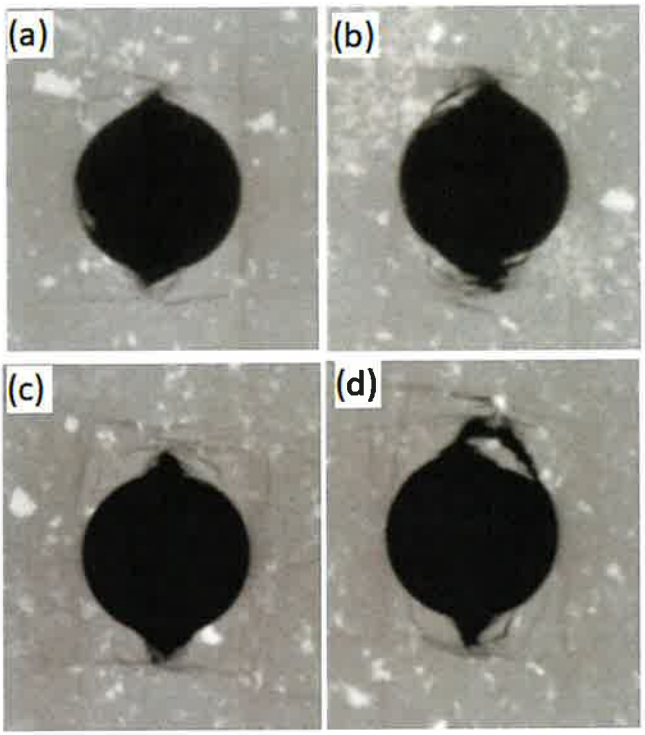

Figure 72. 2-D snapshots of 3-D microCT images from two experimental cases performed at (a-b) 100 °C with brine and (c-d) 150 °C with clean water. (a and c) show damages at a middle location along the wellbore and (b and d) a middle location between the cylindrical outer surface and the central location of the wellbore. Note that the simulation geometry is a full 3D configuration and wellbore breakout experimental samples have a cylindrical shape as in the experimental setup section. Note that microCT images are rotated to match simulation geometry in terms of the maximum stress direction.

Fracture initiation and propagation during wellbore breakout tests: Here we perform borehole breakout numerical tests using cylindrical geometry as in the experimental task on two cases: (1) dry sample with pure solid mechanics and (2) fluid saturated sample with fully hydro-mechanical coupling. First, model parameters were calibrated against available experimental data, while other model parameters for damage -Breakage related parameters were calculated based on simulations. For Sierra White granite material properties, internal friction angle was obtained based on the true-triaxial experimental results for the same Sierra White granite in Ingraham et al. (2018). Applying the Drucker–Prager yield criterion, and assuming it inscribes the Mohr–Coulomb yield surface, we obtain the following relationship with the internal friction angle ϕ:

$$B = \frac{2\sin\phi}{\sqrt{3}\,(3-\sin\phi)}$$

The angle of internal friction ranged between initial yield and failure, $\phi \approx (37.03^{\circ}, 51.82^{\circ})$. In Lyakhovsky et al. (1997), the relationship between the angle of internal friction, ϕ, and the onset of damage accumulation in the CDB model is given in the following equations. We pick the internal friction angle $\phi = 45^{o}$, correspondingly $\xi^{o} \approx -0.8073$, using the equation below Lyakhovsky et al. (1997):

$$\xi_o = -\frac{\sqrt{3}}{\sqrt{2q^2(\frac{\lambda_o}{\mu_o}+\frac{2}{3})^2+1}} \qquad q = \frac{sin(\phi)}{1-sin(\phi)/3}$$

To constrain the model parameters, a uniaxial compression test has been performed as shown in Figure 73b and the peak of stress-strain curve was capped with reported uniaxial compressive strength (UCS) = 176.2 MPa. The model is constrained on the bottom surface in all directions, and a displacement rate $\dot{u} = 1 \times 10^{-6}$m/s (or strain rate $\dot{\epsilon} = 1 \times 10^{-5}\ 1/s$) is applied on the top boundary. The domain is discretized uniformly with mesh size Δx = 2.5mm, and the loading is quasi-static with no inertia effects. We record the overall reaction force F on the top boundary and plot uniaxial stress versus axial strain. The results are shown in Figure 73 (Left). We tested dry sample and obtained one set of CDB parameters as listed in Table 7, the damage evolution rate $C_d = 80\ 1/s$ sufficiently capture the peak strength.

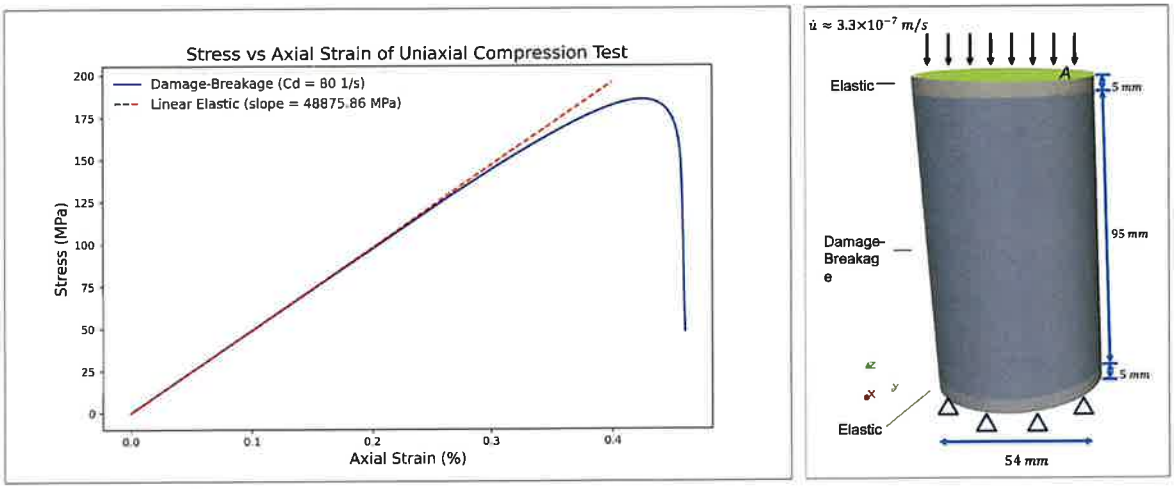

Figure 73. (Left) Results of uniaxial compression test. Red dashed and blue lines represent the linear elastic model and the damage-breakage model, respectively. The choice of Cd = 80 1/s captures the peak value of 176.2 MPa reported in the lab experiments. (Right) The problem setup of uniaxial compression test. We relate the length scale with grain size of the rock sample (l = 1.3 mm.) and the parameters include $\hat{C}_d = 10, m = 0.8, \hat{\dot{\epsilon}} = 10^{-4}\ 1/s$. All model parameters for borehole breakout test are summarized in the following Table 7.

Wellbore Breakout Test: Dry Sample: In this problem, only finite deformation balance of linear momentum is solved. The model setup for the dry sample is shown in Figure 74a, following actual experimental procedure for wellbore breakout tests. For the dry sample, Pp = 0, P = 17.2 MPa, and 18.2MPa (1MPa differential stress) on the top boundary, a static solve is performed first to obtain the equilibrated field. Then in the dynamic solve, strain rate $\dot{\epsilon} = 3.3 \times 10^{-6}\ s^{-1}$ (displacement rate $\dot{u}_2 = 3.3 \times 10^{-7}\ s^{-1}$) is applied on the top boundary, until stress plateau is reached. We use adaptive time stepping with initial time step Δt = 0.1s, growth factor = 1.5 and reduction factor = 0.5, a cap of maximum time step Δt_{max} = 10s. As shown in Figure 74b-c, the continuum damage-breakage (CDB) model accurately reproduces both stress-strain response (slope and the peak differential stress value) and observed breakout geometry shape. Note the simulation is also

performed using constant $C_d = 80\ 1/s$, which shows very close results on stress-strain response (not shown).

Wellbore Breakout Test: Fluid saturated sample: The fluid saturated sample is solved via fully coupled hydro-mechanics formulation. The model setup for the fluid saturated sample is identical to one for the dry sample, while loading and pore pressure loading are divided into two steps, following the actual experiment setup:

Step 1: with initial seating load applied on the sample, the sample is under time-varying confining pressure, and fluid pressure increased until target values are reached. This step is simulated quasi-statically to obtain the stress state before the axial strain is applied.

Step 2: After Step 1, the system is subject to Pp = 3.4 MPa and P = 21.6 MPa (see Figure 74a). The loading is the same as described in dry sample. This step is solved fully dynamically with an inertia effect, until the peak strength is reached.

Table 7. Material parameters for Borehole Breakout Test

Parameter Name	Value
Young's Modulus (λo)	48.5 GPa
Poisson's Ratio (μo)	0.22
Density ρ	2640 kg/m^3
Strain invariant ratio (onset of damage) (ξ_o)	-0.8073
Strain invariant ratio (onset of breakage) (ξ_d)	-0.8073
Ratio of two energy state (χ)	0.8
Reference damage accumulation rate ($\widehat{C_d}$)	10 1/s
Reference strain rate ($\hat{\epsilon}$)	$10^{-4}\ 1/s$
Reference damage coefficient (m)	0.8
Damage healing evolution coefficient (C1)	0 1/s
Damage healing evolution coefficient (C2)	0.05 1/s
Width of transitional region (β)	0.05
Breakage evolution coefficient (C_B)	100 C_d 1/s
Breakage healing evolution coefficient (C_{BH})	0 1/s
Compliance of the fine granular material (C_g)	10^{-12}1/s
Power law index coefficient (m_1)	10
Power law index coefficient (m_2)	1
Porosity (ϕ)	0.008
Permeability (κ)	10^{-20} I m^2
Fluid bulk modulus (K_f)	2.2 GPa
Fluid density (ρ_f)	1000 kg/m3
Viscosity (μ_f)	10^{-3} Pa · s
Length scale (l)	1.3 mm
Granular/Solid grains bulk modulus	50.38 GPa
Dilatancy evolution parameter (g_o)	0.2
Dilatancy evolution parameter (η_{cv})	0.006
Dilatancy evolution parameter (r)	2

Figure 75 summarizes the preliminary results for the stress-strain response, and borehole breakout shape. Figure 75a shows a comparison between the lab measurement of breakout shape and numerical simulation and the simulation results captures the breakout location as well as the preferred fracture directions. Figure 75b also shows that the model can capture the initial slope, point of deviation and peak value, with a fixed increased $C_d = 70\ 1/s$.

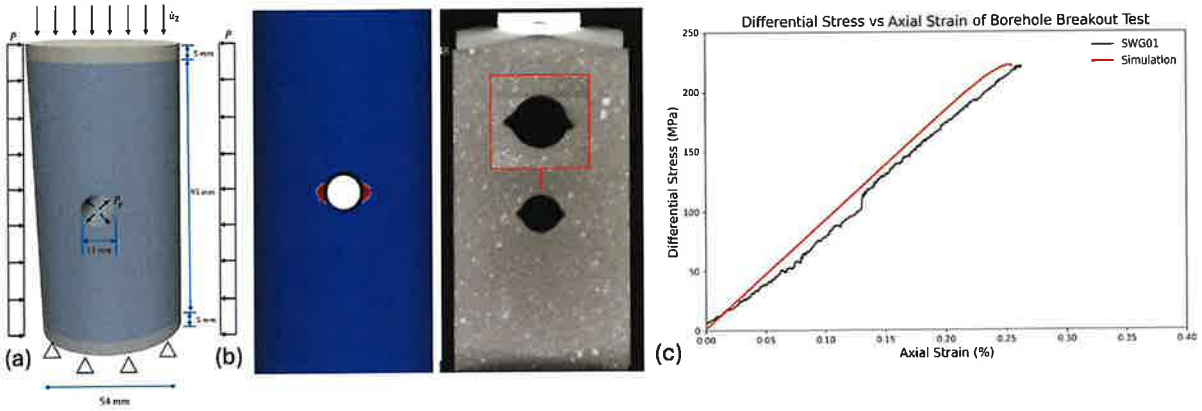

Figure 74. Geometry setup and borehole-breakout test results. (a) Model geometry and loading conditions. Note the gray cylinders placed on top and bottom sides are deformed elastically, the middle blue cylinder adopts continuum damage-breakage (CDB) rheology model. (b) Quantitative comparison of the dry-sample breakout shape, showing excellent agreement near the borehole. (c) Differential-stress evolution for the dry sample versus experimental data, accurately reproducing both the slope and peak strength.

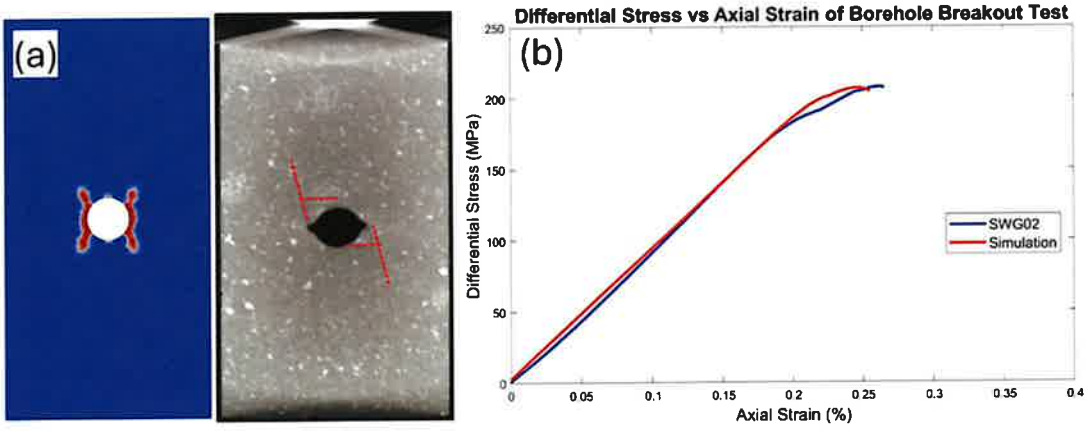

Figure 75. Results for wet sample breakout test. (a) Quantitative comparison of the fully saturated wet-sample breakout shape, capturing the observed crack-propagation direction as shown in microCT image. The heterogeneity of the experimental sample may have triggered a preferential direction of growth for the crack bands on each side of the borehole. (b) Differential-stress evolution for the wet sample compared with experiments, showing good agreement in the slope (elastic properties) and peak strength, and the point of slope deviation, compared to experimental data (SWG-AMB-H2O).

4.1.4 Joint Inversion with ML-driven Geothermal Field Generation and Simulation Models

The estimated permeability field from the proposed method is presented in Figure 76. It is shown that there are reasonable connections between injection and production wells. Figure 76b shows the pressure response of the injection well over time, and a parity plot of pressure data with the fitting error as the root mean square error (RMSE) is shown in Figure 76c. The results indicate that the simulation of the estimated field is consistent with the measurements. The main difference between the measured pressure and the simulated pressure occurs around 310 minutes after shut-in and this might be because the wellhead pressure changes rapidly while the current model cannot capture the abrupt pressure drawdown at the current coarse scale model resolution. The permeability inversion took about 2 hours to complete on a workstation equipped with 32 Intel 2.1 GHz CPU cores and two NVIDIA RTX A6000 GPUs.

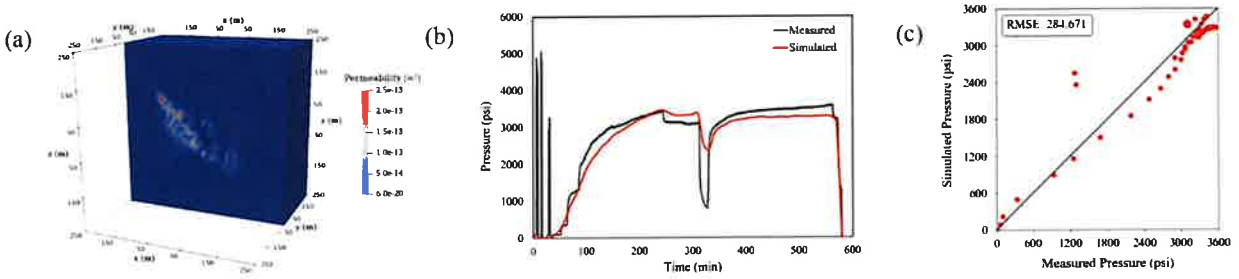

Figure 76. (a) Estimated permeability field; (b) Pressure response over time; (c) The fitting error between the measured pressure and the simulated pressure.

For the validation of the current permeability estimation, we used the estimated fractured permeability field to run a geothermal flow and heat transport simulation with the August-September 2024 circulation test configuration. Figure 77 shows the estimated permeability field and the simulation results. Figure 77b and Figure 77c show the pressure and temperature distributions at the end of simulation, i.e., 26 days of the circulation test.

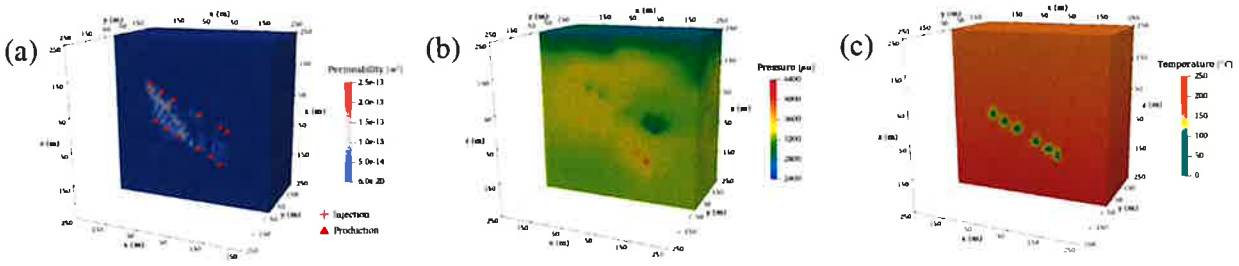

Figure 77. (a) Estimated permeability field; (b) Pressure distribution at the last timestep; (c) Temperature distribution at the last timestep.

In Figure 78, we plot the measured and simulated pressure responses over time and present the measured and simulated production temperature over time. The simulated injection pressure is

consistent with the measured pressure, and the simulated production temperature shows a similar trend to the measured temperature.

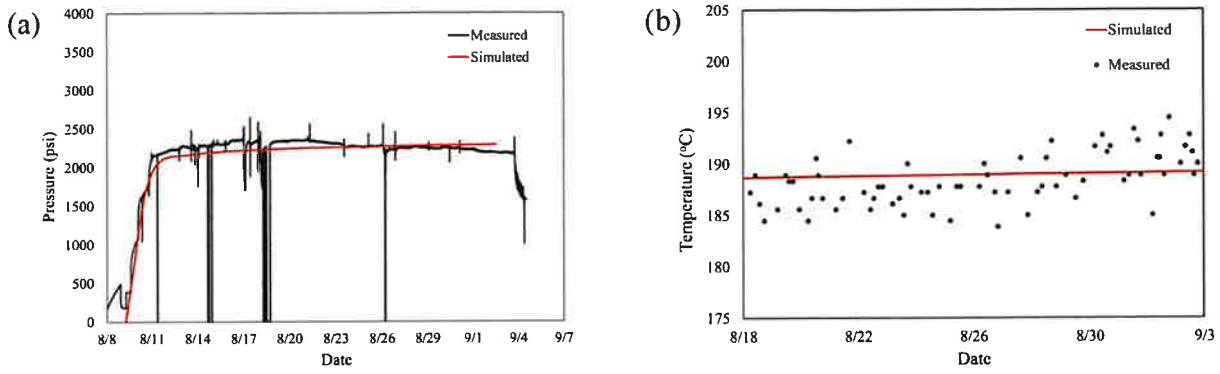

Figure 78. Measured and Simulated (a) pressure and (b) temperature response as a function of time.

4.2 Implications of Findings for Utah FORGE and EGS Technologies

Geophysical Monitoring of Fractures Undergoing Shear: Monitoring the frictional behavior of hot granite fractures under shear is essential for understanding and evaluating the mechanical stability of fractures under EGS conditions. The laboratory experimental research shows that seismic monitoring is an effective tool to monitor the shear behavior of discontinuities, to provide an assessment of the local behavior of the frictional surface under the transducer, and to predict failure of the discontinuity. This approach is applicable to both dry and saturated discontinuities and can be employed across a wide range of pore pressures and temperatures.

Previous studies have shown that the shear behavior of rock fractures depends on temperature, but that the shear behavior of granite fractures (e.g., shear strength and shear fracture stiffness) is not considerably affected by temperatures below 100°C (Kim & Jeon, 2019; Tang, 2020). For granite, the strength degradation may begin beyond 100-200°C (Chen et al., 2012; Zhao et al., 2019; Tang & Zhang, 2020), but a noticeable reduction has been reported to occur beyond 400°C (Chen et al., 2012; Sun et al., 2015). This study was performed on granite fractures at 50 °C and 100°C under water pressures, indicating that the temperature did not significantly affect the mechanical behavior of the fractures tested. These results suggest that seismic monitoring of granite discontinuities under EGS conditions can be effectively implemented and interpreted once high-temperature ultrasonic transducers are developed and deployed in the field. Such monitoring can help predict or minimize induced seismicity associated with hydraulic stimulation. Potential extensions of this research include applications to fault-zone monitoring and, with further investigation, the potential contribution to earthquake prediction studies.

Electrical Resistivity Measurements: Electrical techniques are increasingly being used to evaluate changes in fractures during geothermal operations. The interpretation of fracture properties from electrical measurements relies heavily on theoretical models that link the electrical response of a